PhD thesis

Annette Johansen, MD

Molecular neuroimaging of synaptic plasticity in the human brain

Name of department: Neurobiology Research Unit, Department of Neurology,
                          Copenhagen University Hospital, Rigshospitalet, Copenhagen,
                          Denmark

Author(s):   Annette Johansen, MD

Title: Molecular neuroimaging of synaptic plasticity in the human brain

Institutions: Neurobiology Research Unit, Copenhagen University Hospital
                          Rigshospitalet & Faculty of Health and Medical Sciences,
                          University of Copenhagen, Copenhagen, Denmark

Principal Supervisor: Professor Gitte Moos Knudsen,
                          Neurobiology Research Unit,
                          Copenhagen University Hospital Rigshospitalet

Co-supervisors: Dr. Patrick MacDonald Fisher,
                          Neurobiology Research Unit,
                          Copenhagen University Hospital Rigshospitalet

                          Dr. Pontus Plavén-Sigray,
                          Neurobiology Research Unit,
                          Copenhagen University Hospital Rigshospitalet

Submitted on: October 3, 2023

Date of defense: December 8, 2023

Assessment committee: Professor Steen G. Hasselbalch
                          Department of Clinical Medicine, University of Copenhagen,
                          Copenhagen, Denmark

                          Dr. Johan Lundberg
                          Department of Clinical Neuroscience, Karolinska Institutet,
                          Stockholm, Sweden

                          Professor Richard E. Carson
                          Yale PET Center, Yale University, New Haven, USA

Contents

List of manuscripts

The thesis is based on the following manuscripts.

I. **Johansen, A**.*, Beliveau, V.*, Colliander, E., Raval, N.R., Dam, V.H., Gillings, N., Aznar, S., Svarer, C., Plavén-Sigray, P., & Knudsen, G. M. An *in vivo* high-resolution human brain atlas of synaptic density. Submitted to *Journal of Neuroscience* September 2023.

II. **Johansen, A**., Armand, S., Plavén-Sigray, P., Nasser, A., Ozenne, B., Petersen, I. N., Keller, S. H., Madsen, J., Møller, K., Vassilieva, A., Langley, C., Svarer, C., Stenbæk, D. S., Sahakian, B. J. & Knudsen, G. M. Effects of escitalopram on synaptic density in the human brain: A randomized controlled trial. *Molecular Psychiatry. 2023 (E-pub ahead of print).*

III. **Johansen, A**., Plavén-Sigray, P., Madsen, M.K., Søndergaard, A., Messel, C., Grzywacz, M., Nasser, A., McCulloch, D.E., Beliveau, V., Vassilieva, A., Lund, A., Lehel, S., Stenbæk, D. S., Fisher, P., Svarer, C., & Knudsen, G. M. Effects of psilocybin on synaptic density in the human brain. *Manuscript in prep.*

Related articles not included in thesis:

1. Laurell, G.L., Plavén-Sigray, P., **Johansen, A**., Raval, N.R., Nasser, A., Madsen, C.A., Madsen, J., Hansen, H.D., Donovan, L.L., Knudsen, G.M., Lammertsma, A.A., Ogden, R.T., Svarer, C. & Schain, M. Kinetic models for estimating occupancy from single-scan PET displacement studies. *J Cereb Blood Flow Metab* 43, 1544-1556 (2023).

2. Langley, C., Armand, S., Luo, Q., Savulich, G., Segerberg, T., Søndergaard, A., Pedersen, E.B., Svart, N., Overgaard-Hansen, O., **Johansen, A**., Borgsted, C., Cardinal, R. ., Robbins, T.W., Stenbæk, D. S., Knudsen, G.M. & Sahakian, B.J. Chronic escitalopram in healthy volunteers has specific effects on reinforcement sensitivity: a double-blind, placebo-controlled semi-randomised study. *Neuropsychopharmacol* 48, 664-670 (2023).

3. Raval, N.R., **Johansen, A**., Donovan, L.L., Ros, N.F., Ozenne, B., Hansen, H.D. & Knudsen, G.M. A Single Dose of Psilocybin Increases Synaptic Density and Decreases 5-HT2A Receptor Density in the Pig Brain. *Int J Mol Sci* 22, 835 (2021).

Acknowledgements

Keller for fighting to keep the HRRT and the Allogg alive at the same time. To Søren Holm for taking the time to talk physics to a silly medical student.

Lastly, I owe thanks to the important people outside the walls of Rigshospitalet: Thank you Anja Chylomicron Jørgensen, for being there for the fun and the hard times, through medical school and grown-up life. The endless hours of studying (and hanging out) have served me well through this PhD-journey. To Skvætbanden; Ditte, Mari, Rikke & T. Hansen, thank you for nearly 20 years of friendship and support, and for motivating me to leave the office and come out to play. Thank you for being my safety net, for cheering me on and for the surprise celebration.

Thank you Morfar, for sharing your curiosity about the workings of the world with me ever since a was a kid. I know I was not all that impressed when you introduced me to Pythagoras, but you planted a seed that never stopped growing. Thank you Onkel, for all of your support through the years, and for taking weights off my shoulders so I could go play science. Thank you uncle Henrik and aunt Harriet, for all that you have done for me, and for introducing me to my home away from home in the States. Colleen and Emmett, thank you for being an anchor and a safe haven in this crazy world.

To my dearest Mormor, for her unconditional love and support. And to my parents, for giving me the world.

Summary

The dynamic adaptability of the human brain, termed neuroplasticity, is a central topic in neuroscience. In the developmental phase, the serotonin system crucially influences the processes through which the brain rearranges its pathways, synaptic connections, and functions. Disorders like depression have been proposed to constitute a state of diminished or malfunctioning neuroplasticity. Pharmacological treatments often target the serotonin system, and are hypothesized to work by inducing neuroplasticity. As the processes of neuroplasticity are mainly detectable on microscopic and cellular levels, research focused on the human brain constitutes a major challenge to the research community.

The work forming the basis for this thesis leveraged positron emission tomography (PET) neuroimaging of the Synaptic Vesicle glycoprotein 2A (SV2A) to explore synaptic plasticity in the human brain, focusing on pharmacological modulation of the serotonin system. We first implemented SV2A PET neuroimaging with the radiotracer [^{11}C]UCB-J and created a population-based human brain atlas. In two subsequent clinical trials, we investigated the effects of the selective serotonin-reuptake inhibitor (SSRI) escitalopram and the psychedelic compound psilocybin on cerebral SV2A density.

In Study I, *in vivo* PET SV2A imaging was combined with *in vitro* autoradiography to create a quantitative *in vivo* human brain atlas of synaptic density. The atlas reveals prominent SV2A density gradients reflecting functional topography and cortical hierarchies among functional domains.

In Study II, we applied a double-blind, randomized, placebo-controlled trial design to investigate cerebral SV2A binding in healthy volunteers who received either escitalopram or a placebo for 3-5 weeks. Whereas there was no statistically significant group-difference, we demonstrate time-dependent effects of escitalopram on SV2A density. These results suggest that the delayed treatment response often seen in SSRI-treated patients with major depression could be associated with drug-induced neuroplastic changes taking several weeks to evolve.

In Study III, we applied a single-arm, open-label trial design to investigate the effects of a single psychoactive dose of psilocybin in healthy individuals. We did not find statistically significant increased SV2A binding one week after the intervention. However, exploratory analyses suggest that SV2A binding changes may be related to positive emotional experiences during the intervention session.

In conclusion, this thesis presents a population-based *in vivo* atlas of the human brain's synaptic density that will be freely available to the neuroscience community. Our intervention trials constitute the first *in vivo* investigations linking serotonergic drugs to neuroplasticity in the human brain.

Dansk resumé

Hjernens tilpasningsevne, kaldet neuroplasticitet, er et centralt tema i neurovidenskab. Signalstoffet serotonin spiller en afgørende rolle for neuroplasticitet under hjernens udvikling, idet det modulerer de processer, som hjernen bruger til at reorganisere sin struktur, synaptiske forbindelser og funktioner. Effekten af klassiske og nyere serotonerge farmakologiske behandlinger af neuropsykiatriske tilstande som depression kan muligvis være forbundet med øget neuroplasticitet. Da de neuroplastiske processer hovedsageligt foregår på mikroskopisk og cellulært niveau, har det indtil nu være vanskeligt at undersøge neuroplasticitet i den levende menneskehjerne.

Studierne som danner grundlag for denne afhandling gør brug af hjerneskanningsmetoden positron-emissions tomografi (PET). Anvendt sammen med sporstoffet [^{11}C]UCB-J kan PET-skanningerne fremstille billeder af forekomsten af et protein som findes i hjernens synapser, nemlig Synaptisk Vesikel glykoprotein 2A (SV2A).

I denne afhandling etableres først et populations-baseret atlas af menneskehjernens forekomst af SV2A. Dernæst undersøges det om der sker ændringer i hjernens SV2A som udtryk for synaptisk plasticitet når raske forsøgspersoner indtager lægemidler med effekt på serotoninsystemet. Lægemidlerne er escitalopram, som er en selektiv serotonin-genoptagelseshæmmer (SSRI) samt det psykedeliske stof psilocybin, som stimulerer serotonin 2A receptoren.

I det første studie kombinerede vi PET og autoradiografi for at skabe et atlas over synapsetætheden i hjernen. Atlasset viser forskelle i tætheden af synapser som afspejler de funktioner, som hjernen varetager, så som bevægelse, sanseindtryk, og tænkning.

I det andet studie gennemførte vi et dobbeltblindet lodtrækningsforsøg med escitalopram og placebo. Sammenlignet med placebo finder vi gennemsnitligt ikke nogen statistisk forskel i hjernens SV2A niveau hos forsøgspersoner som i 3-5 uger fik escitalopram. Dog så vi, at jo længere tid deltagerne indtog escitalopram, desto højere var deres SV2A niveauer. Dette kan muligvis være med til at forklare, hvorfor behandlingseffekten af SSRI'er ofte først sætter ind efter flere ugers behandling.

I det tredje studie undersøgte vi i raske forsøgspersoner hvordan en psykedelisk dosis af psilocybin påvirker hjernens SV2A niveau. Selvom vi ikke så nogen gennemsnitlig stigning i SV2A, så vi mulige tegn på at øget SV2A i hjernen kan være relateret til følelsesmæssige positive oplevelser under psilocybin sessionen.

Sammenfattende giver afhandlingen gennem etableringen af et detaljeret hjerneatlas af SV2A et vigtigt bidrag til fremtidig forskning i synaptisk densitet. Dette atlas vil være frit tilgængeligt for andre forskere. Endvidere bidrager afhandlingen med indsigt i hvordan farmakologisk påvirkning af serotoninsystemet påvirker hjernens synaptiske plasticitet.

Abbreviations

1TCM	One-tissue compartment model
2TCM	Two-tissue compartment model
5-HT	5-hydroxytryptamine, serotonin
5-HT$_{2A}$R	Serotonin 2A receptor
5-HTT	Serotonin transporter
ASC	Altered States of Consciousness
B_{avail}	Density of receptors available for binding *in vivo*
B_{max}	Density of receptors *in vitro*
BBB	Blood-brain barrier
BP_{ND}	Non-displaceable binding potential (*in vivo*)
EDI	Ego-Dissolution Inventory
f_P	Free fraction of radioligand in plasma
GM	Grey matter
GPCR	G-protein coupled receptor
HPLC	High-pressure liquid chromatography
HRRT	High-Resolution Research Tomograph
IQ	Intelligence quotient
i.v.	Intravenous
K_D	Dissociation constant
keV	Kiloelectron volt
L	Ligand
LOR	Line of response
MBq	Mega becquerel
MDD	Major depression disorder
MEQ	Mystical Experiences Questionnaire
MRI	Magnetic Resonance Imaging
OP-OSEM	Ordinary Poisson ordered subset expectation maximization
PET	Positron emission tomography
ROI	Region of interest
SRTM	Simplified reference tissue model
SSRI	Selective serotonin reuptake inhibitor
TAC	Time-activity curve
TB	Total binding
V_{ND}	Non-displaceable volume of distribution
V_s	Specific volume of distribution
V_T	Total volume of distribution
WM	White matter

Background

1. Neurons

The human brain is estimated to consist of a staggering 86 billion neurons, matched by a roughly equivalent number of glial cells (Pakkenberg and Gundersen, 1997; Azevedo et al., 2009). While neurons are the principal effector cells of the nervous system, glial cells play pivotal supporting roles for normal brain function.

Neurons, although varied in subtypes, all share distinct morphological features (Figure 1). Central to this structure is the cell body, known as the soma. Radiating from the soma are multiple branching processes, termed dendrites, resembling branches on a tree. In addition to dendrites, each neuron extends a single, elongated process called the axon. The axon can span a minimal distance, merely reaching a neighboring neuron, or it can extend considerably, traveling as far as the base of the spinal cord. The axon terminates in multiple processes called the axon terminal. These simple features make neurons uniquely qualified for signal conduction, modulation and integration, which is ultimately achieved through specialized junctions between the neurons, known as synapses, as detailed in the following section.
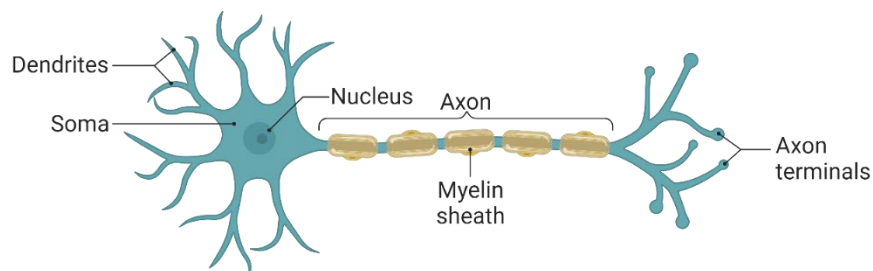
Figure 1. Schematic representation of a typical neuron.

1.1   Synapses

All brain function relies on rapid signaling between neurons which occurs at specialized structures, i.e., synapses (Figure 2). Most synapses in the CNS are chemical synapses which means that the signal is transmitted from the presynaptic neuron by release of a chemical substance (neurotransmitter) into the narrow space (the synaptic cleft) separating it from the postsynaptic neuron. Neurotransmitters are stored in vesicles in the axon terminal of the presynaptic neuron and release occurs when an electrical signal travels from the cell soma along the axon to the axon terminal and depolarizes the cell membrane. This event triggers release of calcium ions that interact with vesicular proteins to promote

fusion of the synaptic vesicles with the cell membrane. The neurotransmitters then diffuse through the extracellular matrix to the postsynaptic neuron and bind to receiver proteins (receptors), whereby the signal is received. The specific effects elicited by receptor stimulation depend on the specific receptor subtype, as exemplified in section 2. Brain function is thus dependent on and determined by which neurons form synapses and what signals they convey.
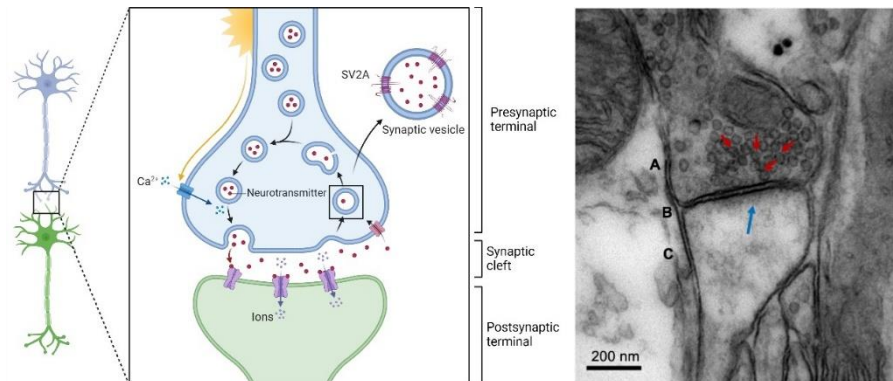
Figure 2. Left panel: schematic illustration of a chemical synapse and its vesicles. Right panel: Electron microscopy (EM) visualizing the structure of a synapse at 80,000x magnification. (**A**) Presynaptic neuron. Synaptic vesicles indicated with red arrows. (**B**) Synaptic cleft. (**C**) Dendritic spine of a postsynaptic neuron indicated with a blue arrow. EM photo published by (Serrano et al., 2022), curtesy of Nuria García-Font (García-Font et al., 2019).

1.2   Neuroplasticity

The human brain develops over 20-25 years (Silbereis et al., 2016). From the early embryological stages of neurogenesis to the continued synaptic pruning in early adulthood, the objective is to establish the most efficient connections between brain regions (macroscale) and neuron populations (microscale). This development has been fine-tuned through evolution to ensure that the central nervous system is able to respond appropriately to internal and external stimuli and ultimately navigate and interact with its environment. Although genes are the major orchestrating factor, the finetuning is to a great extent experience-dependent, meaning that the stimuli that the brain receives (e.g., from sensory organs or hormonal fluctuations) affect how the brain's networks are shaped. The processes that can be activated or suppressed include neuronal migration, synaptogenesis, cell growth or programmed cell death. Collectively, these processes can be categorized under the term neuroplasticity. Functionally, neuroplasticity can be thought of as the ability of the brain to change and adapt to physiological or psychological stimuli to uphold homeostasis in the most efficient way possible (Duman and Aghajanian, 2012). Importantly, this includes elimination of inactive connections to limit energy expenditure.

The pivotal role of neuroplasticity is quite evident in early brain development. In adulthood, the changes in brain organization are less dramatic, however, plasticity remains

essential for functions like memory consolidation and the acquisition of new skills and habits. The capacity for neuroplasticity becomes especially relevant in pathological conditions that impede normal brain function. This is easily exemplified in the rehabilitation of patients suffering from hemiplegia following a stroke where the brain can rewire itself around the damaged areas to allow return of motor control. The same mechanisms may be less obvious in the treatment of psychiatric disorders characterized by maladaptive thought patterns and behaviors, such as depression, anxiety, or substance abuse disorders. As neurons are largely unable to replicate after birth, adaptation and rewiring in the adult human brain rely predominantly on forming new synaptic connection between neurons, i.e. synaptic plasticity.

A large body of preclinical studies have established a link between the brain's serotonin system and neuroplasticity (Gaspar et al., 2003; Branchi, 2011; Kraus et al., 2017). The work forming the basis of this thesis centers on two key proteins in this system and will be introduced in the following sections.

2. The serotonin system

The serotonin system is a monoamine neurotransmitter system highly conserved across species (Azmitia, 2020). Serotonin is involved in regulation of important behavioral and physiological functions related to e.g., appetite, sleep, stress response, and cognitive function (Gaspar et al., 2003; Salvan et al., 2023). It is produced from the amino acid tryptophan in neurons in the raphe nuclei of the brainstem, from where these neurons project extensively to the cerebrum and, to a notably lesser extent, to the cerebellum. When released into the synaptic cleft, serotonin molecules move by way of diffusion and interact with serotonin receptors on the dendrites of the postsynaptic neuron.

Fourteen different serotonin receptors (5-HTR) have been identified in humans, each with its own characteristic spatial distribution (Beliveau et al., 2017). All but one belong to the group of G-protein coupled receptors (GPCRs), while the exception, the 5-HT$_3$R, is a ligand-gated cation channel. GPCRs are located in the cell membrane and are characterized by their seven transmembrane domains. When an endogenous ligand or an agonist drug bind to the active site, the receptor is stabilized in its active conformation. This prompts activation of a guanine nucleotide-binding protein (i.e., the G-protein) located on the intracellular side of the cell membrane, thereby initiating a second messenger signaling cascades. The exact nature of this cascade and its subsequent effects are determined by the specific G-protein to which the receptor is coupled. The downstream effects encompass a wide range, from immediate actions that activate ion channels and result in membrane depolarization to processes involving cytoskeletal rearrangements and gene transcription that unfold over a longer time period.

Two important proteins belonging to the serotonin system are the serotonin transporter (5-HTT) and the serotonin 2A receptor (5-HT$_{2A}$R). These two proteins are the primary targets of the pharmacological interventions explored in this thesis and will be characterized in more detail in the following sections.

2.1   The serotonin transporter

The 5-HTT is a presynaptic protein located within the cell membrane of serotonergic neurons (Figure 3). In the cerebrum, this transporter is predominantly expressed in the striatum and thalamus, with a more modest presence in the cerebral cortex. Its primary role is to reuptake serotonin into the axon terminal, thereby contributing to the regulation of the serotonin level within the synapse. Upon reentry into the presynaptic neuron, serotonin can be repackaged into synaptic vesicles for future use or be broken down by the enzyme monoamine oxidase A (MAO-A).

Pharmacological agents that bind to and inhibit the 5-HTT can decrease the rate of serotonin reuptake. Among these are the selective serotonin reuptake inhibitors (SSRIs), typically used as an antidepressant, and which, as the name suggests, show selectivity for the 5-HTT. SSRIs are frequently prescribed for various brain disorders, most importantly depression, anxiety, and obsessive-compulsive disorder (OCD), for which they are considered a first-line pharmacological treatment disorders (Gabriel et al., 2020). The prevalent hypothesis for SSRIs' mode of action is that by inhibiting 5-HTT, SSRIs increase serotonin in the synaptic cleft, thereby strengthening serotonergic neurotransmission. However, despite extensive clinical use and research over the past 30-40 years, the precise mechanisms through which this leads to alleviation of symptoms have yet to be fully understood. Equally important is the question of why upwards of 30% of patients with, e.g., depression, do not experience improvement in their symptoms (Rush et al., 2006).

Among the SSRIs, the drug escitalopram exhibits the highest 5-HTT selectivity (Owens et al., 2001). Escitalopram is the S-enantiomer of the racemic compound citalopram, which preceded the development of escitalopram. While both enantiomers bind to the active site of the 5-HTT, S-citalopram not only exhibits a higher affinity but also acts as a positive allosteric modulator that increases the affinity to the active site (Zhong et al., 2012).

Selective Serotonin Reuptake Inhibitor (SSRI) Mechanism of Action
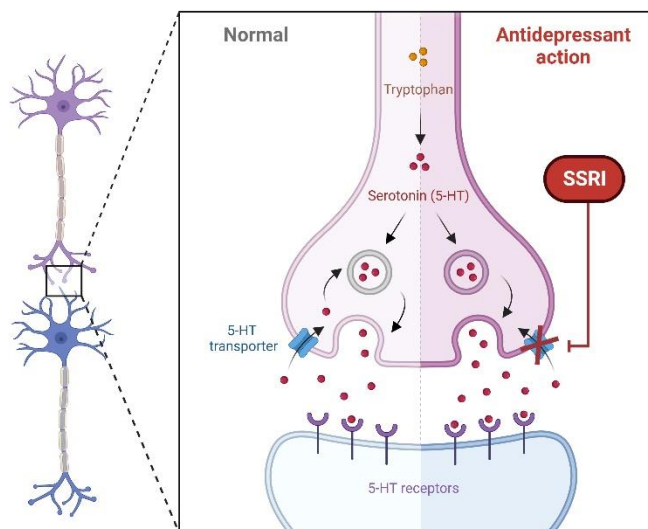
Figure 3. Schematic representation of SSRI inhibition of the 5-HTT. Adapted from (Chu and Wadhwa, 2023).

2.2   The serotonin 2A receptor

The 5-HT$_{2A}$R is one of three GPCR subtypes of the serotonin 2 receptor family. The 5-HT$_{2A}$R is highly expressed in the neocortex compared to other serotonin receptors, and is particularly abundant in the frontal, temporal, and cingulate cortices as well as precuneus area (Ettrup et al., 2014; Beliveau et al., 2017). In contrast, the hippocampus, striatum and thalamus show considerably lower expression. The 5-HT$_{2A}$R is generally considered to be a postsynaptic receptor found predominantly on apical dendrites. However, some studies have identified 5-HT$_{2A}$Rs intracellularly and even in axons and in glial cells (Cornea-Hébert et al., 1999; Miner et al., 2003).

The 5-HT$_{2A}$R primarily activates the G$_q$ signaling pathways leading to activation of the intracellular protein kinase C and Ca^{2+} release which in turn activate downstream second messengers. The G$_q$ pathways is a common pathway for GPCRs, yet the 5-HT$_{2A}$R is quite distinct because of its psychoactive effects. Many 5-HT$_{2A}$R agonists induce acute and profound changes in perception and states of consciousness. At lower doses, these effects may be limited to visual distortions and subtle changes in mood, while moderate to high doses can invoke intense emotional states such as altered sense of time, space, and self, changed meaning of concepts, experience of profound insights; and in some cases, intense feelings of unity with the universe, and ego-dissolution, i.e., an experience of absence of a self (Vollenweider et al., 1998; Kometer et al., 2012; Quednow et al., 2012; Nichols, 2016; Madsen et al., 2019; Stenbæk et al., 2021; McCulloch et al., 2022). Collectively, compounds activating the 5-HT$_{2A}$R and producing such effects are termed psychedelics and they encompass a variety of chemical structures.

The effects of psychedelics are not only inherently intriguing in their phenomenology but have also gained renewed interest due to rapidly growing evidence of their ability to effectively treat mood and anxiety disorders (Carhart-Harris et al., 2016, 2018, 2021; Erritzoe et al., 2018; Roseman et al., 2018; Davis et al., 2021) which are otherwise commonly treated with SSRIs.

2.3   Serotonergic interventions and synaptic plasticity

The motivation for exploring the relationship between human neuroplasticity and pharmacological agents such as psychedelics and SSRIs stems in part from the observation that their therapeutic impacts often outlast their pharmacological presence in the body and brain. This enduring effect is particularly noticeable in the case of psychedelics, which have been demonstrated to produce long-lasting effects on depressive symptoms following only one or two administrations. Such observations strongly suggest that these psychedelics elicit fundamental changes in brain structure or function. Given the many neurobiological correlates identified for physiological and psychological functions through neuroimaging techniques and lesion analyses, it seems plausible to hypothesize that the effects of psychedelics must leave some identifiable marks on the brain, and that these could be related to neuroplasticity.

In contrast, the situation with SSRIs is less straightforward. To achieve their therapeutic effects, SSRIs typically necessitate daily administration over extended periods, ranging from several months to years. However, medication is often tapered after achieving remission of symptoms, indicating that lasting neurobiological changes must have occurred to sustain the treatment gains. Yet, without deeper understanding of the underlying mechanisms, it remains unclear what role SSRIs play in the therapeutic responses. To draw an analogy, in the context of treating a fractured arm or leg, the cast or crutches provided to the patient do not directly prompt cellular repair. Instead, they facilitate the healing process by alleviating mechanical strain and keeping the bones in place. Similarly, understanding the role of serotonergic interventions in psychiatric disorders could reveal whether these drugs serve primarily as facilitators of inherent neurobiological repair mechanisms or have a more direct, causal role in treatment outcomes.

The neuroplastic effects of psychedelics (Banks et al., 2021; Vos et al., 2021; Olson, 2022; Calder and Hasler, 2023; Zhornitsky et al., 2023) and SSRIs (Branchi, 2011; Kraus et al., 2017; Umemori et al., 2018) have been extensively reviewed. Collectively, the literature supports the ability of these pharmacological agents to induce neuroplasticity *in vitro* Typically, assessment of a compound will include investigation of its ability to upregulate transcription of genes associated with development of the nervous system or involved in cellular reorganization, e.g., the brain-derived neurotrophic factor (BDNF). Other plasticity measures include a compound's capacity for inducing cell proliferation and differentiation, increase in dendritic spine density and complexity, or expression of synaptic proteins. However, the body of research that these reviews are based on, is almost exclusively

conducted in in animals or cell cultures, as molecular and cellular *in vivo* biomarkers of neuroplasticity are lacking (Wall et al., 2023).

3. Positron emission tomography

Positron emission tomography (PET) is an imaging technique that allows researchers to visualize and characterize molecular systems in the living brain. To achieve this, a specific molecule is labeled with a positron-emitting isotope. This molecule is referred to as the radiotracer, or simply, tracer, and its emitted signal can be detected by a PET camera. Because these radioactive isotopes have practically identical chemical properties to their non-radioactive counterparts, they can replace a stable atom without changing the molecule's properties. By incorporating the isotope into suitable molecules that interact with biological systems in a known and predictable manner, it is possible to obtain spatial information on, e.g., molecular structures, biochemical processes, and physiological functions. While the theory behind PET can seem fairly straightforward, many technical steps need careful consideration and execution, as outlined in the following sections.

3.1 Basic principles of PET

For PET imaging in humans, the tracer is administered before or at the start of the PET scan. The most common route of administration is intravenous (i.v.) bolus injection, but depending on the research target and question, other routes such as per oral or intrathecal administration can be used.

Following an i.v. injection, the radiotracer is distributed to the entire body via the blood stream. Eventually, the radiotracer molecules decays, causing one of the protons in the atom to convert into a neutron. In the reaction, a positron, which is the anti-particle to an electron, is emitted from the nucleus. Despite the term *positron-emission* tomography, it is not the positron itself that is detected by the PET camera. Instead, the energy released in the decay reaction causes the emitted positron to travel a short distance until it collides with an electron in a sufficiently low energy state. This event results in the annihilation of the particles and emission of two gamma photons at an angle of ~180°. Due to their high-energy state, the gamma rays can penetrate tissue and make their way to the detectors of the PET camera.

The PET camera consists of a ring of detectors sensitive to the energy level of the emitted gamma rays (511 keV). As the gamma rays travel in opposite directions at the speed of light, they will be detected virtually simultaneously (a coincidence), and it must follow that the annihilation event occurred somewhere along an imagined line (the line of response, LOR) connecting the two detector elements (Figure 4). To obtain spatial information, a

sufficiently high number of coincidences must be detected; a higher number of observed coincidences correlates with improved spatial accuracy of the tracer distribution. However, this also necessitates a larger radioactive dose, posing a potential constraint in human studies. Modern PET systems incorporate a time-of-flight technique to increase the resolution. This enables the PET system to measure the almost infinitely small delay between the two photons' arrival in the detector, narrowing down the localization of the annihilation along the LOR.

When acquiring dynamic scans, the data is divided into time-frames of increasing length. The data then undergo reconstruction to convert the raw counts into the 3D distribution, and ultimately a 4D dataset. The reconstruction further makes corrections that take into account that a fraction of emitted photons will arrive at the detector within the time window of another unrelated photon (random count), thus resulting in a 'false' LOR. Another source of error that is corrected is photon scatter, where a photon is deflected from its original path, again leading to a false LOR. Lastly, attenuation correction is applied to account for the loss in signal intensity caused by photons absorbed by the different tissue types, notably bone structures.
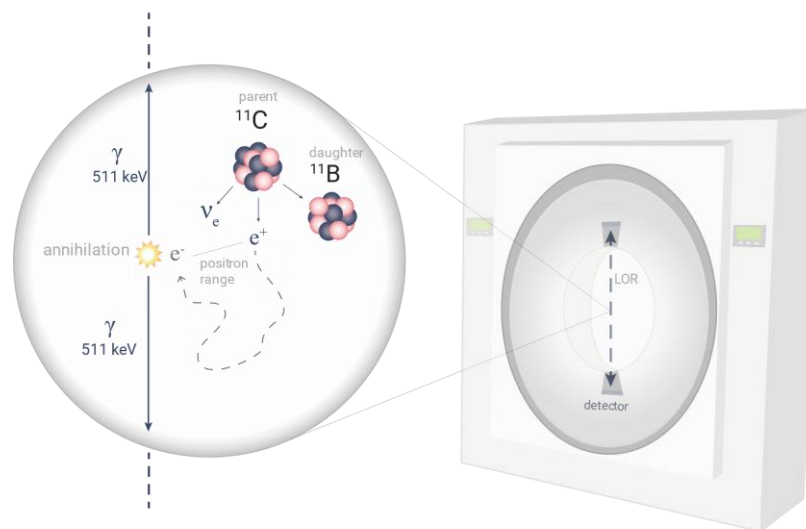
Figure 4. Schematic illustration of the basic concepts of PET. Adapted from (Raval, 2022)

3.2 PET data preprocessing

In some cases, the PET image is the final outcome of the imaging session, for instance when used for detecting tumors, which is one of the most common clinical applications of PET. However, in neuroscience PET is mainly used for quantification of

specific proteins in the brain. For this purpose, a few steps of preprocessing need to be applied to the PET data.

Motion-correction: Given the duration of PET scans, typically ranging from 60-120 minutes, slight head movements by even the most compliant or catatonic participants are almost inevitable. To mitigate this, post-reconstruction motion correction can be applied by aligning each frame either to a representative reference frame or in a frame-by-frame manner. While these methods can correct motion *between* frames, they cannot correct motion *within* a frame. Alternatively, an external motion-tracking device can be used for event-by-event motion correction during reconstruction. This approach, while theoretically more precise, depends on the secure positioning of the tracking device.

Anatomical identification: This step involves identifying relevant anatomical structures of interest. Currently, PET images do not have sufficiently high spatial resolution for anatomical delineation of brain regions, which instead relies on co-registering the PET data to a T1-weighted magnetic resonance image (MRI), from which regions of interest (ROIs) can be defined automatically by applying a template brain atlas. This step typically includes tissue segmentation to determine the boundaries between grey matter, white matter, and cerebrospinal fluid. After this step, the PET data is extracted as time-activity curves (TAC) representing the decay-corrected radioactivity count per volume tissue (kBq/mL) for individual ROIs.

The settings for each step of the acquisition and preprocessing pipeline can affect the outcome of a study, and should thus be tailored to individual tracers and experimental setups (Nørgaard et al., 2019a, 2019b). Regardless of the pipeline setup, rigorous quality control of each step is required for each PET scan.

3.3   PET kinetic modelling

After reconstruction of the PET scan, the data must be converted into a standardized metric to make fair comparisons between groups or across different conditions. An obvious method would be to compute a weighted average over the scan's duration. However, this approach is vulnerable to multiple confounding variables. For instance, given the elusive nature of radioactivity, working with short-lived isotope like Carbon-11, which has a half-life of 20.4 min, makes it practically impossible to administer the same dose of radioactivity for every scan. Furthermore, even with the assumption of consistent dosing, differences between subjects would make such comparison unreliable for two main reasons: 1) the higher the body-weight of a subject, the larger a volume the tracer will be 'diluted' in, thus lowering the concentration in both blood and brain tissue; 2) as with any other substance administered, the body will immediately start to eliminate the tracer. This typically involves metabolizing the tracer to facilitate excretion. The rate of these processes varies and can be sensitive to pathological conditions or drug treatment.

Compartment models provide a conceptual framework for interpreting tracer behavior and, when accompanied by mathematical models, can provide outcome parameters that reflect the concentration of the target protein in tissue (Gunn et al., 2001).

The work presented in this thesis is based on one of the simpler compartment models; the one-tissue compartment model (1TCM; Figure 5a).
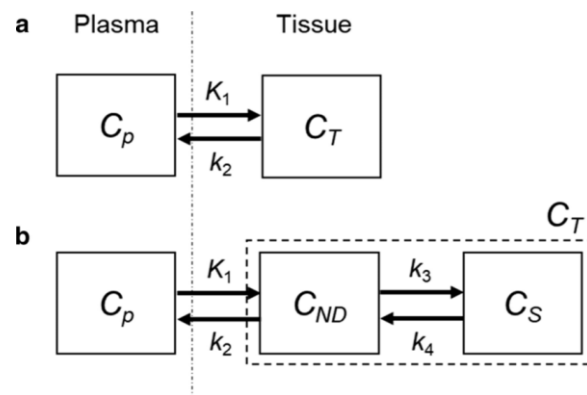
Figure 5. Schematic representation of the 1-Tissue compartment model (**a**) and the 2-Tissue compartment model (**b**). Adapted from (Hiroyama et al., 2020).

Within the 1TCM framework, the tracer is delivered from the arterial plasma (the blood compartment) into the brain (the tissue compartment) by passive diffusion (Figure 6). Because the diffusion of the individual tracer molecules is random, tracer molecules will at some point diffuse from the brain back into the blood-stream. Transfer of tracer between compartments is described by the rate constants K_1 (mL/cm^3/min) and k_2 (min^{-1}).
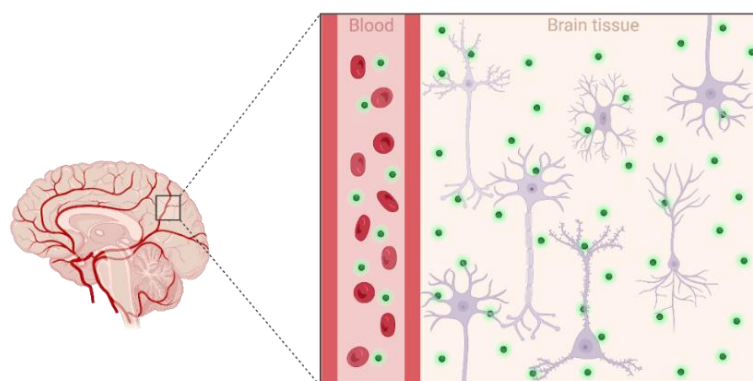
Figure 6. Schematic illustration of tracer molecules diffusing from the blood into the brain tissue and binding to cellular structures.

If the target protein is present in the tissue, the tracer will bind to it and be temporarily trapped in the tissue compartment, i.e., it will accumulate in the tissue. The ratio between

concentration in tissue (C_T) and plasma (C_P) could thus serve as an outcome parameter for PET quantification. However, it takes time before the tracer gets from the blood into the tissue and binds to the target protein and thus the ratio of the concentrations will change over time. Therefore, for the ratio to provide a meaningful outcome, it must be measured under equilibrium conditions where the net tracer movement between comparts is zero. The concentration ratio at equilibrium is termed the total distribution volume (V_T; Eq. 1)

$$V_T = \frac{C_T}{C_P} \; (1)$$

Because the tracer is cleared from the plasma after the initial distribution phase, true equilibrium cannot be achieved from bolus injection experiments (Carson, 2000). Administering the tracer as a bolus followed by a constant infusion provides a way to achieve equilibrium, however this method is sensitive to variation in plasma clearance between individuals, which would bias the estimates. To work around the difficulties of equilibrium, it is possible to instrumentalize some mathematical features of the compartment model to make it compatible with bolus injection experiments. This is achieved from the differential equation describing the 1TCM:

$$\frac{dC_T(t)}{dt} = K_1 \times C_P(t) - k_2 \times C_T(t) \; (2)$$

First, V_T can be expressed as the ratio of the rate constants, which can be shown by setting the derivative to zero and rearranging the equation;

$$V_T = \frac{C_T}{C_P} = \frac{K_1}{k_2} \; (3)$$

In contrast to the C_T and C_P measures, the rate constants are assumed to be time-invariant given that the system is in physiological steady-state for the duration of the scan acquisition (Morris et al., 2004). For PET experiments, this means that there are no major changes in physiological parameters such as blood flow or temperature. As such, if it is possible to estimate the rate constants from bolus injection PET experiments, V_T can be derived from their ratio without achieving equilibrium.

The key to estimating the rate constants lie in the solution to the system's differential equation (Eq. 2). The solution describes total tracer concentration in tissue as a function of time:

$$C_T(t) = C_P(t) \otimes K_1 \times e^{-k_2 t} \; (4)$$

The concentration of tracer in plasma, $C_P(t)$ is obtained by measuring the tracer concentration in arterial plasma during the PET experiment, and is referred to as the arterial

input function (AIF). Eq. 4 is thus the model that is fitted to the PET data to estimate the rate constants, and in turn estimate V_T.

It is important to keep in mind that the 1TCM is a simplification of a complex biological system. For instance, in addition to binding to the target protein, the tracer will also bind to other cellular components in a non-specific manner. Thus, the total tissue concentration is the sum of tracer that is specifically bound (C_S), non-specifically bound (C_NS), and free in the tissue (C_FT). This distinction can be made explicit in the model by introducing a separate compartment for the specific binding, which turns the model into a two-tissue compartment model (2TCM; Figure 5b). Here, the free and non-specifically bound tracer is collapsed into the same compartment and denoted the non-displaceable compartment (C_ND). Similar to the 1TCM, equations describing the 2TCM can be rearranged and its differential equations solved to provide equations for fitting the PET data.

Theoretically, the volume of distribution for the specific compartment (V_S) or the ratio between specific and non-displaceable binding ($V_\mathrm{S}/V_\mathrm{ND}$) can be calculated from the rate constants. However, the individual parameters can rarely be estimated reliably, so V_T is often the outcome parameter from the 2TCM.

Another approach to differentiate the specific binding from the non-displaceable binding is by using a reference tissue. A true reference tissue is a region that has the same tissue properties as the region of interest, except that it is devoid of the target protein. If such a region exists, kinetic modelling can be applied, and the reference tissue's total volume of distribution will be equal to the V_ND in the region of interest.

A reference region can also allow for non-invasive quantification, i.e., without obtaining arterial blood samples. It is, however, crucial that the non-displaceable binding does not differ between subject group or change following intervention, as this can bias the results of the study (Johansen et al., 2018; Laurell et al., 2021).

3.4   The arterial input function

The brain PET data is often the main focus in PET imaging, but the AIF also deserves attention as it is equally complex and influential for the outcome. Below, the steps for calculation the AIF will briefly be mentioned.

Shortly after tracer bolus administration, the radioactivity concentration in blood and plasma will reach a peak that can be measured using an automatic, continuous blood sampling system or by rapid manual sampling. The tracer rapidly mixes in the whole blood pool and distributes in the entire body. At this point, the changes in concentration are less dramatic and discrete blood samples can be drawn at longer intervals to cover the entire scan duration.

To calculate the AIF, one or more laboratory analyses must be performed. The radioactivity is counted in a gamma counter to get whole blood and plasma count rate. Because the body treats a radiotracer like a drug, most tracers will be metabolized by the liver and sometimes in plasma or other tissues. Therefore, the plasma is analyzed to measure

the fraction of the radioactivity originating from the intact tracer molecules (referred to as parent compound), and how much is from radiolabeled metabolites. The resulting parent fraction curve can often be fitted using, e.g., a Hill function or other function describing a one- or two-phase decay over time. This function is then multiplied with the plasma time-activity curve to obtain the metabolite-corrected arterial input function to be used in the PET kinetic modelling.

4. Synaptic imaging *in vivo*

4.1   Synaptic vesicle glycoprotein 2A

The Synaptic Vesicle glycoprotein 2A (SV2A) is membrane-bound protein located in the axon terminal's synaptic vesicles. Comprising 742 amino acids, the structure of SV2A consists of 12 transmembrane domains and also includes a loop that extends into the vesicle lumen. Specific sites have been identified for the attachment of phosphate groups or long chains of carbohydrate molecules (on the luminal side) (Stout et al., 2019).

The function of SV2A in neurotransmission has not been fully established. Its structural resemblance to specific transporter protein families, notably those involved in glucose and neurotransmitter transport, has led to speculations on a possible transporter role (Mendoza-Torreblanca et al., 2013). Additionally, the carbohydrate chains attached to SV2A have been proposed to adsorb neurotransmitters, thus lowering the concentration gradient and allowing more neurotransmitter to be loaded into the vesicle. Motifs on SV2A that bind to other synaptic proteins, e.g., synaptophysin, and Ca^{2+} indicate dynamic regulation of its function, potentially depending on the stage in the vesicle's life cycle or other cellular demands.

SV2A is expressed in all brain structures without a predilection for a specific neurotransmitter system (Bajjalieh et al., 1994), in agreement with SV2A gene transcription in a large range of glutamatergic excitatory and GABAergic inhibitory neuron subtypes (Pazarlar et al., 2022). Compared to one of the most commonly used presynaptic markers, synaptophysin, SV2A staining using immunohistochemistry techniques show spatial correlation on a cellular level (Nowack et al., 2010) and preserved regional ranking (Finnema et al., 2016). In the rat brain, one study estimated that synaptic vesicles contained 1.7 SV2 molecule per vesicle (Takamori et al., 2006), while another estimated that 97% of synaptic vesicles contain 5 SV2 molecules (not distinguishing between SV2A and the less abundant isoforms; SV2B and SV2C) (Mutch et al., 2011).

4.2   SV2A imaging with [^{11}C]UCB-J

For many years, *in vivo* PET imaging of synaptic structures has been limited to imaging of neurotransmitter receptors or transporters, while synaptic quantification across transmitter systems was restricted to post-mortem tissue analysis or surgical specimens. This barrier was removed in 2016 when the first study reporting successful SV2A quantification in humans was published by Finnema et al. (Finnema et al., 2016). Based on extensive compound screening (Mercier et al., 2014), several candidates with high SV2A affinity and high likelihood of permeating the blood-brain barrier (BBB) were identified. Following preclinical *in vivo* experiments (Nabulsi et al., 2016), the compound [^{11}C]UCB-J was found to have the best imaging properties, and was found to have an exceptionally high brain uptake, signal-to-background ratio, and very favorable kinetics in both humans and non-human primates.

Subsequent research has utilized [^{11}C]UCB-J to uncover SV2A alterations in various neurological (Chen et al., 2018; Finnema et al., 2020; Matuskey et al., 2020; Mak et al., 2021; Michiels et al., 2021; Delva et al., 2023) and psychiatric disorders (Holmes et al., 2019; Onwordi et al., 2020; D'Souza et al., 2021; Radhakrishnan et al., 2021; Angarita et al., 2022).

In parallel, methodological studies have delved into optimizing PET data analysis, including reconstruction, quantification, partial-volume correction, and understanding the impacts of brain activation, among other aspects (Finnema et al., 2017; Koole et al., 2019; Rossano et al., 2019; Mansur et al., 2020; Mertens et al., 2020; O'Dell et al., 2020; Smart et al., 2020; Tuncel et al., 2020; Lu et al., 2021; Naganawa et al., 2021). Model comparison as part of initial validation favored the 2TCM over the 1TCM in 73%-92% of fits, However, given the occasional unreliability of 2TCM fits and the general agreement between the two models (Finnema et al., 2017; Mansur et al., 2020), the 1TCM has been widely accepted as the optimal choice for full kinetic modelling with [^{11}C]UCB-J.

Reference tissue methods for SV2A quantification have been extensively investigated. As no grey matter region in the brain is entirely devoid of SV2A, no true reference region exists. Many studies have employed cerebral white matter, specifically the centrum semiovale, as a pseudo-reference. Several approaches are used to obtain different outcome parameters: calculating distribution volume ratios (DVR) or DVR-1 estimates from 1TCM V_T estimates, using reference tissue modeling with e.g., the Simplified Reference Tissue Model (SRTM) to obtain pseudo-BP_{ND} estimates, or by calculating ratios of the TACs from later scan periods. The white matter, being a more lipophilic tissue with some specific [^{11}C]UCB-J signal, remains a debated choice for a reference. Concerns arise from factors like age-related white matter changes and the impact of diseases or various interventions, which could bias results. Thus, its use requires meticulous evaluation in each research context.

Aims & hypotheses

The overall aim of the thesis was to employ SV2A PET neuroimaging to investigate synaptic plasticity in the human brain in relation to pharmacological modulation of the serotonin system. To this end, we first implemented and characterized the PET radiotracer [^{11}C]UCB-J in humans. Second, we conducted two intervention studies in healthy volunteers to evaluate the effects of 5-HTT inhibition and 5-HT$_{2A}$R stimulation, respectively, on cerebral SV2A density. The specific aims and hypotheses for the three studies making up this thesis are outlined below.

4.3   Study I

The aim of the study was to create a high-resolution in vivo human brain atlas of synaptic density using SV2A as a proxy. We hypothesized that regional estimates obtained [^{11}C]UCB-J PET imaging would strongly correlate with regional estimates obtained with [^{3}H]UCB-J autoradiography, enabling us to convert the PET-based estimates into a brain atlas of absolute SV2A protein density.

4.4   Study II

The aim of the study was to investigate the effect of 5-HTT inhibition with the SSRI escitalopram on *in vivo* synaptic density in the human brain, using SV2A as a proxy. We hypothesized that following 3-5 weeks of intervention, hippocampal and neocortical SV2A binding would be higher in the group receiving an SSRIS compared to the group receiving a placebo.

We further tested the secondary hypotheses that longer duration intervention and higher serum escitalopram concentration would be associated with higher SV2A binding in the escitalopram group.

4.5   Study III

The aim of the study was to investigate the effect of 5-HT$_{2A}$R stimulation with the psychedelic compound psilocybin on synaptic density in the human brain, using SV2A as a proxy. We hypothesized that one week after a single psilocybin intervention session, frontal and hippocampal SV2A binding would be increased compared to baseline measurements.

In a n exploratory analysis, we further tested the hypotheses 1) that participants with higher subjective intensity ratings would have larger increase in SV2A binding, and 2) that participants with higher SV2A increase would rate higher on positive persisting effects three month after the psilocybin intervention

Methods

5. Ethics, approvals, and registrations

Data collection was conducted in accordance with Declaration of Helsinki, and all participants and donors provided written informed consent. All study protocols were approved by the relevant authorities. For study I and II, this included approval of by the Ethics Committee of the Capitol Region of Denmark (identifier: H-20062005, H18038352, respectively). Study III was approved by the Ethics committee (identifier: H-16028698) and the Danish Medicines Agency (EudraCT identifier: 2016-004000-61). Studies II and III were also registered at ClinicalTrials.gov (identifier: NCT04239339; NCT03289949, respectively).

A smaller number of subjects contributing to study I were included under a different protocol also approved by the ethics committee (identifier: H-KF-2006-20). All study protocols were registered with the Danish Data Protection Agency. Personal information related to study participants was kept confidential and accessible only to staff members working on the projects, in keeping with Danish laws ("Autorisationsloven," "Sundhedsloven," and the law on doctor-patient confidentiality) and the General Data Protection Regulation (GDPR).

6. Study design

6.1 Study I

This study combined data obtained with different techniques; *in vivo* [^{11}C]UCB-J PET and structural MRI imaging, *in vitro* [^{3}H]/[^{11}C]UCB-J autoradiography, and mRNA microarray profiling. PET and MRI data included all healthy participant data collected as part of ongoing [^{11}C]UCB-J studies, including study 2 and 3 included in this thesis. We included participants under the age of 50 years who had undergone a [^{11}C]UCB-J PET scan at the HRRT scanner at Rigshospitalet without any pharmacological intervention prior to the scan, and who had a complete metabolite-corrected arterial input function. Data sets from a total of 33 individuals were included, along with demographical variables. Data were processed in FreeSurfer to obtain regional, vertex and voxel based [^{11}C]UCB-J estimates as described in section 9.3.

Brain SV2A density estimates were obtained from [³H]UCB-J autoradiography (section 9.6) performed on post-mortem brain tissue from the Bispebjerg Hospital Brain Bank (Bispebjerg-Frederiksberg Hospital, Copenhagen University Hospital, Denmark). This dataset included tissue sections from the frontal, parietal, temporal, and occipital cortices, along with the white matter, obtained from seven donors with no history of brain disorders. SV2A estimates from additional brain regions were obtained from the literature (Varnäs et al., 2020) based on [¹¹C]UCB-J autoradiography.

Regional SV2A mRNA data was obtained from the *abagen* toolbox (section 9.7) (v 0.1.3, https://abagen.readthedocs.io) (Markello et al., 2021).

6.2   Study II

The study was conducted as part of a larger double-blind, pseudo-randomized, placebo-controlled study (Langley et al., 2023). The study design is visualized in Figure 7. Thirty-two healthy participants were randomized to undergo intervention with daily oral administration of either 20 mg escitalopram or a placebo. Randomization was balanced in terms of age, sex, and IQ. Participants were started on one capsule daily (10 mg escitalopram or placebo) for three days, and then continued with two capsules daily (20 mg escitalopram or placebo) for a minimum of three weeks and a maximum of five weeks. Following the intervention period, participants came in for follow-up assessments of 1) neuropsychological testing; 2) structural and functional MRI scan; 3) [¹¹C]UCB-J PET scan. To confirm compliance with the intervention, fasting blood samples were collected for measuring steady-state drug concentration on day 10 and on the day of neuropsychological testing. All participants and investigators were blinded to intervention group allocation until completion of the data analyses.
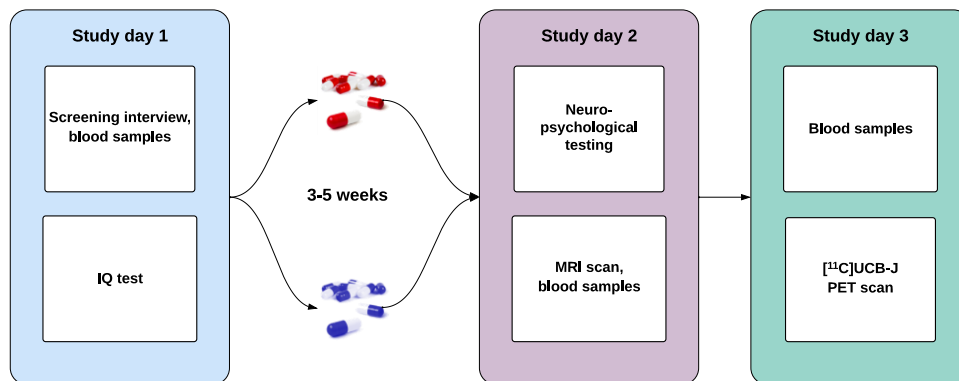
Figure 7. Study design for Study II.

6.3   Study III

The study design is visualized in Figure 8. The study was conducted as a one-arm, open-label study. Fifteen healthy individuals underwent [^{11}C]UCB-J at baseline along with an MRI scan and neuropsychological testing. The first five subjects underwent psilocybin intervention in MR settings, as they were also part of an ongoing study. The remaining 10 subjects underwent psilocybin intervention in a designated intervention room. The target dose was 0.3 mg/kg, administered in capsules of 3 mg psilocybin per capsule. Questionnaires were filled out before drug administration and at the end of the day when the psychedelic effects had subsided. Blood samples were collected throughout the day to measure plasma psilocin levels. One week after the psilocybin intervention, participants underwent a follow-up [^{11}C]UCB-J PET and MRI scan.

Study day 1	Study day 2	Study day 3	Study day 4
Screening interview Blood samples	MRI scan	Psilocybin 0.3 mg/kg	MRI scan
Neuropsychological testing	[^{11}C]UCB-J PET scan	Blood samples Questionnaires	[^{11}C]UCB-J PET scan
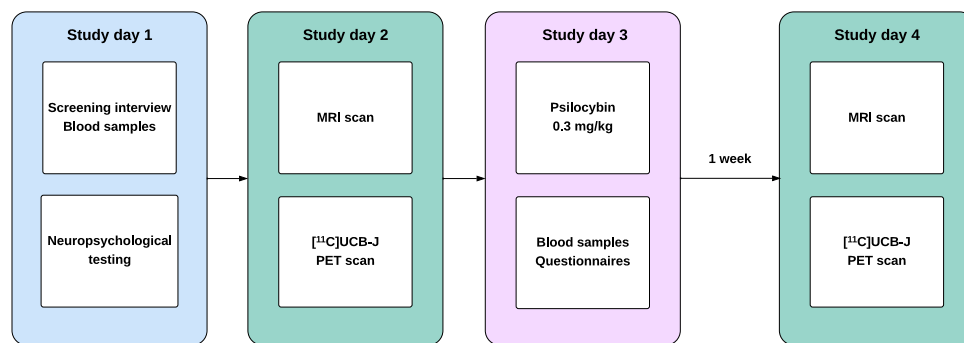
Figure 8. Study design Study III.

7. Recruitment and screening procedures

Healthy volunteers were recruited through a database in which individuals can sign up as potential participants in brain imaging studies. Individuals received both verbal and written information outlining the study, including potential side effects, before signing the informed consent form.

All participants underwent a screening procedure to ensure that they were healthy and eligible to participate in the study program. The screening procedure was performed by a medical doctor or a trained medical student and included 1) medical history, especially related to neurological or psychiatric events; 2) psychiatric screening interview to confirm absence of current or prior psychiatric condition; 3) physical and neurological examination; 4) blood samples to confirm the absence of underlying subclinical medical condition (e.g., diabetes, thyroid condition, anemia); and 5) ECG for participants taking part in the drug-intervention studies to confirm cardiac health and normal cQT interval. All participants were evaluated with respect to the exclusion criteria for the specific study (see Table 1).

Table 1: Exclusion criteria for the individual study protocols

Condition	Study II (SSRI)	Study III (Psilocybin)	Other
< 18 years of age	X	X	X
Significant somatic condition/disease	X	X	X
Present or previous neurological condition/disease	X	X	X
History of psychiatric disorder		X	
Immediate family history of psychiatric disorder		X	
Intake of QT-prolonging medication		X	
Abnormal electrocardiogram (ECG)	X	X	
Postural orthostatic tachycardia syndrome	X		
Hypotension (blood pressure < 100/70 mmHg) or hypertension (blood pressure > 140/90 mmHg)	X		
Current intake of psychoactive medication	X		
Nicotine addiction (i.e., daily nicotine consumption)	X		
Alcohol or drug abuse	X	X	X
Intake of drugs suspected to influence test results	X	X	X
Recreational drug use other than tobacco and alcohol within the last 30 days.	X		X
Life time cannabis use > 50 times	X		X
Life time recreational drug use > 10 times (for each substance)	X		X
Head injury or concussion resulting in loss of consciousness for more than 2 min	X		X
Vision or hearing impairment	X	X	X
Non-fluent in Danish	X	X	X
Learning disability	X	X	X
Pregnancy or breastfeeding	X	X	X
MRI contraindications	X	X	X
Allergy to study drugs, incl. PET-tracer	X	X	X
Significant exposure to radiation within the past year (e.g., medical imaging investigations)	X	X	X
Bodyweight less than 50 kg		X	
History of significant adverse response to a hallucinogenic drug		X	
Use of hallucinogenic drugs less than 6 months prior to inclusion		X	
Blood donation less than 3 months before study participation		X	
Low plasma ferritin levels (< 12 μg/L)		X	

8. Pharmacological interventions

8.1   Serum-escitalopram measurements

In study II, a venous blood sample was collected from participants on study day 10 and on the day of neuropsychological testing before intake of their daily dose. After centrifugation, serum was extracted and stored at -80 °C until completion of the study. The serum samples were analyzed for concentration of escitalopram using ultra-performance liquid chromatography-tandem mass spectrometer (UPLC-MS/MS) by the Laboratory of Filadelfia Epilepsy Hospital, Dianalund, Denmark.

8.2   Psilocybin intervention sessions

All psilocybin intervention sessions took place at the Danish Centre for Psychedelic Research (DCPR) under the Neurobiological Research Unit, Copenhagen University Hospital, Rigshospitalet.

On a day prior to the intervention, participants had a preparatory session with two trained therapists to establish rapport and prepare them for potential psychological effects of psilocybin. On the day of the intervention, participants were asked to arrive well-rested at 08.30 a.m., to not consume any alcohol the day before. Participants were then asked to fill out state questionnaires, after which a catheter was placed in the antecubital vein for collection of blood samples. A urine sample was collected to screen for presence of the following drugs: amphetamines, opioids, benzodiazepines, barbiturates, tetrahydrocannabinol, cocaine, ketamine, phencyclidine, and gamma hydroxybutyrate. Information concerning potential psilocybin effects and safety precautions was repeated to participants before drug administration.

The intervention sessions took place in one of two settings: Participants 1-5 underwent the intervention while in an MRI scanner and participant 6-15 in a designated intervention room (Figure 9). The therapists provided interpersonal support for the participants throughout the intervention session and for the sessions in the intervention room, a carefully curated music program was tailored to facilitate the different phases (Stenbæk et al., 2021; Messell et al., 2022). During the session, participants were asked at 20 min intervals to rate the Subjective Drug Intensity (SDI; 0-10). At the end of the intervention day, after drug effects had subsided (~4-6 hours after administration), participants filled out questionnaires relating to their experience and drug effects. After a debrief, the therapists in consultation with a medical doctor made sure that participants were ready to leave the site.

The day after the psilocybin intervention, the participants met with the therapists for an integration session and, if deemed necessary, scheduled a follow-up session. The basis for the psychological support during psychedelic drug interventions is described in more detail by (Armand, 2022).

Figure 9. The intervention room for psychedelic intervention sessions at the Neurobiology Research Unit at Copenhagen University Hospital, Rigshospitalet.

8.3   Psychedelic effects questionnaires

Questionnaires used for evaluating the psychedelic experience included the Revised Mystical Experience Questionnaire-30 (MEQ30) (Barrett et al., 2015), the Ego-Dissolution Inventory (EDI) (Nour et al., 2016), and the Altered State of Consciousness (ASC) (Studerus et al., 2010). Persisting effects were evaluated three months after the psilocybin session using the Persisting Effects Questionnaire (PEQ) (Griffiths et al., 2006).

9. Imaging acquisition and processing

9.1   MRI acquisition

All participants were scanned on a 3T Siemens Magnetom Prisma scanner (Siemens AG, Erlangen, Germany) installed at the North Wing of Copenhagen University Hospital, Rigshospitalet, in 2020. Using a 32-channel head coil, T1 and T2 weighted structural scans were acquired for the purpose of delineation of anatomical ROIs and grey matter segmentation. Protocol parameters are listed in Table 2.

Table 2: MRI acquisition protocols

	Study II (SSRI)	Study III (Psilocybin)
T1		
Resolution (mm³)	0.9 x 0.9 x 0.9	0.8 x 0.8 x 0.8
Repetition time (ms)	2000	1810
Echo time (ms)	2.58	2.42
Inversion time (ms)	972	920
Flip angle (°)	8	9
T2		
Resolution (mm³)	0.9 x 0.9 x 0.9	0.9 x 0.9 x 0.9
Repetition time (ms)	3200	3200 ms
Echo time (ms)	408	408

9.2 PET acquisition

All participants were scanned on the High-Resolution Research Tomograph (HRRT) PET scanner (CTI/Siemens, Knoxville, TN, USA) at the PET & Cyclotron Unit at Copenhagen University Hospital, Rigshospitalet. Parameters related to the [^{11}C]UCB-J PET acquisitions and reconstruction are listed in Table 3. All scans were started at the time of the intravenous [^{11}C]UCB-J bolus injection. The radioactive dose was targeted at ~5-6 MBq/kg body mass. Radioactivity in the blood was measured continuously (2 seconds intervals; flow = 8 mL/min) for the first 15 min using an automated blood sampling system (Allogg ABSS, Allogg Technology, Sweden). Manual blood samples were collected at 2.5, 5, 10, 25, 40, 60, 90, and 120 min. These blood samples were analyzed for whole blood and plasma radioactivity using a gamma counter (Cobra II auto-gamma, Packard Instrument Company, USA). Samples up until 90 min were also analyzed using radio-HPLC in order to measure the fraction of parent compound and radiometabolites in the plasma. The plasma free fraction (f_P) of [^{11}C]UCB-J was measured using the equilibrium dialysis method: plasma collected from the study participant prior to the PET scan was spiked with the tracer and dialyzed against a buffer. Radioactivity was then measured in the plasma and buffer at 30, 60, 90, 120, 150, and 180 min, to get the buffer:plasma ratio. All radio-detection equipment was cross-calibrated to the PET scanner on a biweekly basis.

Table 3: PET acquisition and reconstruction settings

Parameter	Setting/value
Acquisition	
Transmission scan	6 min, pre-tracer injection
Tracer administration	Manual bolus injection (~20 s)
Acquisition mode	3D List mode
Reconstruction	
Method	3D-OP-OSEM (10 iterations, 16 subsets)
Attenuation correction	Maximum a posteriori transmission reconstruction (μ-map)
Matrix size	207 planes of 256 x 256 voxels
Voxels size	1.22 x 1.22 x 1.22 mm^3
Scan duration	120 min (40 frames)
Framing protocol	8 x 15 s, 8 x 30 s, 4 x 60 s, 5 x 120 s, 10 x 300 s, 5 x 300 s

9.3   PET & MRI preprocessing for Study I

In the first step, PET images underwent frame-by-frame motion correction using the AIR software with the reconcile command (Automated Image Registration, v. 5.2.5, LONI, UCLA, http://air.bmap.ucla.edu/AIR5/). Voxel movement was evaluated from the realigned frames, and a median movement < 3 mm was deemed acceptable.

The next step of the preprocessing was performed in FreeSurfer (Fischl, 2012)(v. 7.2, https://surfer.nmr.mgh.harvard.edu/) using the PETSurfer pipeline (Greve et al., 2014). This entailed standard anatomical processing of the T1-weighted MR images using the *recon-all* command within FreeSurfer. In the first step, the cortical surface was reconstructed, and T2-weighted MR images were used to refine the pial surface. The motion-corrected summation PET images were then coregistered to the MR images. Next, PET images were resampled onto the standard surface (*fsaverage*) and volume space (*MNI152*) and smoothed with 10 and 5 mm full-width at half-maximum, respectively.

Regional time activity curves (TACs) from non-smoothed data were extracted from regions of interest (ROI) based on eight subcortical grey matter regions defined by FreeSurfer (accumbens, amygdala, caudate, cerebellum cortex, hippocampus, putamen, thalamus, and ventral diencephalon), and cortical regions were created as averages within each of the 34 regions from the Desikan-Killiany atlas (Desikan et al., 2006).

9.4   PET & MRI preprocessing for Study II and III

T1 and T2 weighted images were used for segmentation into grey matte, white matter, and cerebrospinal fluid using the multispectral segmentation in SPM12 (Statistical Parametric Mapping, the Wellcome Centre for Human Neuroimaging, UCL, https://www.fil.ion.ucl.ac.uk/spm/).

Subsequent processing steps were conducted using the PVElab software pipeline (https://nru.dk/index.php/allcategories/category/30-software/). The motion-corrected summation PET image was co-registered to the corresponding T1-weighted image and segmented brain masks using SPM12. Cortical and subcortical ROIs were automatically defined as described by Svarer et al. (Svarer et al., 2005), and used to extract grey matter TACs. No partial volume correction was applied.

The ROI for the white matter region centrum semiovale was defined by using the PVElab Müeller-Gartner partial volume correction method followed by two rounds of 3D erosions to minimize partial volume effects. PET-MRI co-registration and placement of the ROIs were visually inspected for each subject; no manual correction was needed.

9.5   Kinetic modelling

For all three studies, kinetic modelling of [^{11}C]UCB-J PET and blood data was performed in *R* (v. 4.2.2, R Foundation, Vienna, Austria) using the *kinfitr* package (v. 0.6) (Tjerkaski et al., 2020).

For each participant, the metabolite-corrected arterial input function (AIF) was estimated as follows: first, radioactivity counts from the manual whole blood and plasma samples were used to establish a blood-to-plasma ratio curve, which was fitted using a cubic natural spline on the first four samples. Interpolated values were multiplied with the continuous whole-blood measurements, which was subsequently combined with the manual plasma samples from the later time points to estimate the full uncorrected plasma curve. Next, a Hill model was fitted to the unmetabolized [^{11}C]UCB-J in plasma (parent fraction) estimated from the radio-HPLC analysis, and subsequently multiplied to the plasma radioactivity curve, thus arriving at the metabolite-corrected AIF.

The main outcome for the [^{11}C]UCB-J PET quantification was total distribution volume (V_T). V_T values for all brain regions as well as cortical vertices and subcortical voxels were estimated with the 1TCM using the participants' individual metabolite-corrected AIF. The fraction of blood volume (v_B) was set to zero, as it did not improve the model fits or change V_T estimates, as was also concluded from initial [^{11}C]UCB-J evaluations (Finnema et al., 2017).

9.6   Autoradiography

Human brain regional SV2A density (B_{max}) was measured using [^{3}H]UCB-J autoradiography as described by (Raval, 2022). Tissue sections from post-mortem brains were obtained from the Bispebjerg Hospital Brain Bank (Bispebjerg-Frederiksberg Hospital, Copenhagen University Hospital, Denmark).

The tissue samples from seven healthy donors (mean age ± SD [range]: 84 ± 11 [68, 91] stored at -80 °C were cut with a cryostat to make sections with a thickness of 12 μm,

which were subsequently mounted on to SuperFrost Plus^{TM} microscope slides (Thermo Fisher Scientific, Waltham, MA, USA). Before the experiments, tissue sections representing grey and white matter of the frontal, parietal, temporal, and occipital cortex were thawed to room temperature pre-incubated twice for ten minutes in a buffer solution. The slides were then incubated for 60 min in buffer containing 20 nM [^{3}H]UCB-J, before being washed twice in wash-buffer and a final rinse with deionized water. The slides were then dried overnight and fixed in paraformaldehyde vapor chamber at 4 °C. The following day, slides were placed in autoradiography cassettes with radioactive tritium standards (ART0123, American Radiolabeled Chemical, Inc., St. Loui, MO, USA) and tritium-sensitive imaging plates (BAS-IP TR2040 E, Science Imaging Scandinavia AB, Nacka, Sweden). After 36 hours of exposure, the imaging plates were read with an Amersham™ Typhoon™ IP scanner (Cytiva, Uppsala, Sweden) at 10 µm resolution. Manual delineation of grey and white matter, image calibration and quantification was performed using ImageJ software (NIH Image, Bethesda, MD, USA) to convert mean pixel density to nCi/mg tissue equivalent (TE). These values were then decay corrected to convert to the unit pmol/g TE. A saturation binding study conducted with and without the addition of 10 mM of the UCB-J blocking agent levetiracetam showed similar grey matter non-specific binding and total binding in white matter, white matter was used as a proxy for non-specific binding.

Additional brain regions were included based on [^{11}C]UCB-J autoradiography estimates of SV2A from the literature (Varnäs et al., 2020). These estimates were converted from the unit kBq/mm^2 to pmol/g based on a linear regression equation modelled from the regions overlapping with the [^{3}H]UCB-J autoradiography regions.

9.7   mRNA data from the Allen Human Brain Atlas

Regional SV2A mRNA levels as a proxy for SV2A gene expression were obtained using the *abagen* toolbox (v 0.1.3), https://abagen.readthedocs.io (Markello et al., 2021). Six healthy donors with no history of brain conditions contributed to the data set available from the Allen Human Brain Atlas (AHBA), https://human.brain-map.org (Hawrylycz et al., 2012).

10.   Data analyses and statistics

10.1   Study I

Fist, SV2A estimates from [^{11}C]UCB-J PET and [^{3}H]UCB-J autoradiography were combined. To calculate the calibration factor between autoradiography and PET, regional [^{11}C]UCB-J PET estimates were compared with regional autoradiography estimates using a

linear regression model. The equation from the linear regression model was then used to calibrate the PET measurements for the regional and vertex outcomes to obtain PET-based brain maps in absolute protein densities. Subsequently, relationship between SV2A density and mRNA levels as an estimate of gene expression were evaluated with a Spearman correlation analysis. Finally, effects of the demographic variables age, sex, and IQ were assessed on the regional, vertex and voxel-based level again using linear regression models.

10.2 Study II

Group differences in $[^{11}C]$UCB-J V_T in the neocortex and the hippocampus between the escitalopram group and the placebo group were tested with two-tailed Welch two-sample t-tests. Cohen's d with Hedges correction was computed to estimate the effect sizes.

In a secondary analysis, we investigated the effect of intervention duration on $[^{11}C]$UCB-J V_T estimates for the hippocampus and the neocortex. We compared a linear regression model with a group-by-intervention duration term to a nested model without the group term. These models were also performed with age, sex, and IQ as covariates. Partial correlation coefficients (r_ρ) were derived from these models. Lastly, we used linear regression models to investigate the effects of s-escitalopram concentration (log-transformed) on $[^{11}C]$UCB-J V_T estimates. As a sensitivity analysis, we also conducted the above analyses with the randomization variables (age, sex, and IQ) as covariates.

10.3 Study III

Changes in $[^{11}C]$UCB-J V_T estimates between baseline and 1-week follow-up for the hippocampus and the frontal cortex were compared using one-tailed paired t-tests.

As exploratory analyses, we used correlation analyses to investigate whether change in $[^{11}C]$UCB-J V_T was associated with subjective ratings of the psychedelic experience rated immediately after the psilocybin session (MEQ30, EDI, ASC) and subjective persisting effects at 3-months follow-up (PEQ). Because of high intercorrelation between the items in the PEQ, a total sum-score was calculated for the positive and the negative items, respectively.

Results

In the following sections, a summary of the main results from Study I-III are presented. Full details are provided in each of the manuscripts (see Appendix).

11.   Study I

In study I, we aimed to create a high-resolution atlas of presynaptic density as index with SV2A. [^{11}C]UCB-J PET data and structural MRI data were obtained from 33 healthy participants in the CIMBI database; a summary of subject and [^{11}C]UCB-J PET imaging characteristics is presented in Table 4. We averaged regional [^{11}C]UCB-J V_T values and used linear regression between regional [^{3}H]UCB-J autoradiography and [^{11}C]UCB-J V_T estimates (mL/cm^3), see Figure 10. For the regression equation, $V_T = 3.56$ mL/cm^3 + 0.03 mL/cm^3/pmol/mL, the intercept estimate [SE] of 3.56 [2.18] mL/cm^3 represents the average non-displaceable compartment of [^{11}C]UCB-J binding (V_{ND}), while the slope estimate [SE] of 0.03 [0.005] represents the average [^{11}C]UCB-J plasma free fraction divided by the [^{11}C]UCB-J-SV2A dissociation constant (f_P/K_D).

Table 4. Study I: Demographics of the Study I PET cohort.

Sex (n, F/M)	17/16
Age (years)	27 ± 6 [20, 44]
IQ[a]	109 ± 7 [96, 125]
Injected dose (MBq)	400 ± 75 [224, 550]
Injected dose, adjusted (MBq/kg)	5.7 ± 1.4 [2.7, 9.7]
Injected mass, adjusted (ng/kg)	8.9 ± 13.4 [1.2, 80.9]

Values are mean ± SD [range]. [a]IQ score was available for 30 participants.
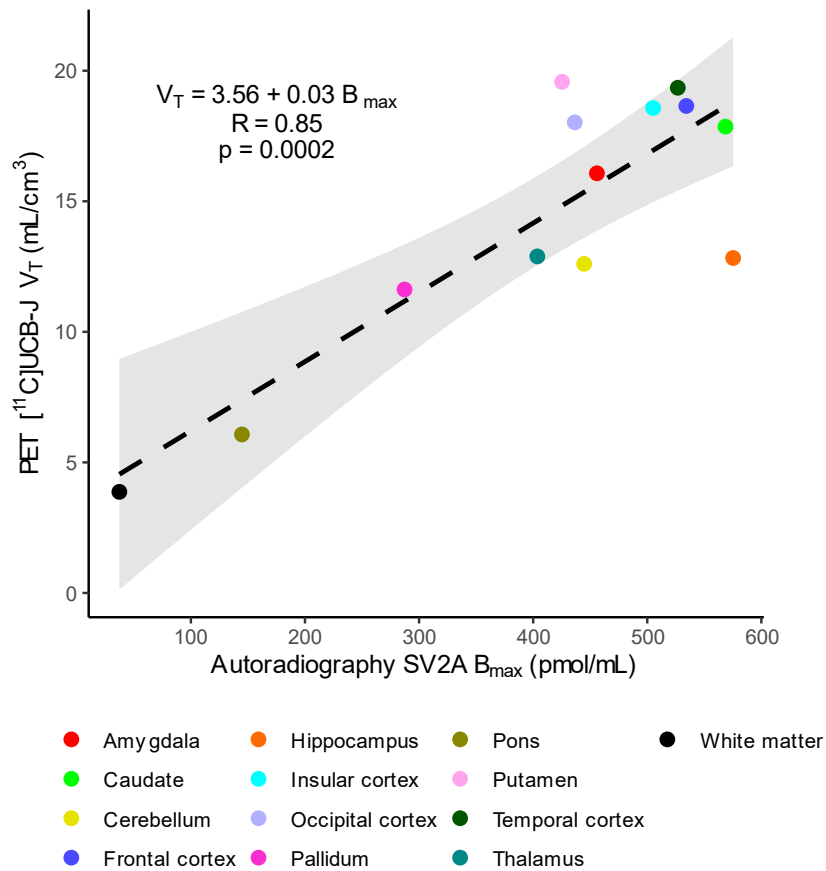
Figure 10. PET [^{11}C]UCB-J V_T vs autoradiography B_{max}. Average regional SV2A densities measured with [^{11}C]UCB-J PET (V_T; mL/cm^3) and autoradiography (B_{max}; pmol/mL) in brains from healthy participants/donors. The dashed line represents the regression line.

As autoradiography and PET-based estimates correlated well ($r = 0.85$, $p = 0.0002$), we used the linear equation to transform the [^{11}C]UCB-J V_T values into absolute density for all regions, vertices, and voxels. The resulting cortical and subcortical maps are presented in Figure 11. We observed the highest cortical binding in precuneus, posterior cingulate and parts of the temporal cortex, while the lowest binding was seen in the pre- and post-central gyri. For the subcortical regions, we observed highest binding in the putamen and caudate, and lower binding in the thalamus, pallidum, hippocampus, and cerebellum.
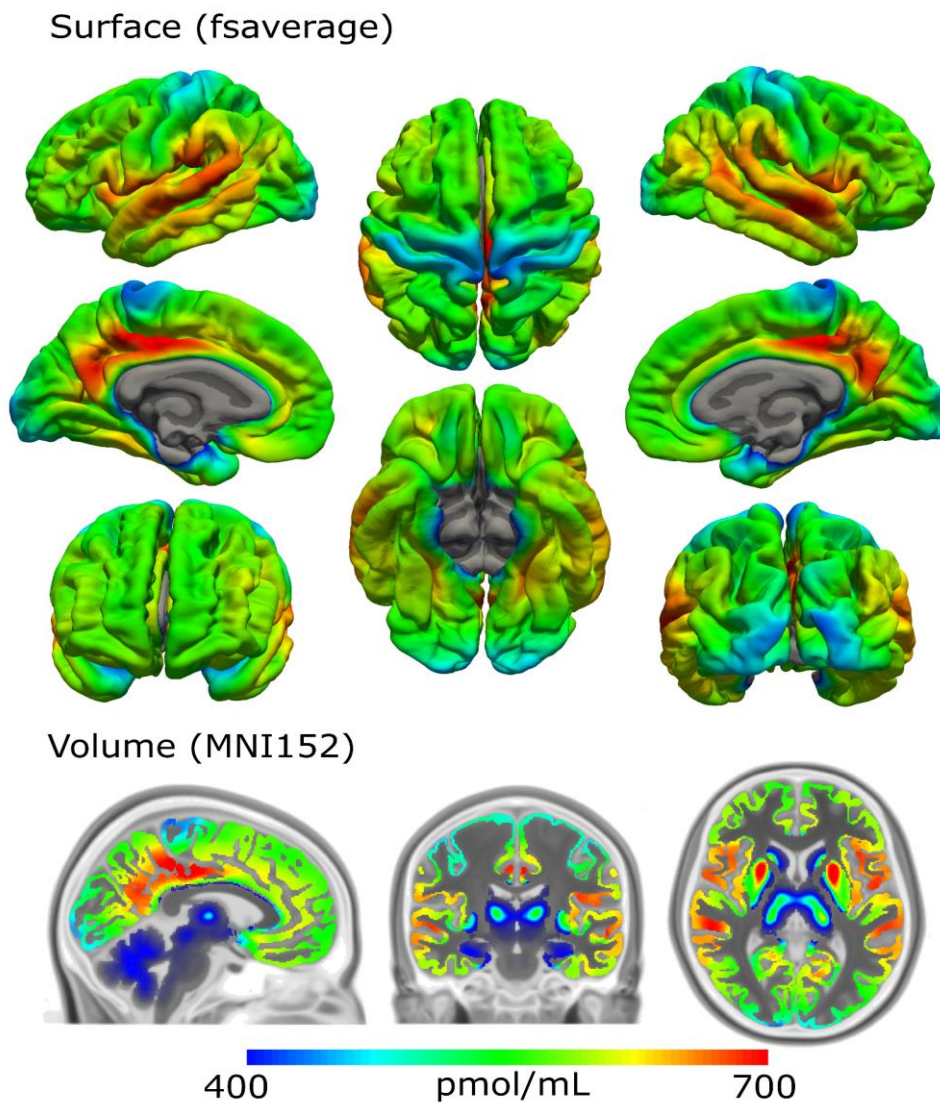
Figure 11. Brain maps of absolute SV2A density on the FreeSurfer *fsaverage* surface (top) and in the MNI152 volume space (bottom).

We found no association between regional SV2A densities and age, sex, and IQ (all corrected p-values > 0.13). We also did not find associations between cortical thickness /subcortical volumes and SV2A density (all corrected p-values > 0.69).

In a vertex-/voxel-wise analysis, we found positive associations between SV2A density and IQ in clusters located rather symmetrically in the parahippocampal gyri, orbitofrontal and temporal cortices (Figure 12)
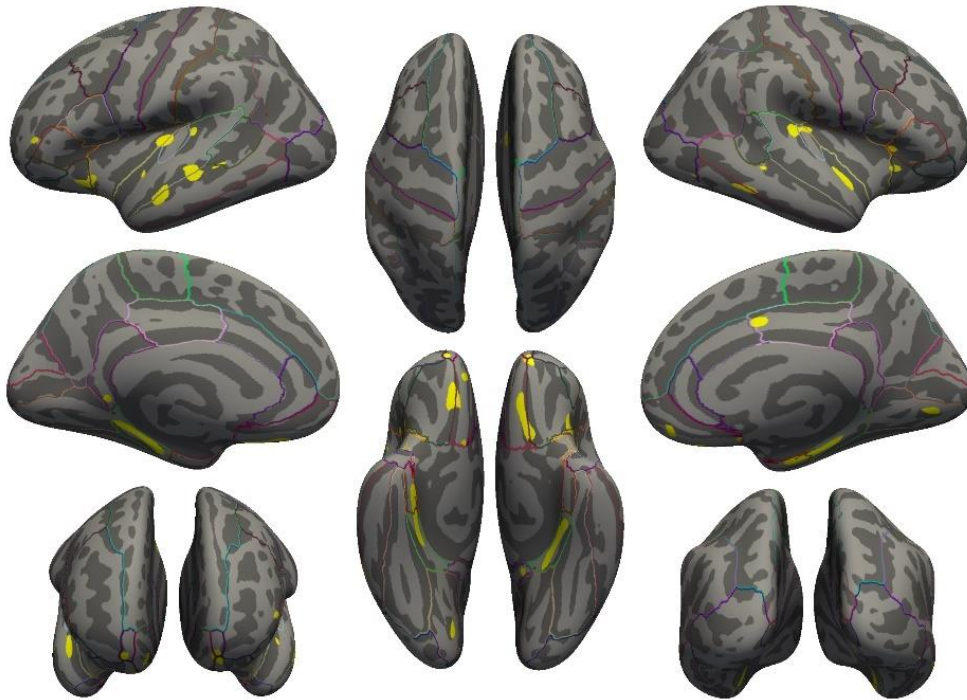
Figure 12. Inflated surface maps with projections of vertices that show positive association between SV2A density and IQ scores (n = 30). The colored lines show the borders of the regions defined by the Desikan-Killiany atlas.

Lastly, we investigated the association between regional *in vivo* SV2A density and regional mRNA levels. As evaluated with a Spearman correlation analysis, we found no association between SV2A density and mRNA level (Figure 13; $r = 0.10$, $p = 0.53$).
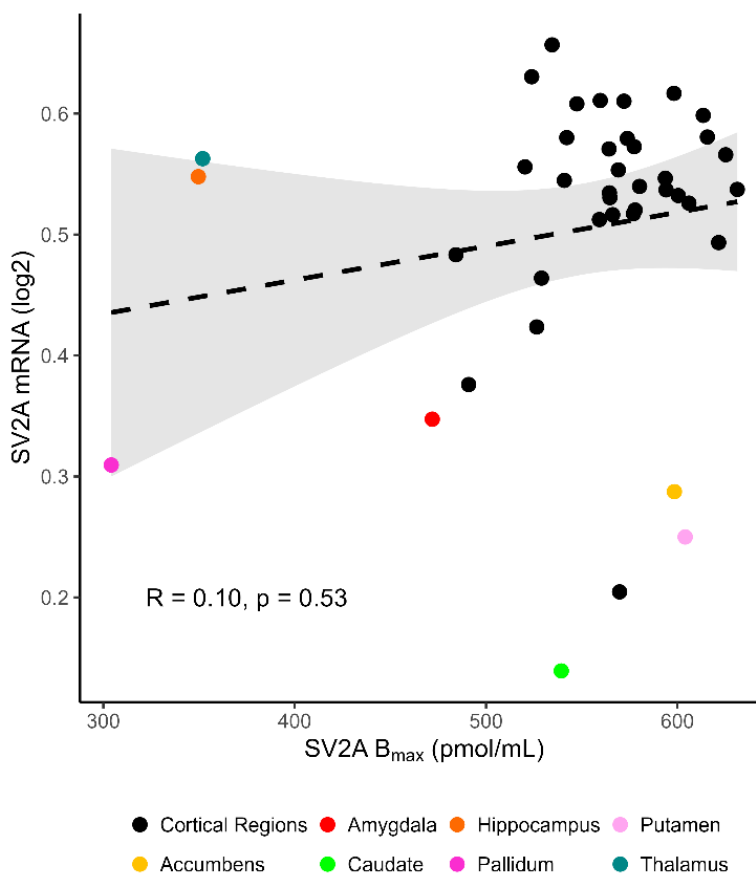
Figure 13. SV2A density vs SV2A mRNA levels. Average regional SV2A densities plotted against corresponding SV2A mRNA summary values ($\log_2$). The dashed line and shaded grey area represent the regression line and 95% CI for all brain regions. SV2A density and mRNA was not correlated, as evaluated with Spearman's correlation.

12. Study II

In study II, we investigated the effects of the SSRI escitalopram on synaptic density as indexed with [^{11}C]UCB-J PET. A summary of subject and [^{11}C]UCB-J PET imaging characteristics is presented in Table 5. There was no difference in [^{11}C]UCB-J free fraction, f_P, between the escitalopram and placebo group when controlling for age and sex ($\beta_{esc} = 0.01$, $p = 0.52$), and f_P was not associated with V_Ts in the neocortex ($\beta f_P = 7.0$ mL/cm^3, $p = 0.50$). Therefore, f_P was not used in the analyses.

Table 5. Subject demographics for Study II

	Placebo (N = 15[a])	Escitalopram (N = 17)	p-value
Female/male	8/7	12/5	0.52
Age (years)	22.8 ± 2.9 [19.9, 31.6]	25.2 ± 5.8 [19.6, 41.9]	0.15
IQ	108 ± 5.9 [94, 118]	112 ± 8.0 [99, 129]	0.11
Intervention duration (days)	30.4 ± 4.7 [22, 38]	28.2 ± 3.3 [24, 35]	0.14
S-escitalopram, day 10 (nmol/L)	0 ± 0 [0, 0]	86 ± 75 [28, 338]	-
S-escitalopram, follow-up (nmol/L)	0 ± 0 [0, 0]	84 ± 56 [28, 263]	-
Injected dose (MBq)	401 ± 101 [124, 550]	410 ± 63 [251, 526]	0.77
Injected mass (ng/kg)	12.2 ± 19.5 [1.2, 80.9]	8.9 ± 7.2 [1.4, 29.3]	0.53
f_P	0.36 ± 0.05 [0.29, 0.46]	0.36 ± 0.05 [0.26, 0.42]	0.87

Demographic characteristics of the study participants and related [^{11}C]UCB-J PET imaging parameters. Values are mean ± SD [range]. p-values refer to two-sample t-tests for continuous variables and chi-square tests for categorical variables. [a] Includes three participants in the placebo group who did not have a complete arterial input function. Group characteristics did not change noticeably when leaving out these participants.

12.1   Primary analyses

We did not find [^{11}C]UCB-J V_Ts in the hippocampus or the neocortex to be significantly higher in participant who had undergone intervention with escitalopram compared to placebo after an average intervention period of 29 days (Figure 14 and Table 6). Inclusion of the randomization variables, age, sex, and IQ, did not reveal any difference in [^{11}C]UCB-J V_T between the placebo and escitalopram group.
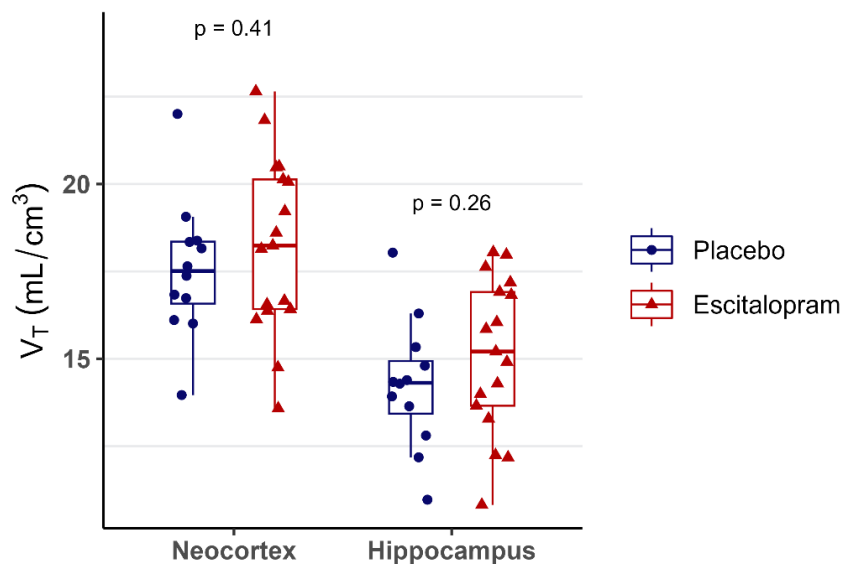
Figure 14. Comparison of [^{11}C]UCB-J binding in healthy individuals following 3-5 weeks of intervention with escitalopram (n = 17) or placebo (n = 12).

Table 6. Summary of results for Study II

	Placebo (n = 12)	Escitalopram (n = 17)	Mean difference	Cohen's d	p-value
Hippocampus	14.3 [1.9]	15.1 (2.2)	0.8 (5.6%)	0.43	0.26
Neocortex	17.6 (2.0)	18.3 (2.5)	0.7 (4.0%)	0.31	0.41

Summary of [^{11}C]UCB-J V_T estimates for the placebo and escitalopram group for the hippocampus and the neocortex. Groups were compared with a Welch two-sample t-test.

12.2 Secondary analyses

As a secondary analysis, we investigated if there was a time-dependent effect of escitalopram, i.e., if longer drug exposure was associated with higher [^{11}C]UCB-J V_T estimates. A likelihood-ratio test comparing a linear regression model with a *group-by-intervention duration* term to a nested model without the *group* term, indicated an improved model fit when *group* was included in the model: the test resulted in a p-value of 0.020 ($p_{adj.}$ = 0.039) for the neocortex and 0.058 ($p_{adj.}$ = 0.058) for the hippocampus. Examining the effects of *intervention duration* as estimated with the linear regression models, we saw a positive effect for the escitalopram group (Figure 15); in the neocortex the effect was estimated to be +0.41 mL/cm^3 per day (r_ρ = 0.46, p = 0.016) and in the hippocampus it was estimated to be +0.25 mL/cm^3 per day (r_ρ = 0.31, p = 0.11). In contrast, for the placebo group, the effect of *intervention duration* was -0.12 mL/cm^3 per day (r_ρ = -0.18, p = 0.38) for the neocortex, and -0.14 mL/cm^3 per day (r_ρ = -0.22, p = 0.26) for the hippocampus.

Our sensitivity analyses with age, sex, and IQ included as covariates, supported our findings: in the neocortex, the effect of intervention duration on [^{11}C]UCB-J V_T in the escitalopram group was +0.47 mL/cm^3 per day (r_ρ = 0.58, p = 0.003), and +0.30 mL/cm^3 per day (r_ρ = 0.40, p = 0.048) in the hippocampus. For the placebo group, the effect was -0.01 mL/cm^3 per day (r_ρ = -0.01, p = 0.95) in the neocortex and -0.06 mL/cm^3 per day (r_ρ = -0.11, p = 0.62) for the hippocampus.
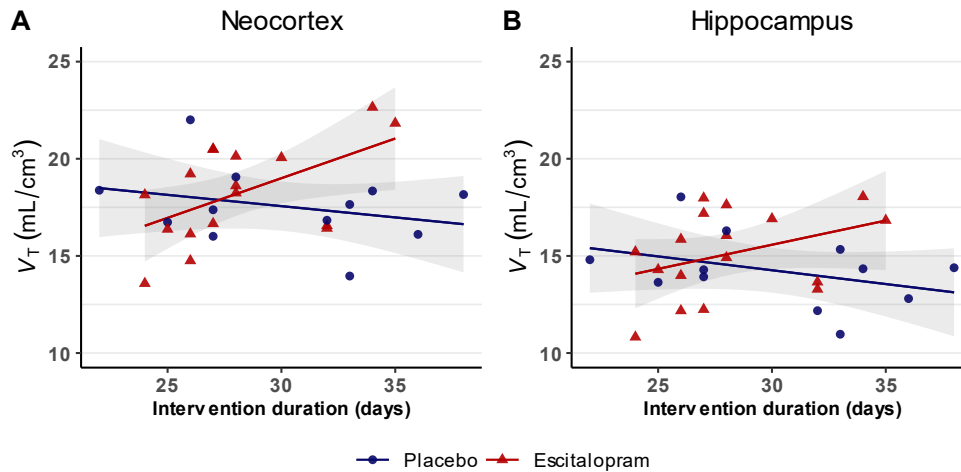
Figure 15. Effect of intervention duration. Relationship between [^{11}C]UCB-J binding (V_T) and the duration of the intervention for the placebo group (n = 12) and the escitalopram group (n = 17) in the neocortex (**A**) and the hippocampus (**B**). The shaded grey area represents the 95% CI.

We also investigated whether there was any association between the s-escitalopram concentration and [^{11}C]UCB-J V_T (Figure 16). For the neocortex, the estimated effect was +0.81 mL/cm^3 per log[ng/L] ($r_\rho = 0.18$, $p = 0.48$), and for the hippocampus it was and +0.39 mL/cm^3 per log[ng/L] ($r_\rho = 0.10$, $p = 0.70$). Our sensitivity analyses including age, sex, and IQ did not reveal any effects of s-escitalopram on [^{11}C]UCB-J V_{TS}.
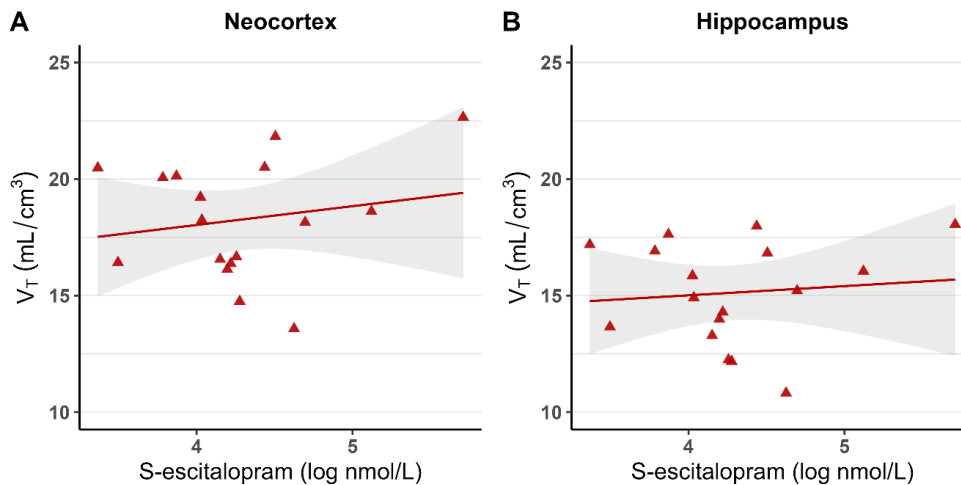
Figure 16. Effect of s-escitalopram. Relationship between s-escitalopram concentration and [^{11}C]UCB-J binding (V_T) in the escitalopram group for the neocortex (**A**) and the hippocampus (**B**).

13.   Study III

In study II, we investigated the effects of psilocybin on synaptic density as indexed with [^{11}C]UCB-J PET. A total of 15 healthy participants were scanned at baseline and one week after a moderate-high dose of psilocybin. A summary of participant demographics, subjective ratings of the psychedelic experience, and [^{11}C]UCB-J PET imaging characteristics is presented in Table 7. Twelve out of the fifteen participants had a complete AIF for both scans. There was no difference in the [^{11}C]UCB-J free fraction, f_P, between the baseline and 1-week follow-up scan ($p = 0.8$).

Table 7. Subject demographics for Study III

Age (years)	32.5 [26.6, 60.3]
Female/male	5/10
Mystical Type Experience (MEQ; 0-5)	2.97 [1.7, 5.0]
Ego-Dissolution Inventory (EDI; 0-100)	71.5 [2.4, 100]
Altered State of Consciousness (ASC; 0-100)	34.4 [10.0, 66.8]
Positive Persisting Effects (PEQ; 0-100)	28.6 [1.8, 77.8]
Negative Persisting Effects (PEQ; 0-100)	2.73 [0, 17.6]
Injected radioactivity dose (MBq)	
Baseline	413 [266, 481]
1-week follow-up	388 [89, 466]
Injected mass (ng/kg)	
Baseline	5.7 [1.5, 10.8]
1-week follow-up	3.1 [2.2, 10.6]
f_p	
Baseline	0.33 [0.22, 0.45]
1-week follow-up	0.33 [0.21, 0.44]

Values are presented as median [range].

13.1   Primary analyses

We did not find [^{11}C]UCB-J V_{TS} in the hippocampus or the frontal cortex to be significantly higher 1 week after psilocybin intervention. Individual estimates for baseline and follow-up are shown in Figure 17 and summarized in Table 8.
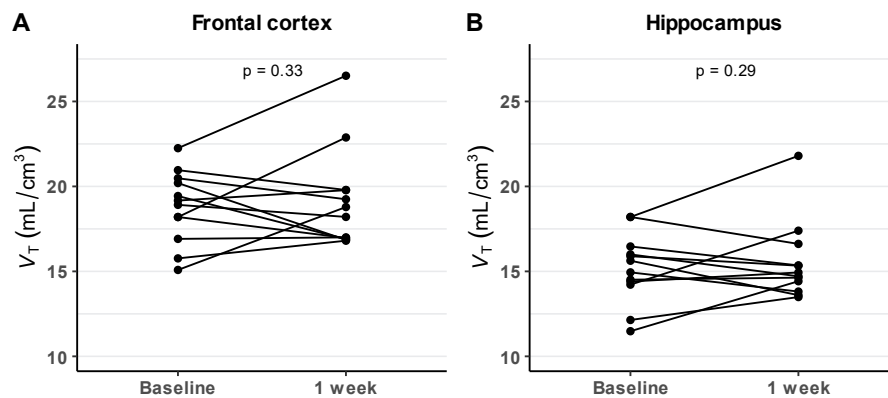
Figure 17. Study III main analysis. [^{11}C]UCB-J binding (V_T) estimates for the frontal cortex (**A**) and the hippocampus (**B**) at baseline and 1-week after psilocybin intervention compared with one-tailed *t*-tests.

Table 8. Summary of results for Study III.

	Baseline V_T (mL/cm^3)	Follow-up V_T (mL/cm^3)	Mean change (mL/cm^3)	Relative change (%)	*p*-value
Hippocampus	15.2 (2.1)	15.5 (2.3)	0.3 (2.0)	3.0 (13.5)	0.29
Frontal cortex	18.8 (2.1)	19.1 (2.9)	0.3 (2.6)	2.6 (14.1)	0.33

Summary of [^{11}C]UCB-J V_T estimates for the baseline and 1-week follow-up scans. Changes in V_T were compared using one-tailed, paired *t*-tests.

13.2 Exploratory analyses

Using correlation analyses, we investigated if changes in [^{11}C]UCB-J V_T were associated with subjective ratings of the psychedelic experience or persisting effects. For the questionnaires filled out immediately after the intervention session, we found no associations for the frontal cortex or the hippocampus: the MEQ30 total score (r < 0.38, *p* > 0.21), the EDI score (*r* < 0.35, *p* > 0.24), or the ASC mean score (*rho* < 0.09, *p* > 0.77). Among the MEQ30 and ASC sub facets, the largest positive effect sizes were observed for subscales measuring emotional facets (MEQ-Positive mood, ASC-Blissful state and ASC-Experience of unity), whereas purely sensory effects (e.g., ASC-Elementary imagery and ASC-Audio-visual synesthesia) showed smaller effect sizes (see supplementary material for paper III in the Appendix).

We further evaluated associations with persisting effects measured three months after the psilocybin intervention. Here, we correlated changes in [^{11}C]UCB-J V_T with a summed score of the positive and negative effects of the PEQ subscales, respectively. For the positive scores, we found no association (*r* < 0.27, *p* > 0.37, *rho* < 0.06, *p* > 43). For the negative sum score, we found a negative correlation for the hippocampus (*rho* = -0.62, *p* = 0.023) and the neocortex (*rho* = -0.69, *p* = 0.009).

Discussion

14. Study I

14.1 Combining in vivo and in vitro SV2A quantification

The brain atlas presented here builds on the combination of *in vivo* and *in vitro* neuroimaging methods, leveraging the strengths of one approach to compensate the shortcomings of the other. With PET, it is possible to image the entire brain in one acquisition, while physical and technical properties apply a limit to the spatial resolution. Further, the outcome measure is not an absolute concentration of the target protein, but is proportional to it. In contrast, autoradiography has excellent spatial resolution and provides estimate of absolute protein concentrations, but the methodology of working with 20 μm tissue sections renders whole brain quantification impossible using current techniques.

When combining PET and autoradiography to image the same target, we would expect the methods to agree, as was the case; we found a strong correlation between the average regional estimates of SV2A binding obtained with PET and autoradiography. The regional correlation and absolute SV2A densities found in our human data also agree with data from a validation study in the baboon brain experiment employing *in vivo* [^{11}C]UCB-J PET and *in vitro* homogenate binding (Finnema et al., 2016). In the baboon brain, SV2A density ranged from 111 pmol/mL brain tissue in the pons to 918 pmol/mL in the temporal cortex. Taken together, our results support the validity of using [^{11}C]UCB-J PET for human SV2A imaging, and for using the equation the linear regression model to calibrate our PET measures to absolute density, thus making it directly comparable to other microanatomical structures such as the density of neurons and neuroreceptors.

We found no correlation between regional *in vivo* SV2A density and SV2A gene expression as estimated with mRNA quantifications obtained from the Allen Human Brain atlas. This discrepancy is also observed for a range of neurotransmitter receptors and transporters (Beliveau et al., 2017; Hansen et al., 2022), and most likely reflects that SV2A is a presynaptic protein. A large proportion of axon terminals are located far from their respective cell soma which is the major site for mRNA translation and protein synthesis. Our finding thus underscores that SV2A mRNA quantification is not a valid proxy for SV2A protein density.

14.2   Cerebral SV2A distribution

Within the neocortex, highest SV2A density was observed in regions such as the posterior cingulate, precuneus, insular, and temporal cortices. Conversely, relatively lower density was observed within the lateral occipital and sensorimotor cortices, which encompass the primary areas of the primary visual, motor, and sensory regions. This observed trend – highest density in areas linked to associative functions and lowest density in core sensory and motor areas – mirrors the distribution patterns found for many neurotransmitter receptors (Beliveau et al., 2017; Zilles and Palomero-Gallagher, 2017). A similar pattern was observed in the putamen, which showed a rostral-caudal gradient, reflecting the associative and motor area distinctions.

Furthermore, a gradient in SV2A density was found within the sensorimotor cortex, corresponding to the somatotopic homunculus (Penfield and Boldrey, 1937; Gordon et al., 2023): medial areas associated with larger anatomical structures, like the trunk and legs, display lower SV2A density, while the density increased laterally where the cortical representation include structures responsible for more intricate motor functions, such as the hands and face, that also have higher sensory resolution. Interrupting this organization, a small pocket exhibiting slightly higher binding was observed mid-laterally in the central sulcus. This location appears to correspond with the recently identified Rolandic motor association area (Jensen et al., 2023), which is proposed to facilitate coordination between different body parts.

On the medial side, a patch of high binding stood out in an area involving the precuneus and part of the posterior cingulate cortex. The precuneus is an integral part of the default mode network as defined from functional connectivity studies using functional MRI (Raichle et al., 2001; Utevsky et al., 2014). The anterior part is involved in cognitive processes such as theory of mind and self-referential thinking, while the posterior part is involved in episodic memory and visuospatial imagery (Dadario and Sughrue, 2023). Structural and functional neuroimaging data has further implicated the precuneus in time orientation (Peer et al., 2015; Skye et al., 2023). Although many mental functions can be said to be uniquely human, the ones mentioned above lie at the core of what distinguishes humans from other species. Furthermore, comparative neuroanatomical literature suggest that cortical expansion of the precuneus region is a neurological specialization underlying recent human cognitive advancement (Bruner et al., 2017; Wei et al., 2019). The high SV2A density supports this as an area of either high complexity or capacity for neural activation and modulation.

The cortical gradient is further reflected in a study showing that higher-order cognitive networks, like the default mode network, express more human-accelerated region (HAR) genes than somato-motor and visual networks (Wei et al., 2019). These genes correlate with intellectual ability. It remains uncertain if increased synaptic density in certain areas relates to enhanced cognitive skill in healthy people, as observed in those with

neurodegenerative disorders (Mecca et al., 2022). Our preliminary analysis found links between IQ scores and SV2A density in areas such as the parahippocampal gyrus and temporal cortices. Some of these regions have ties to intelligence, evidenced by shared genetic origin with grey matter density (Pol et al., 2006) and complexity (Goriounova et al., 2018). This emphasizes the intricate neurobiology of cognitive abilities and the potential of SV2A imaging to explore these connections.

15.   Study II & III

In studies II and III, we investigated two different pharmacological interventions, the SSRI escitalopram and the 5-HT$_{2A}$R agonist psilocybin. Both drugs, despite their very different pharmacology and subjective effects, have been proposed to exert their effects by inducing neuroplasticity. The aim of the studies was to examine their effects on *in vivo* SV2A binding in health individuals as a proxy of synaptic plasticity.

15.1   Effects of escitalopram on cerebral SV2A binding

In study II, we employed a double-blind, randomized, placebo-controlled trial design to investigate the effect of an SSRI on cerebral SV2A binding in healthy individuals. Our primary analysis did not support our hypothesis that escitalopram intervention for 3-5 weeks would be associated with higher SV2A binding in the hippocampus and neocortex compared to placebo. The duration of the intervention period was chosen to mimic clinical practice and the timeframe of when symptom relief can generally be expected in patients who respond to the treatment (Kasper et al., 2006; Taylor et al., 2006; Gelenberg et al., 2010). However, potential limitations include the possibility that the detected effect size within our study's timeframe might be too subtle to detect. A larger sample or extended intervention period might be needed to properly detect the effects. In support of the latter, we found that escitalopram intervention had a time-dependent effect on SV2A binding; within the escitalopram group, a longer duration of the intervention was associated with higher SV2A binding. This effect was not present in the placebo group. Replicating the study with an extended time period is warranted for assessing the validity of the observed association and for mapping the dynamics more closely. For instance, we used linear regressions to evaluate the association with time, however, the trajectory likely would follow an S-shaped curve reflecting the baseline SV2A level initially, which would then be followed by a period of increasing SV2A density, and finally reaching a new plateau.

As the study was conducted in healthy participants, we cannot immediately extrapolate these results to how SSRIs work in clinical populations, such as individuals with

depression. However, as results from a previous study indicate an inverse correlation between the severity of depressive symptoms and SV2A levels (Holmes et al., 2019), it is reasonably to speculate that effects would be similar. It would be especially interesting to map SV2A in relation to changes in symptom severity over time. This could give some indications as to the causal direction (if any) between synaptic density and depression, as one could also imagine decreased synaptic density in depression could be a compensatory or protective mechanism.

In addition to the length of the intervention, the dosage of a drug is a key factor in intervention studies. Even with significant differences in drug concentration, there we saw no correlation between SV2A binding estimates and s-escitalopram concentration. This might be ascribed to our use of a high daily dose of 20 mg escitalopram, anticipated to achieve close to maximum occupancy of 70-80% of the serotonin transporter, as indicated by a recent meta-analysis (Sørensen et al., 2022).

We identified the hippocampus and neocortex as a priori regions of interests. However, it is possible that effects on SV2A and their temporal dynamics differ between brain regions, as has been seen in preclinical studies (Hajszan et al., 2005; Fritze et al., 2017). It is also important consider where in the brain effect can be expected given that SV2A is a presynaptic protein. For instance, SSRIs affect projection neurons in, e.g., the prefrontal cortex, the effects on SV2A could potentially manifest in the areas innervated by the prefrontal cortex rather than in the prefrontal cortex itself. Conversely, if SSRIs predominantly affect interneurons, effects could be expected within the frontal cortex.

15.2   Effects of psilocybin of cerebral SV2A binding

Our investigation into the effects of psilocybin on cerebral SV2A binding adopted a single-arm, open-label study model, with SV2A imaging conducted at baseline and one week post a single psilocybin intervention session. Contrary to our hypothesis, we observed no significant increase in SV2A binding in the hippocampus and frontal cortex. However, as SV2A is a presynaptic marker, it is possible that psilocybin could induce postsynaptic changes, which we would not detect. Recent preclinical studies have shown that psychedelic compounds promote structural neuroplasticity in rodents and cultured neurons as early as six hours after administration, and with persisting effects detected up to seven days later as (Ly et al., 2018, 2021; Shao et al., 2021; Moliner et al., 2023; Vargas et al., 2023). These studies focused mainly on dendritic structure and complexity, i.e., postsynaptic changes, but the presynaptic market VGLUT1 was also found to be upregulated 24 hours after drug administration in Ly et al. 2018. Our prior study in awake pigs found higher SV2A levels in the hippocampus 24 hours post psilocybin exposure, as detected using [^{3}H]UCB-J autoradiography, with possible prolonged effects observable within the hippocampus and the prefrontal cortex after a week (Raval et al., 2021). Although the evidence for neuroplastic

effects of psychedelics is more robust at the earlier time point, i.e., ≤ 24 hours, our focus was on the persisting effects of psilocybin. However, we cannot exclude that psilocybin could induce a transient increase in SV2A that is normalized after a week, or oppositely, that an increase would be detectable only at even later time points. As for the study on escitalopram, given that the participants receiving psilocybin were healthy, we cannot generalize the results to a population of patients with depression.

Studies indicate that positive experiences during the intervention session, specifically related to mystical-type experiences more so than purely sensory perceptual effects, are associated with greater antidepressant effects in patients with depression (Roseman et al., 2018) and lasting positive effects in healthy individuals (McCulloch et al., 2022; Søndergaard et al., 2022). Such findings lend support to the theory that the quality of the 'trip experience' mediates antidepressant effects. Yet, it is possible that subjective effects are an epiphenomenon, and that an association reflects the degree of receptor stimulation. To delve deeper into this question, we explored the relationship between subjective effects of psilocybin intervention and changes in SV2A binding. The total scores from the questionnaires characterizing the acute effects, the MEQ30, EDI, and ASC, were not associated with change in SV2A. Among the MEQ30 and ASC sub facets, the largest positive effect sizes were observed for subscales measuring emotional facets (MEQ-Positive mood, ASC-Blissful state and ASC-Experience of unity).

Individuals with decreased SV2A one week after psilocybin intervention tended to have more unfavorable mood and life attitude outcomes, as evaluated with the PEQ. The inverse relationship, an SV2A increase, was not related to positive persisting effects. However, as these investigations of the subjective effects are exploratory and done in a relatively small sample of healthy individuals, the findings should be interpreted with caution and replicated in future studies.

15.3 Considerations regarding study design

Strengths and limitations of the two studies deserve to be mentioned. First, the sample sizes in both studies were small, as is often the case in PET studies. This makes it difficult to detect smaller effects and poses a risk of false negative results. Paradoxically, the risks of false positive results also increase with small sample sizes, as has been theoretically argued (Button et al., 2013) and empirically demonstrated for brain-wide association studies (Marek et al., 2022). However, an important strength that works to counteract the limitations of small studies, is the use of intervention designs which (theoretically) provides a stronger basis for causal inference than in mere observational studies. Furthermore, as our studies are the first of their kind in humans, effects sizes could only be projected based on pre-clinical data or similar human studies. Moreover, as radioactivity is administered to the study participants, there is an ethical reason to limit the number of included participant.

In the escitalopram study, we did not measure SV2A binding at baseline. While this might appear as a limitation, the randomized nature of the study supports the assumption of no differences between the groups at baseline. Further, employing a test-rest design could pose a different challenge; in a previous study using [^{11}C]UCB-J PET, a significant negative bias at 28-day rescans as compared to baseline was reported (Tuncel et al., 2020, 2022). This phenomenon has also been observed for other tracers (Leurquin-Sterk et al., 2016). It is unclear if this is due to biological or methodological reasons, or simply by chance, but it could hamper the sensitivity of studies employing a test-retest setup like our psilocybin study.

16. Imaging synaptic plasticity with [^{11}C]UCB-J PET

16.1 SV2A as a synaptic marker

No single biomarker will ever be able to capture all relevant aspects of a biological structure or function. Thus, the properties, limitations, and pitfalls of a given biomarker should be kept in mind and, ideally, investigated just as vigorously as the biological question that the biomarker is used to solve. As such, SV2A as a biomarker deserves some reflection.

The use of SV2A as a proxy for synaptic density caries the implicit assumption that SV2A is present in all synapses and that the number vesicles times the copy number of SV2A molecules per vesicle is the same for all synapses. However, the term synaptic density itself is even somewhat vague, as it could be defined either as the number of *synapse units* (as visualized in Figure 2) per tissue volume or the *synapse volume or surface area* per tissue volume. This distinction is important as a brain with large synapses containing a large number of synaptic vesicles might result in a similar SV2A density estimate as would be seen in a brain a higher number of smaller synapses. Consequently, observing higher SV2A density following an intervention could represent newly formed synapses, enlarged synapses, increased number of vesicles per synapse, or increased number of SV2A molecules in each vesicle. These different aspects of SV2A density also mean that an observed change following a pharmacological challenge could reflect different synaptic alterations depending on the time-frame.

To date, only few imaging studies have investigated effects of interventions on SV2A density, and thus the question of how modifiable SV2A is, remains large unanswered. A recent clinical trial found no effect of ketamine on SV2A binding measured with [^{11}C]UCB-J PET 24 hours after the drug intervention (Holmes et al., 2022). The study further reported no effects in non-human primates at the timepoints 24 hours, 1 week and 4-6 week after the intervention. Although technically not an interventional study, Angarita et al. recently

showed that in cocaine use disorder, SV2A binding was inversely correlated with the length of cocaine abstinence, while the overall years of cocaine use didn't significantly influence SV2A binding. In a preclinical study, cocaine was found to increase SV2A binding (Rossi et al., 2023). While these investigations are preliminary, they hint at whether SV2A functions more as a dynamic state indicator or a consistent trait marker of synapses.

Lastly, for imaging techniques such as PET that rely on binding interactions between the target protein and the radioligand, the affinity of the ligand is assumed to be the same across subjects and clinical populations. However, proteins are complex 3-dimensionel structures that often exert their function by interacting with other cellular structures and undergoing conformational changes. Thus, it is worth considering if synaptic vesicle protein interactions could lead to changes in tracer affinity, thereby explaining an observed difference in SV2A binding. Similar considerations are relevant for drug intervention studies or medicated patients. Typically, only drugs that are able to block the binding site for the tracer will be considered a hindrance for PET imaging. However, an SV2A positive allosteric modulator has been developed and shown to increase the SV2A binding affinity of two [^{11}C]UCB-J analogues, namely the anti-epileptic drugs levetiracetam and brivaracetam (Wood and Gillard, 2017). As such, potential changes in the tracer's affinity should be considered for studies investigating drugs as well as brain pathology.

Conclusion

The main objectives of this thesis were to implement SV2A PET neuroimaging with the radiotracer [11C]UCB-J in humans, characterize the SV2A distribution in the brain, and employ the method to investigate synaptic plasticity in relation to pharmacological intervention with the SSRI escitalopram and the psychedelic compound psilocybin.

In Study I, the robust correlation between [11C]UCB-J V_T estimates and the absolute SV2A protein density, as determined by autoradiography, underscores the validity of [11C]UCB-J for SV2A imaging. However, when compared with SV2A mRNA data from the Allen Human Brain Atlas, regional ranking was not preserved, implying that SV2A mRNA levels are not a reliable proxy for SV2A protein density. In terms of *in vivo* SV2A distribution, the atlas unveiled pronounced cortical and subcortical gradients in SV2A density. These gradients not only reflect functional topography but also mirror cortical hierarchies, with a progressive increase from primary motor and sensory regions to advanced associative cortical areas.

In Study II, we could not confirm our primary hypothesis of higher SV2A binding in healthy individuals after an average of four weeks of intervention with the SSRI escitalopram compared to placebo. The results of our secondary analyses indicated a time-dependent effect of escitalopram om SV2A density in that longer duration of escitalopram intervention was associated with higher SV2A binding, while no association was seen for serum escitalopram concentration. These results suggest that over 3-5 weeks, escitalopram may induce synaptic neuroplasticity in the human brain. Although replication of the findings is warranted, the time-dependent effect offers a biological explanation for the delayed response commonly observed in patients treated with SSRIs.

In Study III, our data did not support our primary hypothesis of increased SV2A binding one week after a single intervention with a moderate-to-high dose of psilocybin in healthy individuals. Our exploratory analyses delving into the relationship between SV2A changes and subjective effects during the intervention indicate that aspects tied to positive emotional experiences may be stronger predictors of SV2A binding alterations than solely sensory experiences.

17.   Future perspectives

The exploration of SV2A quantification through combining *in vivo* and *in vitro* methods and the subsequent exploration of its dynamics related to pharmacological intervention with both SSRIs and psychedelics has brought to light several intriguing

findings and implications. Nevertheless, the outlined work is just one step towards disentangling the complex field of synaptic plasticity in the human brain. The experience and insights gained from working on these studies have led to reflections and perspectives on the following issues:

Temporal dynamics of synaptic changes: The pharmacological interventions with SSRIs and psychedelics in our studies highlight the importance of understanding the temporal dynamics of synaptic changes. Future studies should be designed with particular consideration regarding the time of synaptic imaging. Based on our study, future studies of conventional antidepressants are suggested to employ intervention periods of at least 5 weeks, to maximize the likelihood of detecting differences.

Investigations in clinical populations: The work presented here involved healthy individuals, thus raising the question of how the findings translate to clinical populations such as patients with depression. In designing such studies, one should keep in mind that the temporal dynamics might differ from healthy populations. Although placebo-controlled trials pose a challenge due to ethical concerns, dose-variations or changes in symptom scores as outcomes can be utilized to maximize contrasts and inference.

Selecting the region of interest: While we selected the hippocampus and neocortex as regions of interest based on previous SV2A investigations and their known involvement in mood regulation and cognition, it remains an open question if certain regions are more prone to changes in presynaptic density. The hippocampus, although often the focus in neuroplasticity research might not be the most likely region for detecting changes in SV2A signal due to its tissue heterogeneity.

Technological advances: Elaborating on the previous point, increasing resolution of PET imaging together with refinements in segmentation of structural imaging with MRI will provide a higher spatial resolution. This will increase feasibility for detecting more subtle and focal differences such as in neuron subpopulations or hippocampus subfields.

Expanding to other synaptic markers: As much research in neuroplasticity following exposure to psychedelics focus on postsynaptic structural changes, development of postsynaptic density markers may allow for a more nuanced understanding of neuroplastic changes.

Interdisciplinary inquiries: As the field of synaptic imaging with radioligands targeting the SV2A is relatively young, much can still be learned from fields outside of PET imaging. It is critical to better understand the SV2A in order to correctly interpret results obtained with PET. An example could be to perform high-resolution [^{3}H]UCB-J autoradiography to characterize SV2A density in hippocampal subfields, as has been done for multiple neurotransmitter receptors (Zilles and Palomero-Gallagher, 2017; Palomero-Gallagher et al., 2020). Ultimately, insights from all fields spanning protein conformation and interactions to synaptic vesicle release dynamics and capacity should be gathered as a scientific input function to be convolved with well-designed PET studies.

References

Angarita, G. A., Worhunsky, P. D., Naganawa, M., Toyonaga, T., Nabulsi, N. B., Li, C. R., et al. (2022). Lower prefrontal cortical synaptic vesicle binding in cocaine use disorder: An exploratory 11C-UCB-J positron emission tomography study in humans. *Addict Biol* 27, e13123. doi: 10.1111/adb.13123.

Armand, S. (2022). Affective cognition and brain serotonin in healthy individuals. *University of Copenhagen*. Available at: https://nru.dk/index.php/testmenu/category/4-phd-theses.

Azevedo, F. A. C., Carvalho, L. R. B., Grinberg, L. T., Farfel, J. M., Ferretti, R. E. L., Leite, R. E. P., et al. (2009). Equal numbers of neuronal and nonneuronal cells make the human brain an isometrically scaled-up primate brain. *J Comp Neurol* 513, 532–541. doi: 10.1002/cne.21974.

Azmitia, E. C. (2020). Chapter 1 Evolution of serotonin: sunlight to suicide. *Handb. Behav. Neurosci.* 31, 3–22. doi: 10.1016/b978-0-444-64125-0.00001-3.

Bajjalieh, S., Frantz, G., Weimann, J., McConnell, S., and Scheller, R. (1994). Differential expression of synaptic vesicle protein 2 (SV2) isoforms. *J Neurosci* 14, 5223–5235. doi: 10.1523/jneurosci.14-09-05223.1994.

Banks, M. I., Zahid, Z., Jones, N. T., Sultan, Z. W., and Wenthur, C. J. (2021). Catalysts for change: the cellular neurobiology of psychedelics. *Mol. Biol. Cell* 32, 1135–1144. doi: 10.1091/mbc.e20-05-0340.

Barrett, F. S., Johnson, M. W., and Griffiths, R. R. (2015). Validation of the revised Mystical Experience Questionnaire in experimental sessions with psilocybin. *J. Psychopharmacol.* 29, 1182–1190. doi: 10.1177/0269881115609019.

Beliveau, V., Ganz, M., Feng, L., Ozenne, B., Højgaard, L., Fisher, P. M., et al. (2017). A High-Resolution In Vivo Atlas of the Human Brain's Serotonin System. *J Neurosci* 37, 120–128. doi: 10.1523/jneurosci.2830-16.2016.

Branchi, I. (2011). The double edged sword of neural plasticity: Increasing serotonin levels leads to both greater vulnerability to depression and improved capacity to recover. *Psychoneuroendocrino* 36, 339–351. doi: 10.1016/j.psyneuen.2010.08.011.

Bruner, E., Preuss, T. M., Chen, X., and Rilling, J. K. (2017). Evidence for expansion of the precuneus in human evolution. *Brain Struct. Funct.* 222, 1053–1060. doi: 10.1007/s00429-015-1172-y.

Button, K. S., Ioannidis, J. P. A., Mokrysz, C., Nosek, B. A., Flint, J., Robinson, E. S. J., et al. (2013). Power failure: why small sample size undermines the reliability of neuroscience. *Nat. Rev. Neurosci.* 14, 365–376. doi: 10.1038/nrn3475.

Calder, A. E., and Hasler, G. (2023). Towards an understanding of psychedelic-induced neuroplasticity. *Neuropsychopharmacol* 48, 104–112. doi: 10.1038/s41386-022-01389-z.

Carhart-Harris, R., Giribaldi, B., Watts, R., Baker-Jones, M., Murphy-Beiner, A., Murphy, R., et al. (2021). Trial of Psilocybin versus Escitalopram for Depression. *New Engl J Med* 384, 1402–1411. doi: 10.1056/nejmoa2032994.

Carhart-Harris, R. L., Bolstridge, M., Day, C. M. J., Rucker, J., Watts, R., Erritzoe, D. E., et al. (2018). Psilocybin with psychological support for treatment-resistant depression: six-month follow-up. *Psychopharmacology* 235, 399–408. doi: 10.1007/s00213-017-4771-x.

Carhart-Harris, R. L., Bolstridge, M., Rucker, J., Day, C. M. J. J., Erritzoe, D., Kaelen, M., et al. (2016). Psilocybin with psychological support for treatment-resistant depression: An open-label feasibility study. *Lancet Psychiatry* 3, 619--627. doi: 10.1016/s2215-0366(16)30065-7.

Carson, R. E. (2000). PET physiological measurements using constant infusion. *Nucl. Med. Biol.* 27, 657–660. doi: 10.1016/s0969-8051(00)00138-4.

Chen, M.-K., Mecca, A. P., Naganawa, M., Finnema, S. J., Toyonaga, T., Lin, S., et al. (2018). Assessing Synaptic Density in Alzheimer Disease With Synaptic Vesicle Glycoprotein 2A Positron Emission Tomographic Imaging. *Jama Neurol* 75, 1215. doi: 10.1001/jamaneurol.2018.1836.

Chu, A., and Wadhwa, R. (2023). "Selective Serotonin Reuptake Inhibitors.," in *StatPearls* (StatPearls Publishing).

Cornea-Hébert, V., Riad, M., Wu, C., Singh, S. K., and Descarries, L. (1999). Cellular and subcellular distribution of the serotonin 5-HT2A receptor in the central nervous system of adult rat. *J. Comp. Neurol.* 409, 187–209. doi: 10.1002/(sici)1096-9861(19990628)409:2<187::aid-cne2>3.0.co;2-p.

Dadario, N. B., and Sughrue, M. E. (2023). The functional role of the precuneus. *Brain* 146, 3598–3607. doi: 10.1093/brain/awad181.

Davis, A. K., Barrett, F. S., May, D. G., Cosimano, M. P., Sepeda, N. D., Johnson, M. W., et al. (2021). Effects of Psilocybin-Assisted Therapy on Major Depressive Disorder. *Jama Psychiat* 78, 481–489. doi: 10.1001/jamapsychiatry.2020.3285.

Delva, A., Laere, K. V., and Vandenberghe, W. (2023). Longitudinal Imaging of Regional Brain Volumes, SV2A, and Glucose Metabolism In Huntington's Disease. *Mov. Disord.* doi: 10.1002/mds.29501.

Desikan, R. S., Ségonne, F., Fischl, B., Quinn, B. T., Dickerson, B. C., Blacker, D., et al. (2006). An automated labeling system for subdividing the human cerebral cortex on MRI scans into gyral based regions of interest. *Neuroimage* 31, 968–980. doi: 10.1016/j.neuroimage.2006.01.021.

D'Souza, D. C., Radhakrishnan, R., Naganawa, M., Ganesh, S., Nabulsi, N., Najafzadeh, S., et al. (2021). Preliminary in vivo evidence of lower hippocampal synaptic density in cannabis use disorder. *Mol Psychiatr* 26, 3192–3200. doi: 10.1038/s41380-020-00891-4.

Duman, R. S., and Aghajanian, G. K. (2012). Synaptic Dysfunction in Depression: Potential Therapeutic Targets. *Science* 338, 68–72. doi: 10.1126/science.1222939.

Erritzoe, D., Roseman, L., Nour, M. M., MacLean, K., Kaelen, M., Nutt, D. J., et al. (2018). Effects of psilocybin therapy on personality structure. *Acta Psychiat Scand* 138, 368–378. doi: 10.1111/acps.12904.

Ettrup, A., Cunha-Bang, S. da, McMahon, B., Lehel, S., Dyssegaard, A., Skibsted, A. W., et al. (2014). Serotonin 2A Receptor Agonist Binding in the Human Brain with [11C]Cimbi-36. *J Cereb Blood Flow Metabolism* 34, 1188–1196. doi: 10.1038/jcbfm.2014.68.

Finnema, S. J., Nabulsi, N. B., Eid, T., Detyniecki, K., Lin, S., Chen, M.-K., et al. (2016). Imaging synaptic density in the living human brain. *Sci Transl Med* 8, 348ra96. doi: 10.1126/scitranslmed.aaf6667.

Finnema, S. J., Nabulsi, N. B., Mercier, J., Lin, S., Chen, M.-K., Matuskey, D., et al. (2017). Kinetic evaluation and test–retest reproducibility of [11C]UCB-J, a novel radioligand for positron emission tomography imaging of synaptic vesicle glycoprotein 2A in humans. *J Cereb Blood Flow Metabolism* 38, 2041–2052. doi: 10.1177/0271678x17724947.

Finnema, S. J., Toyonaga, T., Detyniecki, K., Chen, M., Dias, M., Wang, Q., et al. (2020). Reduced synaptic vesicle protein 2A binding in temporal lobe epilepsy: A [11C]UCB-J positron emission tomography study. *Epilepsia* 61, 2183–2193. doi: 10.1111/epi.16653.

Fischl, B. (2012). FreeSurfer. *Neuroimage* 62, 774–781. doi: 10.1016/j.neuroimage.2012.01.021.

Fritze, S., Spanagel, R., and Noori, H. R. (2017). Adaptive dynamics of the 5-HT systems following chronic administration of selective serotonin reuptake inhibitors: a meta-analysis. *J Neurochem* 142, 747–755. doi: 10.1111/jnc.14114.

Gabriel, F. C., Melo, D. O. de, Fráguas, R., Leite-Santos, N. C., Silva, R. A. M. da, and Ribeiro, E. (2020). Pharmacological treatment of depression: A systematic review comparing clinical practice guideline recommendations. *Plos One* 15, e0231700. doi: 10.1371/journal.pone.0231700.

García-Font, N., Martín, R., Torres, M., Oset-Gasque, M. J., and Sánchez-Prieto, J. (2019). The loss of β adrenergic receptor mediated release potentiation in a mouse model of fragile X syndrome. *Neurobiol. Dis.* 130, 104482. doi: 10.1016/j.nbd.2019.104482.

Gaspar, P., Cases, O., and Maroteaux, L. (2003). The developmental role of serotonin: news from mouse molecular genetics. *Nat Rev Neurosci* 4, 1002–1012. doi: 10.1038/nrn1256.

Gelenberg, A. J., Freeman, M. P., Markowitz, J. C., Rosenbaum, J. F., Thase, M. E., Trivedi, M. H., et al. (2010). Treatment of Patients With Major Depressive Disorder. Available at: https://psychiatryonline.org/pb/assets/raw/sitewide/practice_guidelines/guidelines/mdd.pdf [Accessed September 6, 2022].

Gordon, E. M., Chauvin, R. J., Van, A. N., Rajesh, A., Nielsen, A., Newbold, D. J., et al. (2023). A somato-cognitive action network alternates with effector regions in motor cortex. *Nature* 617, 351–359. doi: 10.1038/s41586-023-05964-2.

Goriounova, N. A., Heyer, D. B., Wilbers, R., Verhoog, M. B., Giugliano, M., Verbist, C., et al. (2018). Large and fast human pyramidal neurons associate with intelligence. *eLife* 7, e41714. doi: 10.7554/elife.41714.

Greve, D. N., Svarer, C., Fisher, P. M., Feng, L., Hansen, A. E., Baare, W., et al. (2014). Cortical surface-based analysis reduces bias and variance in kinetic modeling of brain PET data. *Neuroimage* 92, 225–236. doi: 10.1016/j.neuroimage.2013.12.021.

Griffiths, R. R., Richards, W. A., McCann, U., and Jesse, R. (2006). Psilocybin can occasion mystical-type experiences having substantial and sustained personal meaning and spiritual significance. *Psychopharmacology* 187, 268–283. doi: 10.1007/s00213-006-0457-5.

Gunn, R. N., Gunn, S. R., and Cunningham, V. J. (2001). Positron Emission Tomography Compartmental Models. *J. Cereb. Blood Flow Metab.* 21, 635–652. doi: 10.1097/00004647-200106000-00002.

Hajszan, T., MacLusky, N. J., and Leranth, C. (2005). Short-term treatment with the antidepressant fluoxetine triggers pyramidal dendritic spine synapse formation in rat hippocampus. *Eur J Neurosci* 21, 1299–1303. doi: 10.1111/j.1460-9568.2005.03968.x.

Hansen, J. Y., Markello, R. D., Tuominen, L., Nørgaard, M., Kuzmin, E., Palomero-Gallagher, N., et al. (2022). Correspondence between gene expression and neurotransmitter receptor and transporter density in the human brain. *NeuroImage* 264, 119671. doi: 10.1016/j.neuroimage.2022.119671.

Hawrylycz, M. J., Lein, E. S., Guillozet-Bongaarts, A. L., Shen, E. H., Ng, L., Miller, J. A., et al. (2012). An anatomically comprehensive atlas of the adult human brain transcriptome. *Nature* 489, 391–399. doi: 10.1038/nature11405.

Hiroyama, S., Rokugawa, T., Ito, M., Iimori, H., Morita, I., Maeda, H., et al. (2020). Quantitative evaluation of hepatic integrin αvβ3 expression by positron emission tomography imaging using 18F-FPP-RGD2 in rats with non-alcoholic steatohepatitis. *EJNMMI Res.* 10, 118. doi: 10.1186/s13550-020-00704-3.

Holmes, S. E., Finnema, S. J., Naganawa, M., DellaGioia, N., Holden, D., Fowles, K., et al. (2022). Imaging the effect of ketamine on synaptic density (SV2A) in the living brain. *Mol Psychiatr* 27, 2273–2281. doi: 10.1038/s41380-022-01465-2.

Holmes, S. E., Scheinost, D., Finnema, S. J., Naganawa, M., Davis, M. T., DellaGioia, N., et al. (2019). Lower synaptic density is associated with depression severity and network alterations. *Nat Commun* 10, 1529. doi: 10.1038/s41467-019-09562-7.

Jensen, M. A., Huang, H., Valencia, G. O., Klassen, B. T., Boom, M. A. van den, Kaufmann, T. J., et al. (2023). A motor association area in the depths of the central sulcus. *Nat. Neurosci.* 26, 1165–1169. doi: 10.1038/s41593-023-01346-z.

Johansen, A., Hansen, H. D., Svarer, C., Lehel, S., Leth-Petersen, S., Kristensen, J. L., et al. (2018). The importance of small polar radiometabolites in molecular neuroimaging: A PET study with [11C]Cimbi-36 labeled in two positions. *J Cereb Blood Flow Metabolism* 38, 659–668. doi: 10.1177/0271678x17746179.

Kasper, S., Spadone, C., Verpillat, P., and Angst, J. (2006). Onset of action of escitalopram compared with other antidepressants: results of a pooled analysis. *Int Clin Psychopharm* 21, 105–110. doi: 10.1097/01.yic.0000194375.42589.c3.

Kometer, M., Schmidt, A., Bachmann, R., Studerus, E., Seifritz, E., and Vollenweider, F. X. (2012). Psilocybin Biases Facial Recognition, Goal-Directed Behavior, and Mood State Toward Positive Relative

to Negative Emotions Through Different Serotonergic Subreceptors. *Biol Psychiat* 72, 898–906. doi: 10.1016/j.biopsych.2012.04.005.

Koole, M., Aalst, J. van, Devrome, M., Mertens, N., Serdons, K., Lacroix, B., et al. (2019). Quantifying SV2A density and drug occupancy in the human brain using [11C]UCB-J PET imaging and subcortical white matter as reference tissue. *Eur J Nucl Med Mol I* 46, 396–406. doi: 10.1007/s00259-018-4119-8.

Kraus, C., Castrén, E., Kasper, S., and Lanzenberger, R. (2017). Serotonin and neuroplasticity – Links between molecular, functional and structural pathophysiology in depression. *Neurosci Biobehav Rev* 77, 317–326. doi: 10.1016/j.neubiorev.2017.03.007.

Langley, C., Armand, S., Luo, Q., Savulich, G., Segerberg, T., Søndergaard, A., et al. (2023). Chronic escitalopram in healthy volunteers has specific effects on reinforcement sensitivity: a double-blind, placebo-controlled semi-randomised study. *Neuropsychopharmacology* 48, 664–670. doi: 10.1038/s41386-022-01523-x.

Laurell, G. L., Plavén-Sigray, P., Jucaite, A., Varrone, A., Cosgrove, K. P., Svarer, C., et al. (2021). Nondisplaceable Binding Is a Potential Confounding Factor in 11C-PBR28 Translocator Protein PET Studies. *J Nucl Med* 62, 412–417. doi: 10.2967/jnumed.120.243717.

Leurquin-Sterk, G., Postnov, A., Laat, B. de, Casteels, C., Celen, S., Crunelle, C. L., et al. (2016). Kinetic modeling and long-term test-retest reproducibility of the mGluR5 PET tracer 18F-FPEB in human brain. *Synapse* 70, 153–162. doi: 10.1002/syn.21890.

Lu, Y., Toyonaga, T., Naganawa, M., Gallezot, J.-D., Chen, M.-K., Mecca, A. P., et al. (2021). Partial volume correction analysis for 11C-UCB-J PET studies of Alzheimer's disease. *Neuroimage* 238, 118248. doi: 10.1016/j.neuroimage.2021.118248.

Ly, C., Greb, A. C., Cameron, L. P., Wong, J. M., Barragan, E. V., Wilson, P. C., et al. (2018). Psychedelics Promote Structural and Functional Neural Plasticity. *Cell Reports* 23, 3170–3182. doi: 10.1016/j.celrep.2018.05.022.

Ly, C., Greb, A. C., Vargas, M. V., Duim, W. C., Grodzki, A. C. G., Lein, P. J., et al. (2021). Transient Stimulation with Psychoplastogens Is Sufficient to Initiate Neuronal Growth. *ACS Pharmacol. Transl. Sci.* 4, 452–460. doi: 10.1021/acsptsci.0c00065.

Madsen, M. K., Fisher, P. M., Burmester, D., Dyssegaard, A., Stenbæk, D. S., Kristiansen, S., et al. (2019). Psychedelic effects of psilocybin correlate with serotonin 2A receptor occupancy and plasma psilocin levels. *Neuropsychopharmacol* 44, 1328–1334. doi: 10.1038/s41386-019-0324-9.

Mak, E., Holland, N., Jones, P. S., Savulich, G., Low, A., Malpetti, M., et al. (2021). In vivo coupling of dendritic complexity with presynaptic density in primary tauopathies. *Neurobiol Aging* 101, 187–198. doi: 10.1016/j.neurobiolaging.2021.01.016.

Mansur, A., Rabiner, E. A., Comley, R. A., Lewis, Y., Middleton, L. T., Huiban, M., et al. (2020). Characterization of 3 PET Tracers for Quantification of Mitochondrial and Synaptic Function in Healthy Human Brain: 18F-BCPP-EF, 11C-SA-4503, and 11C-UCB-J. *J Nucl Med* 61, 96–103. doi: 10.2967/jnumed.119.228080.

Marek, S., Tervo-Clemmens, B., Calabro, F. J., Montez, D. F., Kay, B. P., Hatoum, A. S., et al. (2022). Reproducible brain-wide association studies require thousands of individuals. *Nature* 603, 654–660. doi: 10.1038/s41586-022-04492-9.

Markello, R. D., Arnatkeviciute, A., Poline, J.-B., Fulcher, B. D., Fornito, A., and Misic, B. (2021). Standardizing workflows in imaging transcriptomics with the abagen toolbox. *Elife* 10. doi: 10.7554/elife.72129.

Matuskey, D., Tinaz, S., Wilcox, K. C., Naganawa, M., Toyonaga, T., Dias, M., et al. (2020). Synaptic Changes in Parkinson Disease Assessed with in vivo Imaging. *Ann Neurol.* 87, 329–338. doi: 10.1002/ana.25682.

McCulloch, D. E.-W., Grzywacz, M. Z., Madsen, M. K., Jensen, P. S., Ozenne, B., Armand, S., et al. (2022). Psilocybin-Induced Mystical-Type Experiences are Related to Persisting Positive Effects: A Quantitative and Qualitative Report. *Front Pharmacol* 13, 841648. doi: 10.3389/fphar.2022.841648.

Mecca, A. P., O'Dell, R. S., Sharp, E. S., Banks, E. R., Bartlett, H. H., Zhao, W., et al. (2022). Synaptic density and cognitive performance in Alzheimer's disease: A PET imaging study with [11C]UCB-J. *Alzheimer's Dementia* 18, 2527–2536. doi: 10.1002/alz.12582.

Mendoza-Torreblanca, J. G., Vanoye-Carlo, A., Phillips-Farfán, B. V., Carmona-Aparicio, L., and Gómez-Lira, G. (2013). Synaptic vesicle protein 2A: basic facts and role in synaptic function. *Eur J Neurosci* 38, 3529–3539. doi: 10.1111/ejn.12360.

Mercier, J., Archen, L., Bollu, V., Carré, S., Evrard, Y., Jnoff, E., et al. (2014). Discovery of Heterocyclic Nonacetamide Synaptic Vesicle Protein 2A (SV2A) Ligands with Single-Digit Nanomolar Potency: Opening Avenues towards the First SV2A Positron Emission Tomography (PET) Ligands. *Chemmedchem* 9, 693–698. doi: 10.1002/cmdc.201300482.

Mertens, N., Maguire, R. P., Serdons, K., Lacroix, B., Mercier, J., Sciberras, D., et al. (2020). Validation of Parametric Methods for [11C]UCB-J PET Imaging Using Subcortical White Matter as Reference Tissue. *Mol Imaging Biol* 22, 444–452. doi: 10.1007/s11307-019-01387-6.

Messell, C., Summer, L., Bonde, L. O., Beck, B. D., and Stenbæk, D. S. (2022). Music programming for psilocybin-assisted therapy: Guided Imagery and Music-informed perspectives. *Front Psychol* 13, 873455. doi: 10.3389/fpsyg.2022.873455.

Michiels, L., Delva, A., Aalst, J. van, Ceccarini, J., Vandenberghe, W., Vandenbulcke, M., et al. (2021). Synaptic density in healthy human aging is not influenced by age or sex: a 11C-UCB-J PET study. *Neuroimage* 232, 117877. doi: 10.1016/j.neuroimage.2021.117877.

Miner, L. A. H., Backstrom, J. R., Sanders-Bush, E., and Sesack, S. R. (2003). Ultrastructural localization of serotonin2A receptors in the middle layers of the rat prelimbic prefrontal cortex. *Neuroscience* 116, 107–117. doi: 10.1016/s0306-4522(02)00580-8.

Moliner, R., Girych, M., Brunello, C. A., Kovaleva, V., Biojone, C., Enkavi, G., et al. (2023). Psychedelics promote plasticity by directly binding to BDNF receptor TrkB. *Nat. Neurosci.*, 1–10. doi: 10.1038/s41593-023-01316-5.

Morris, E. D., Endres, C. J., Schmidt, K. C., Christian, B. T., Jr., R. F. M., and Fisher, R. E. (2004). "Kinetic modeling in positron emission tomography.," in *Emission tomography: The Fundamentals of PET and SPECT*, eds. W. MN and A. JN (Elsevier Academic Press).

Mutch, S. A., Kensel-Hammes, P., Gadd, J. C., Fujimoto, B. S., Allen, R. W., Schiro, P. G., et al. (2011). Protein Quantification at the Single Vesicle Level Reveals That a Subset of Synaptic Vesicle Proteins Are Trafficked with High Precision. *J Neurosci* 31, 1461–1470. doi: 10.1523/jneurosci.3805-10.2011.

Nabulsi, N. B., Mercier, J., Holden, D., Carré, S., Najafzadeh, S., Vandergeten, M.-C., et al. (2016). Synthesis and Preclinical Evaluation of 11C-UCB-J as a PET Tracer for Imaging the Synaptic Vesicle Glycoprotein 2A in the Brain. *J Nucl Med* 57, 777–784. doi: 10.2967/jnumed.115.168179.

Naganawa, M., Gallezot, J.-D., Finnema, S. J., Matuskey, D., Mecca, A., Nabulsi, N. B., et al. (2021). Simplified Quantification of 11C-UCB-J PET Evaluated in a Large Human Cohort. *J Nucl Med* 62, 418–421. doi: 10.2967/jnumed.120.243949.

Nichols, D. E. (2016). Psychedelics. *Pharmacol Rev* 68, 264–355. doi: 10.1124/pr.115.011478.

Nørgaard, M., Ganz, M., Svarer, C., Frokjaer, V. G., Greve, D. N., Strother, S. C., et al. (2019a). Different preprocessing strategies lead to different conclusions: A [11C]DASB-PET reproducibility study. *J Cereb Blood Flow Metabolism* 40, 1902–1911. doi: 10.1177/0271678x19880450.

Nørgaard, M., Ganz, M., Svarer, C., Frokjaer, V. G., Greve, D. N., Strother, S. C., et al. (2019b). Optimization of preprocessing strategies in Positron Emission Tomography (PET) neuroimaging: A [11C]DASB PET study. *Neuroimage* 199, 466–479. doi: 10.1016/j.neuroimage.2019.05.055.

Nour, M. M., Evans, L., Nutt, D., and Carhart-Harris, R. L. (2016). Ego-Dissolution and Psychedelics: Validation of the Ego-Dissolution Inventory (EDI). *Front. Hum. Neurosci.* 10, 269. doi: 10.3389/fnhum.2016.00269.

Nowack, A., Yao, J., Custer, K. L., and Bajjalieh, S. M. (2010). SV2 regulates neurotransmitter release via multiple mechanisms. *Am J Physiol-cell Ph* 299, C960–C967. doi: 10.1152/ajpcell.00259.2010.

O'Dell, R. S., Naganawa, M., Toyonaga, T., Young, J., Dahal, R., Singh, E., et al. (2020). Validation of a simplified tissue-to-reference ratio measurement using SUVR for the assessment of synaptic density alterations in Alzheimer's disease using [11C]UCB-J PET. *Alzheimer's Dementia* 16. doi: 10.1002/alz.045928.

Olson, D. E. (2022). Biochemical Mechanisms Underlying Psychedelic-Induced Neuroplasticity. *Biochemistry-us* 61, 127–136. doi: 10.1021/acs.biochem.1c00812.

Onwordi, E. C., Halff, E. F., Whitehurst, T., Mansur, A., Cotel, M.-C., Wells, L., et al. (2020). Synaptic density marker SV2A is reduced in schizophrenia patients and unaffected by antipsychotics in rats. *Nat Commun* 11, 246.

Owens, M. J., Knight, D. L., and Nemeroff, C. B. (2001). Second-generation SSRIs: human monoamine transporter binding profile of escitalopram and R-fluoxetine. *Biol. Psychiatry* 50, 345–350. doi: 10.1016/s0006-3223(01)01145-3.

Pakkenberg, B., and Gundersen, H. J. G. (1997). Neocortical neuron number in humans: Effect of sex and age. *J Comp Neurol* 384, 312–320. doi: 10.1002/(sici)1096-9861(19970728)384:2<312::aid-cne10>3.0.co;2-k.

Palomero-Gallagher, N., Kedo, O., Mohlberg, H., Zilles, K., and Amunts, K. (2020). Multimodal mapping and analysis of the cyto- and receptorarchitecture of the human hippocampus. *Brain Struct. Funct.* 225, 881–907. doi: 10.1007/s00429-019-02022-4.

Pazarlar, B. A., Aripaka, S. S., Petukhov, V., Pinborg, L., Khodosevich, K., and Mikkelsen, J. D. (2022). Expression profile of synaptic vesicle glycoprotein 2A, B, and C paralogues in temporal neocortex tissue from patients with temporal lobe epilepsy (TLE). *Mol Brain* 15, 45. doi: 10.1186/s13041-022-00931-w.

Peer, M., Salomon, R., Goldberg, I., Blanke, O., and Arzy, S. (2015). Brain system for mental orientation in space, time, and person. *Proc. Natl. Acad. Sci.* 112, 11072–11077. doi: 10.1073/pnas.1504242112.

Penfield, W., and Boldrey, E. (1937). Somatic motor and sensory representation in the cerebral cortex of man as studied by electrical stimulation. *Brain* 60, 389–443. doi: 10.1093/brain/60.4.389.

Pol, H. E. H., Schnack, H. G., Posthuma, D., Mandl, R. C. W., Baaré, W. F., Oel, C. van, et al. (2006). Genetic Contributions to Human Brain Morphology and Intelligence. *J. Neurosci.* 26, 10235–10242. doi: 10.1523/jneurosci.1312-06.2006.

Quednow, B. B., Kometer, M., Geyer, M. A., and Vollenweider, F. X. (2012). Psilocybin-Induced Deficits in Automatic and Controlled Inhibition are Attenuated by Ketanserin in Healthy Human Volunteers. *Neuropsychopharmacol* 37, 630–640. doi: 10.1038/npp.2011.228.

Radhakrishnan, R., Skosnik, P. D., Ranganathan, M., Naganawa, M., Toyonaga, T., Finnema, S., et al. (2021). In vivo evidence of lower synaptic vesicle density in schizophrenia. *Mol Psychiatr* 26, 7690–7698. doi: 10.1038/s41380-021-01184-0.

Raichle, M. E., MacLeod, A. M., Snyder, A. Z., Powers, W. J., Gusnard, D. A., and Shulman, G. L. (2001). A default mode of brain function. *Proc. Natl. Acad. Sci.* 98, 676–682. doi: 10.1073/pnas.98.2.676.

Raval, N. R. (2022). Translational Positron Emission Tomography - Animal Models and In Vitro Autoradiography for Radioligand Development. Available at: https://nru.dk/index.php/testmenu/category/4-phd-theses.

Raval, N. R., Johansen, A., Donovan, L. L., Ros, N. F., Ozenne, B., Hansen, H. D., et al. (2021). A Single Dose of Psilocybin Increases Synaptic Density and Decreases 5-HT2A Receptor Density in the Pig Brain. *Int J Mol Sci* 22, 835. doi: 10.3390/ijms22020835.

Roseman, L., Nutt, D. J., and Carhart-Harris, R. L. (2018). Quality of Acute Psychedelic Experience Predicts Therapeutic Efficacy of Psilocybin for Treatment-Resistant Depression. *Front Pharmacol* 8, 974. doi: 10.3389/fphar.2017.00974.

Rossano, S., Toyonaga, T., Finnema, S. J., Naganawa, M., Lu, Y., Nabulsi, N., et al. (2019). Assessment of a white matter reference region for 11C-UCB-J PET quantification. *J Cereb Blood Flow Metabolism* 40, 1890–1901. doi: 10.1177/0271678x19879230.

Rossi, R., Bærentzen, S. L., Thomsen, M. B., Real, C. C., Wegener, G., Grassi-Oliveira, R., et al. (2023). A single dose of cocaine raises SV2A density in hippocampus of adolescent rats. *Acta Neuropsychiatr*, 1–23. doi: 10.1017/neu.2023.14.

Rush, A. J., Trivedi, M. H., Wisniewski, S. R., Nierenberg, A. A., Stewart, J. W., Warden, D., et al. (2006). Acute and Longer-Term Outcomes in Depressed Outpatients Requiring One or Several Treatment Steps: A STAR*D Report. *Am J Psychiat* 163, 1905–1917. doi: 10.1176/ajp.2006.163.11.1905.

Salvan, P., Fonseca, M., Winkler, A. M., Beauchamp, A., Lerch, J. P., and Johansen-Berg, H. (2023). Serotonin regulation of behavior via large-scale neuromodulation of serotonin receptor networks. *Nat Neurosci* 26, 53–63. doi: 10.1038/s41593-022-01213-3.

Serrano, M. E., Kim, E., Petrinovic, M. M., Turkheimer, F., and Cash, D. (2022). Imaging Synaptic Density: The Next Holy Grail of Neuroscience? *Front Neurosci-switz* 16, 796129. doi: 10.3389/fnins.2022.796129.

Shao, L.-X., Liao, C., Gregg, I., Davoudian, P. A., Savalia, N. K., Delagarza, K., et al. (2021). Psilocybin induces rapid and persistent growth of dendritic spines in frontal cortex in vivo. *Neuron* 109, 2535-2544.e4. doi: 10.1016/j.neuron.2021.06.008.

Silbereis, J. C., Pochareddy, S., Zhu, Y., Li, M., and Sestan, N. (2016). The Cellular and Molecular Landscapes of the Developing Human Central Nervous System. *Neuron* 89, 248–268. doi: 10.1016/j.neuron.2015.12.008.

Skye, J., Bruss, J., Herbet, G., Tranel, D., and Boes, A. D. (2023). Localization of a Medial Temporal Lobe—Precuneus Network for Time Orientation. *Ann. Neurol.* 94, 421–433. doi: 10.1002/ana.26681.

Smart, K., Liu, H., Matuskey, D., Chen, M.-K., Torres, K., Nabulsi, N., et al. (2020). Binding of the synaptic vesicle radiotracer [11C]UCB-J is unchanged during functional brain activation using a visual stimulation task. *J Cereb Blood Flow Metabolism* 41, 1067–1079. doi: 10.1177/0271678x20946198.

Søndergaard, A., Madsen, M. K., Ozenne, B., Armand, S., Knudsen, G. M., Fisher, P. M., et al. (2022). Lasting increases in trait mindfulness after psilocybin correlate positively with the mystical-type experience in healthy individuals. *Front Psychol* 13, 948729. doi: 10.3389/fpsyg.2022.948729.

Sørensen, A., Ruhé, H. G., and Munkholm, K. (2022). The relationship between dose and serotonin transporter occupancy of antidepressants—a systematic review. *Mol Psychiatr* 27, 192–201. doi: 10.1038/s41380-021-01285-w.

Stenbæk, D. S., Madsen, M. K., Ozenne, B., Kristiansen, S., Burmester, D., Erritzoe, D., et al. (2021). Brain serotonin 2A receptor binding predicts subjective temporal and mystical effects of psilocybin in healthy humans. *J Psychopharmacol* 35, 459–468. doi: 10.1177/0269881120959609.

Stout, K. A., Dunn, A. R., Hoffman, C., and Miller, G. W. (2019). The Synaptic Vesicle Glycoprotein 2: Structure, Function, and Disease Relevance. *Acs Chem Neurosci* 10, 3927–3938. doi: 10.1021/acschemneuro.9b00351.

Studerus, E., Gamma, A., and Vollenweider, F. X. (2010). Psychometric Evaluation of the Altered States of Consciousness Rating Scale (OAV). *PLoS ONE* 5, e12412. doi: 10.1371/journal.pone.0012412.

Svarer, C., Madsen, K., Hasselbalch, S. G., Pinborg, L. H., Haugbøl, S., Frøkjær, V. G., et al. (2005). MR-based automatic delineation of volumes of interest in human brain PET images using probability maps. *Neuroimage* 24, 969–979. doi: 10.1016/j.neuroimage.2004.10.017.

Takamori, S., Holt, M., Stenius, K., Lemke, E. A., Grønborg, M., Riedel, D., et al. (2006). Molecular Anatomy of a Trafficking Organelle. *Cell* 127, 831–846. doi: 10.1016/j.cell.2006.10.030.

Taylor, M. J., Freemantle, N., Geddes, J. R., and Bhagwagar, Z. (2006). Early Onset of Selective Serotonin Reuptake Inhibitor Antidepressant Action: Systematic Review and Meta-analysis. *Arch Gen Psychiat* 63, 1217–1223. doi: 10.1001/archpsyc.63.11.1217.

Tjerkaski, J., Cervenka, S., Farde, L., and Matheson, G. J. (2020). Kinfitr — an open-source tool for reproducible PET modelling: validation and evaluation of test-retest reliability. *EJNMMI Res* 10, 77. doi: 10.1186/s13550-020-00664-8.

Tuncel, H., Boellaard, R., Coomans, E. M., Hollander-Meeuwsen, M. den, Vries, E. F. J. de, Glaudemans, A. W. J. M., et al. (2022). Validation and test–retest repeatability performance of parametric methods for [11C]UCB-J PET. *EJNMMI Res* 12, 3. doi: 10.1186/s13550-021-00874-8.

Tuncel, H., Boellaard, R., Coomans, E. M., Vries, E. F. de, Glaudemans, A. W., Feltes, P. K., et al. (2020). Kinetics and 28-day test–retest repeatability and reproducibility of [11C]UCB-J PET brain imaging. *J Cereb Blood Flow Metabolism* 41, 1338–1350. doi: 10.1177/0271678x20964248.

Umemori, J., Winkel, F., Didio, G., Pou, M. L., and Castrén, E. (2018). iPlasticity: Induced juvenile-like plasticity in the adult brain as a mechanism of antidepressants. *Psychiat Clin Neuros* 72, 633–653. doi: 10.1111/pcn.12683.

Utevsky, A. V., Smith, D. V., and Huettel, S. A. (2014). Precuneus Is a Functional Core of the Default-Mode Network. *J. Neurosci.* 34, 932–940. doi: 10.1523/jneurosci.4227-13.2014.

Vargas, M. V., Dunlap, L. E., Dong, C., Carter, S. J., Tombari, R. J., Jami, S. A., et al. (2023). Psychedelics promote neuroplasticity through the activation of intracellular 5-HT2A receptors. *Science* 379, 700–706. doi: 10.1126/science.adf0435.

Varnäs, K., Stepanov, V., and Halldin, C. (2020). Autoradiographic mapping of synaptic vesicle glycoprotein 2A in non-human primate and human brain. *Synapse* 74, e22157. doi: 10.1002/syn.22157.

Vollenweider, F. X., Vollenweider-Scherpenhuyzen, M. F. I., Bäbler, A., Vogel, H., and Hell, D. (1998). Psilocybin induces schizophrenia-like psychosis in humans via a serotonin-2 agonist action. *Neuroreport* 9, 3897–3902. doi: 10.1097/00001756-199812010-00024.

Vos, C. M. H. de, Mason, N. L., and Kuypers, K. P. C. (2021). Psychedelics and Neuroplasticity: A Systematic Review Unraveling the Biological Underpinnings of Psychedelics. *Frontiers Psychiatry* 12, 724606. doi: 10.3389/fpsyt.2021.724606.

Wall, M. B., Harding, R., Zafar, R., Rabiner, E. A., Nutt, D. J., and Erritzoe, D. (2023). Neuroimaging in psychedelic drug development: past, present, and future. *Mol. Psychiatry*, 1–8. doi: 10.1038/s41380-023-02271-0.

Wei, Y., Lange, S. C. de, Scholtens, L. H., Watanabe, K., Ardesch, D. J., Jansen, P. R., et al. (2019). Genetic mapping and evolutionary analysis of human-expanded cognitive networks. *Nat. Commun.* 10, 4839. doi: 10.1038/s41467-019-12764-8.

Wood, M. D., and Gillard, M. (2017). Evidence for a differential interaction of brivaracetam and levetiracetam with the synaptic vesicle 2A protein. *Epilepsia* 58, 255–262. doi: 10.1111/epi.13638.

Zhong, H., Haddjeri, N., and Sánchez, C. (2012). Escitalopram, an antidepressant with an allosteric effect at the serotonin transporter—a review of current understanding of its mechanism of action. *Psychopharmacology* 219, 1–13. doi: 10.1007/s00213-011-2463-5.

Zhornitsky, S., Oliva, H. N. P., Jayne, L. A., Allsop, A. S. A., Kaye, A. P., Potenza, M. N., et al. (2023). Changes in synaptic markers after administration of ketamine or psychedelics: a systematic scoping review. *Front. Psychiatry* 14, 1197890. doi: 10.3389/fpsyt.2023.1197890.

Zilles, K., and Palomero-Gallagher, N. (2017). Multiple Transmitter Receptors in Regions and Layers of the Human Cerebral Cortex. *Front Neuroanat* 11, 78. doi: 10.3389/fnana.2017.00078.

Appendix

[A]   Study I

Johansen, A.*, Beliveau, V.*, Colliander, E., Raval, N.R., Dam, V.H., Gillings, N., Aznar, S., Svarer, C., Plavén-Sigray, P., & Knudsen, G. M. An *in vivo* high-resolution human brain atlas of synaptic density. *Submitted to Journal of Neuroscience September 2023*

[B]   Study II

Johansen, A., Armand, S., Plavén-Sigray, P., Nasser, A., Ozenne, B., Petersen, I. N., Keller, S. H., Madsen, J., Møller, K., Vassilieva, A., Langley, C., Svarer, C., Stenbæk, D. S., Sahakian, B. J. & Knudsen, G. M. (2023). Effects of escitalopram on synaptic density in the human brain: A randomized controlled trial. *Molecular Psychiatry. 2023. (E-pub ahead of print)*

[C]   Study III

Johansen, A., Plavén-Sigray, P., Madsen, M.K., Søndergaard, A., Messel, C., Grzywacz, M., Nasser, A., McCulloch, D.E., Beliveau, V., Vassilieva, A., Lund, A., Lehel, S., Stenbæk, D. S., Fisher, P., Svarer, C., & Knudsen, G. M. Effects of psilocybin on synaptic density in the human brain. *Manuscript in prep.*

I

An in vivo high-resolution human brain atlas of synaptic density

Authors:

Annette Johansen[1,2,*], Vincent Beliveau[1,3,*], Emil Colliander[1,2], Nakul Ravi Raval[1,4,5], Vibeke Høyrup Dam[1], Nic Gillings[6], Susana Aznar[7], Claus Svarer[1], Pontus Plavén-Sigray[1,8], Gitte Moos Knudsen[1,2]

Affiliations:

1. Neurobiology Research Unit, Copenhagen University Hospital Rigshospitalet, 2100 Copenhagen, Denmark
2. Department of Clinical Medicine, Faculty of Health and Medical Sciences, University of Copenhagen, 2200 Copenhagen, Denmark
3. Department of Neurology, Medical University of Innsbruck, 6020 Innsbruck, Austria
4. Department of Radiology and Biomedical Imaging, Yale University, New Haven, CT 06520, USA
5. Yale PET Center, Yale University, New Haven, CT 06520, USA
6. Department of Clinical Physiology and Nuclear Medicine, Copenhagen University Hospital Rigshospitalet, 2100 Copenhagen, Denmark
7. Center for Neuroscience and Stereology, Copenhagen University Hospital, Bispebjerg-Frederiksberg Hospital, 2400 Copenhagen, Denmark
8. Centre for Psychiatry Research, Department of Clinical Neuroscience, Karolinska Institutet & Stockholm Health Care Services, Region Stockholm, Karolinska University Hospital, SE-171 76, 171 77 Stockholm, SWE

Corresponding author:
Gitte Moos Knudsen
Neurobiology Research Unit,
Copenhagen University Hospital Rigshospitalet,
Blegdamsvej 9
DK-2100 Copenhagen, Denmark
gmk@nru.dk
+45 35 45 67 20

*Authors contributed equally

Abstract

Synapses are fundamental to the function of the central nervous system and are implicated in a number of brain disorders. Despite their pivotal role, a comprehensive imaging resource detailing the distribution of synapses in the human brain has been lacking until now. Here, we employ high-resolution PET neuroimaging in healthy humans to create a 3D atlas of the synaptic marker Synaptic Vesicle glycoprotein 2A (SV2A). Calibration to absolute density values (pmol/mL) was achieved by leveraging postmortem human brain autoradiography data. The atlas unveils distinctive cortical and subcortical gradients of synapse density that reflect functional topography and hierarchical order from core sensory to higher-order integrative areas - a distribution that diverges from SV2A mRNA patterns. Furthermore, we find a positive association between IQ and SV2A density in several higher-order cortical areas. This new resource will help advance our understanding of brain physiology and the pathogenesis of brain disorders, serving as a pivotal tool for future neuroscience research.

Significance statement

Here, we present a high-resolution 3D *in vivo* brain atlas of synaptic density in the human brain. In the healthy human brain, distinctive cortical and subcortical gradients of synapse density reflect functional topography and hierarchical order from core sensory to higher-order integrative areas - a distribution that diverges from SV2A mRNA patterns. This brain atlas will help advance our understanding of human brain physiology and the pathogenesis of brain disorders, serving as a pivotal tool for future research in clinical, translational and comparative neuroscience .

Introduction

Synapses are the junctions between neurons and constitute a central site for neuronal signaling in the brain. Estimates of the number of synapses formed on a single neuron in the adult human brain vary greatly (7,200 – 80,000), bringing their total number to a staggering range of 6 x 10^{14} to 7 x 10^{15} [1]. Because of their pivotal role in brain functions, the study of synapses is key to improving our understanding of how modulation of synapses affects brain function and human behavior from motor control to higher-order cognitive functions in both health and disease.

Synaptic structures and their organization in the human brain can be studied *in vitro* with electron microscopy to visualize distinct components of individual synapses on a sub-cellular scale, with *in situ* hybridization for mRNA quantification, and with immunohistochemistry for visualizing specific synaptic proteins [2]. Commonly used human brain atlases that provide estimates of gene expression (e.g., mRNA quantification) have been shown to misrepresent the corresponding protein levels and distribution [3–5]. Autoradiography provides absolute target protein concentrations in postmortem brain tissue with high in-plane resolution, but the spatial information is often limited by a low number of discrete samples in a few subjects, and regions with microanatomical and functional heterogeneity are often represented by single estimates. To the best of our knowledge, no detailed human brain atlas that maps the synaptic density currently exists.

Using appropriate radioligands and large number of subjects, *in vivo* molecular neuroimaging with positron emission tomography (PET) can provide 3D human brain atlases at high resolution [3, 4, 6]. These PET-based brain atlases are instrumental in cross-modal analyses, revealing associations between spatial protein distributions and patterns of e.g., cortical thickness and abnormalities in psychiatric and neurological disorders.

[^{11}C]UCB-J is a PET radioligand that binds to the Synaptic Vesicle glycoprotein 2A (SV2A), a transmembrane protein located in synaptic vesicles in the presynaptic axon terminals [7, 8]. SV2A is ubiquitously expressed in all grey matter regions of the brain and across neurotransmitter systems [9]. SV2A co-localizes with synaptophysin immunostaining and is

regarded as a proxy of synaptic density [8], allowing for investigations of how synaptic density relates to brain functions. For example, studies have shown that impaired cognition correlates negatively with PET measures of SV2A binding in Alzheimer's disease and schizophrenia [10–12]. A related question is to what extent synaptic density is functionally related to cognitive function in healthy individuals.

We here present a high-resolution *in vivo* human brain atlas of the synaptic marker SV2A. By obtaining quantitative measures from postmortem human brain autoradiography, we convert PET binding estimates to represent SV2A in absolute density (pmol/mL brain tissue). The atlas represents synaptic density across the cerebral cortex and subcortical brain structures, and enables us to characterize the spatial distribution of SV2A protein density and the relation to SV2A mRNA. Finally, we examine the relationship between synaptic density and demographic variables, brain morphology, and cognitive function.

Methods

i.   *Participants*

Thirty-three healthy participants who had undergone [11C]UCB-J PET and structural MRI examinations were included in the study. Demographic information, intelligence quotient (IQ) scores, and scan-related details are provided in Table 1. All participants were scanned under study protocols approved by the Ethics Committee of the Capital Region of Denmark (protocol ids: H-18038352, H-19053510, H-16026898, H-KF-2006-20) and data were entered into the CIMBI database [13].

All participants provided written informed consent before undergoing a comprehensive screening procedure involving medical history, blood biochemistry assessments, and neurological and psychiatric evaluations. PET and MRI data from 12 participants have been reported in a previous publication [14].

IQ was assessed with the Reynolds Intellectual Screening Test (RIST) [15] consisting of a verbal task (Guess What) capturing crystallized intelligence and a nonverbal task (Odd-Item Out) capturing fluid intelligence. Raw scores on the two tasks were combined and transformed into a total RIST index score reflecting overall IQ. Testing took place in standardized test room and was performed by trained neuropsychological testers.

Table 1: Demographics of the PET cohort (N = 33).	
Sex (n, F/M)	17/16
Age (years)	24.0 [20, 44]
IQ[a]	108 [96, 125]
Injected dose (MBq)	410 [224, 550]
Injected dose, adjusted (MBq/kg)	5.5 [2.7, 9.7]
Injected mass, adjusted (ng/kg)	6.5 [1.2, 80.9]

Table 1. Description of the sample used for the [^{11}C]UCB-J PET measurements. Values are median [range]. [a] IQ scores were available for 30 participants.

ii.   PET and MRI acquisition

The detailed methodology for [^{11}C]UCB-J PET, T1- and T2-weighted MRI scan acquisitions, as well as blood analyses, can be found in a previous publication [14]. Briefly, participants underwent 120 min [^{11}C]UCB-J PET scans with the High-Resolution Research Tomograph (HRRT, CTI/Siemens, Knoxville, TN, USA) starting at the time of radiotracer bolus injection. Data were acquired in 3D list mode and reconstructed into 40 frames (8 x 15 s, 8 x 30 s, 4 x 60 s, 5 x 120 s, 10 x 300 s, 5 x 300 s) using a 3D OP-OSEM algorithm (16 subsets, 10 iterations) with attenuation correction using the HRRT maximum a posteriori transmission reconstruction method (MAP-TR) μ-map [16, 17]. The reconstructed PET images comprised 207 planes of 256 x 256 voxels of 1.22 x 1.22 x 1.22 mm^3. Continuous automatic arterial blood sampling was conducted for the first 15 minutes, followed by manual samples taken at specific time intervals (2.5, 5, 10, 25, 40, 60, 90, and 120 min). These samples were then used to determine metabolite-corrected arterial plasma input functions.

MRI scans were conducted using a Siemens Magnetom Prisma 3T scanner (Siemens AG, Erlangen, Germany) using a Siemens 32-channel head coil. Participants underwent scanning with

either of two similar T1 MP-RAGE sequences (TR = 2000/1810 ms, TE = 2.58 ms, TI = 972 ms, flip angle = 8°/9°, in-plane resolution = 0.9 x 0.9 mm^2/ 0.8 x 0.8 mm^2, slice thickness = 0.9 mm/0.8 mm, number of slices = 224, no gap, in-plane matrix = 288 x 288/256 x 256, field-of-view: 230 mm) and a T2-weighted space turbo spin echo sequence (TR = 3200 ms, TE = 408 ms, in-plane resolution = 0.9 x 0.9 mm^2, slice thickness = 0.9 mm, number of slices = 224, no gap, in-plane matrix = 256 x 256). T1- and T2-weighted images were corrected for gradient non-linearities online on the scanner.

iii. *Image processing*

The reconstructed dynamic PET data were motion-corrected using the frame-by-frame reconcile procedure in AIR (v. 5.2.5, LONI, UCLA, CA, USA http://air.bmap.ucla.edu/AIR5). Subsequent preprocessing of PET and MR images was performed using the PETSurfer pipeline [18] in FreeSurfer [19] (v. 7.2, https://surfer.nmr.mgh.harvard.edu/) as described in detail elsewhere [3]. The T1-weighted images underwent standard anatomical processing using the recon-all stream within FreeSurfer. PET images were co-registered to the MR images using a rigid transformation, and subsequently resampled onto the standard surface (*fsaverage*) and volume (*MNI152*) spaces and smoothed with 10 and 5 mm full-width at half-maximum, respectively. Regional time-activity curves for the regions of the Desikan-Killiany cortical atlas [20] and eight subcortical regions defined by FreeSurfer (i.e., accumbens, amygdala, caudate, cerebellum cortex, hippocampus, putamen, thalamus, and ventral diencephalon) were extracted from the non-smoothed data.

iv. *Kinetic modeling*

Kinetic modeling of [^{11}C]UCB-J PET data was performed in R (v. 4.2.1, R Foundation, Vienna, Austria) using the *kinfitr* package v. 0.7.2 [21]. The metabolite-corrected arterial input function (AIF) was estimated for each participant by first fitting a cubic spline to the first four samples of the whole blood-to-plasma ratio data point. Interpolated values were then multiplied with the

continuous whole-blood curve, and subsequently concatenated with the manual plasma samples. The unmetabolized [11C]UCB-J in plasma (parent fraction) obtained from the radio-HPLC analysis was fitted using a Hill model, which was subsequently multiplied to the plasma radioactivity curve to obtain the metabolite-corrected AIF.

Total tissue distribution volumes (V_T; mL/cm^3) of all brain regions, as well as for the cortical vertices and subcortical voxels, were estimated with the one-tissue compartment model (1TCM) using the participants' metabolite-corrected arterial input function, as previously described [14].

v. *In vivo SV2A binding and in vitro autoradiography*

To obtain regional estimates of cerebral SV2A protein densities (B_{max}; pmol/mL), we made use of frozen sections of post-mortem human brain tissue from seven donors from the Bispebjerg Brain Bank (Bispebjerg-Frederiksberg Hospital, Copenhagen University Hospital, Denmark), approved by the Ethics Committee of the Capital Region of Denmark (protocol id: H-20062005). Demographic information on the donors is provided in Table S1. The sections included frontal, parietal, temporal, and occipital cortex as well as white matter. We employed [3H]UCB-J autoradiography to determine SV2A B_{max} following procedures outlined in the supplementary material. These data were converted from the unit pmol/g to pmol/mL using a grey matter density of 1.045 g/mL [22]. To supplement the data with subcortical regions, we included SV2A estimates from [11C]UCB-J autoradiography conducted by Varnäs et al. [23]. These data were reported in the unit of kBq/mm^2. To align the estimates with our [3H]UCB-J data, we performed a linear regression with a null intercept to obtain estimates in units of pmol/mL.

Next, weighted-averages of the [11C]UCB-J V_T estimates corresponding to the autoradiography regions were obtained, and the association with the calibrated autoradiography data was assessed using linear regression. The resulting linear equation was then used to transform [11C]UCB-J V_T values for all regions, voxels and vertices into absolute protein

densities (pmol/mL). All subsequent references to SV2A densities thus pertain to $[^{11}C]$UCB-J V_T values calibrated to pmol/mL using this approach.

vi. *In vivo SV2A protein density and SV2A gene expression*

As a measure of gene expression, regional SV2A mRNA data were obtained from six donors using the *abagen* toolbox (v 0.1.3) [24]. This software provides a standardized pipeline for the quantification of mRNA data from the Allen Human Brain atlas [25]. A detailed description of the pipeline, including donor demographics, is provided in the Supplementary Material.

vii. *Statistics*

For each region, a linear regression model was used to assess the association between age, sex, and IQ and SV2A densities. We further assess the effect of cortical thickness and subcortical volume on SV2A densities, adjusting for age and sex (and intracranial volume for voxel-based analyses). All tests were corrected for multiple comparisons using the false discovery rate method [26]. Regional SV2A mRNA levels and SV2A densities were compared using Spearman correlation.

Additional exploratory analyses were performed at the vertex- and voxel-level to investigate subregional associations between *in vivo* SV2A density and IQ generalized linear model adjusted for age and sex. Model significance was assessed with permutation testing using FreeSurfer's *fspalm* script, which invokes FSL's palm (alpha111) [27]. Cluster-forming threshold was set to $p = 0.001$, cluster-wise p-value to 0.05, and 5,000 permutations were performed. Bonferroni correction for 3 spaces, accounting for both cortical hemispheres and the subcortical space, was applied.

Results

i.   In vitro autoradiography and in vivo SV2A imaging

We measured the absolute protein density of SV2A using [^{3}H]UCB-J autoradiography in post-mortem brains from the Bispebjerg Brain Bank. We found high SV2A binding in the neocortical grey matter (range 368-629 pmol/g) and low levels in the white matter (27-36 pmol/g). We included additional brain regions from a previously published [^{11}C]UCB-J autoradiography dataset from Varnäs et al. [23], and converted these to pmol/g based on the linear regression equation (Figure S2; conversion factor = 0.71 pmol/g per kBq/mm^2). Finally, all estimates were converted to volume densities (mL^{-1}).

In vivo SV2A density was measured with [^{11}C]UCB-J PET and compared with the densities obtained with autoradiography. The regional average [^{11}C]UCB-J V_T estimates correlated well with the postmortem autoradiography data (Figure 1; $r(11) = 0.85$, $p = 0.0002$) and were described by the following equation: $V_T = 3.56$ mL/cm^3 + 0.03 mL/cm^3/pmol/mL. Here, the intercept estimate [SE] of 3.56 [2.18] mL/cm^3 represents the average non-displaceable compartment of [^{11}C]UCB-J binding (V_{ND}), while the slope estimate [SE] of 0.03 [0.005] is equal to the average [^{11}C]UCB-J plasma free fraction (f_P) divided by the [^{11}C]UCB-J dissociation constant (f_P/K_D).
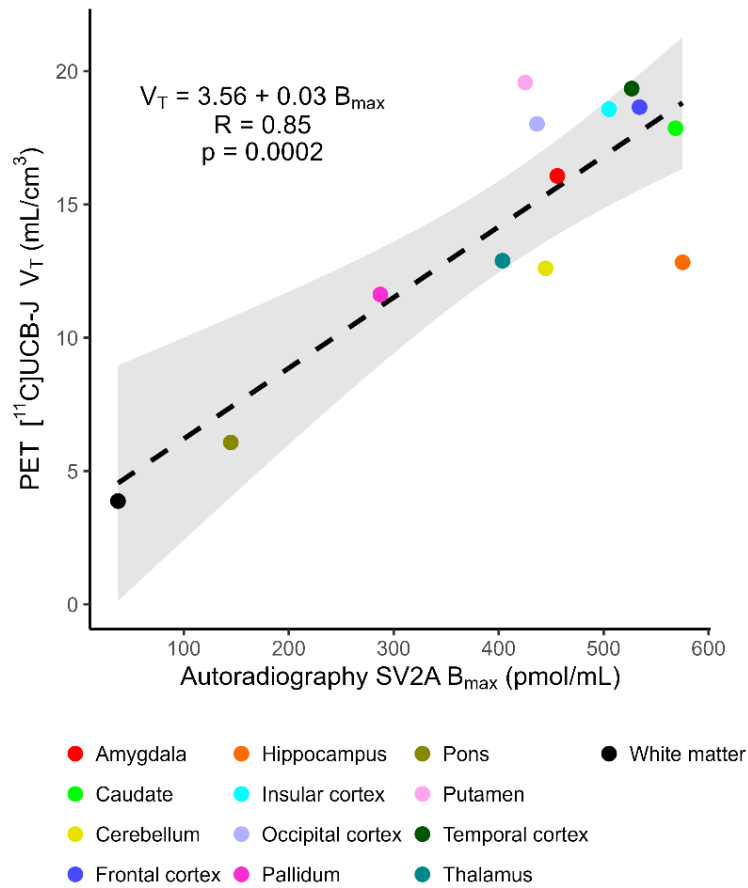
Figure 1. Average regional SV2A densities measured with [^{11}C]UCB-J PET (V_T; mL/cm^3) and autoradiography (B_{max}; pmol/mL) in brains from healthy participants/donors. The dashed line represents the regression line, and shaded grey area the 95% CI.

ii.   The in vivo synaptic density atlas

The linear regression equation from Figure 1 was used to calibrate the V_T values and thereby create the cortical and subcortical SV2A density maps (Figure 2). The atlas shows high SV2A density in the neocortex, with highest densities in the posterior cingulate, precuneus, and gyri of the temporal cortex, and lowest in the pre- and postcentral gyri. For the subcortical regions, we observe the highest density in the putamen and caudate and lower density in the hippocampus, thalamus, pallidum, and cerebellum. Regional SV2A densities are reported in Supplementary Table S2.

We also created maps visualizing the variability of SV2A density (Figures S3 and S4): Relative to the mean value, we observe the highest cortical variability bilaterally in the peri-

colossal rim of the cingulate cortex, around the temporal poles and inferior temporal gyri, medial post-central gyrus, and part of the left lateral occipital cortex. In contrast, the precuneus bilaterally, and frontal and temporal areas of the right hemisphere show the lowest variability. By visual inspection, the variability appears higher in the left hemisphere.
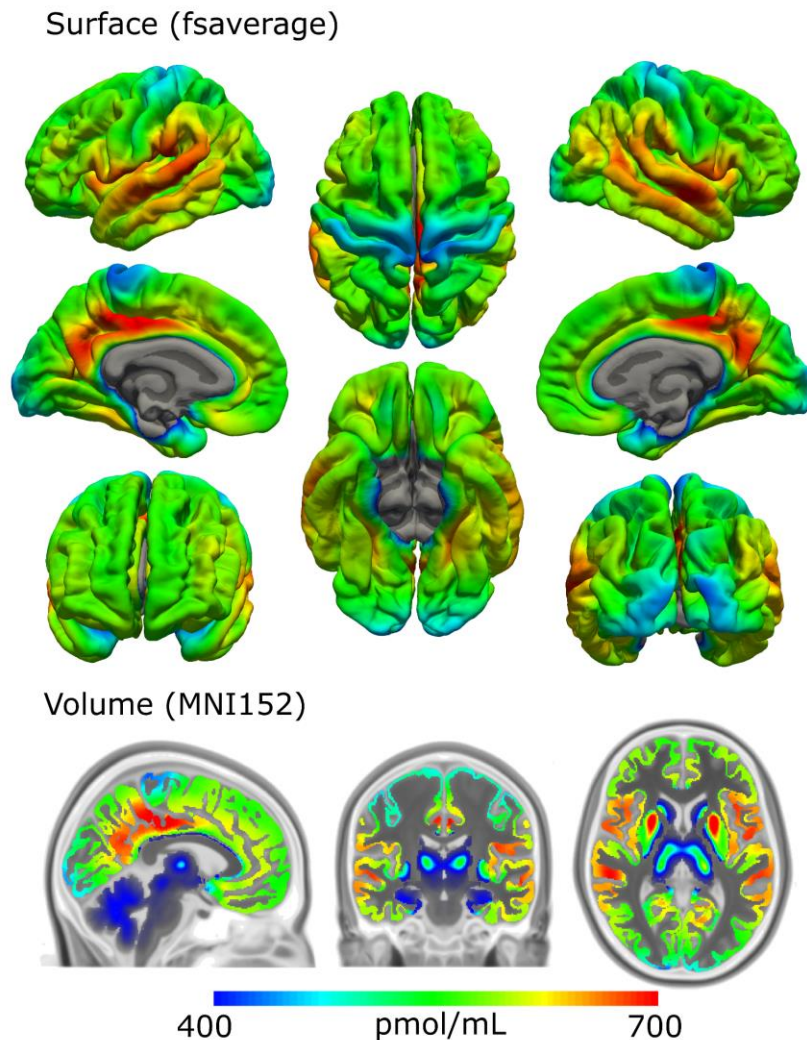
Figure 2. Average SV2A density maps (B_{max}; pmol/mL) on the FreeSurfer fsaverage surface (top) and in the MNI152 volume space (bottom).

iii.   In vivo SV2A density and SV2A gene expression

We examined how well regional *in vivo* SV2A density corresponded with SV2A gene expression as assessed by SV2A mRNA data from the Allen Human Brain Atlas [25]. We found no

association between regional *in vivo* SV2A density and SV2A mRNA levels (Figure 3; Spearman's $r(39) = 0.10$, $p = 0.53$).
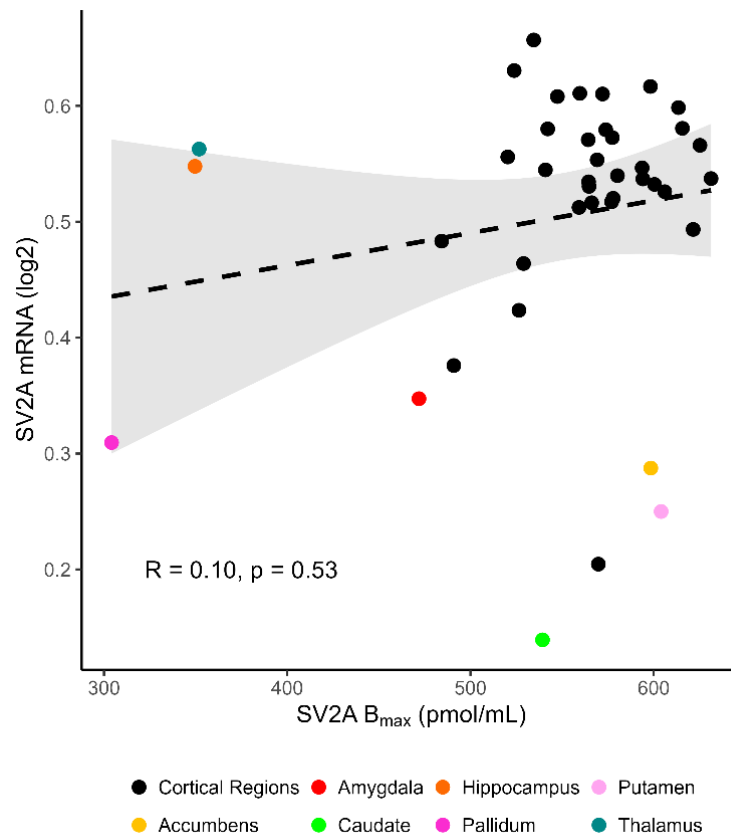
Figure 3. Average regional SV2A density plotted against corresponding SV2A mRNA values (log2). The dashed line and shaded grey area represent the regression line and 95% CI for all brain regions. SV2A density and mRNA levels were not correlated, as evaluated with Spearman's correlation.

iv.   Effects of demographic variables on SV2A density

Across all brain regions, we found no effects of age, sex on SV2A densities nor association with IQ scores when correcting for multiple comparisons (all corrected *p*-values > 0.13). Similarly, there were no associations between cortical thickness, subcortical volumes, and regional SV2A densities (all corrected *p*-values > 0.69). All model outputs are listed in Supplementary Table S4 and S5.

Our vertex- and voxel-wise analysis showed positive associations between IQ scores and SV2A density in several symmetrical vertex clusters found in the parahippocampal gyri,

orbitofrontal and temporal cortices (Figure 4 and Table S3). No subcortical voxels were below the set threshold.
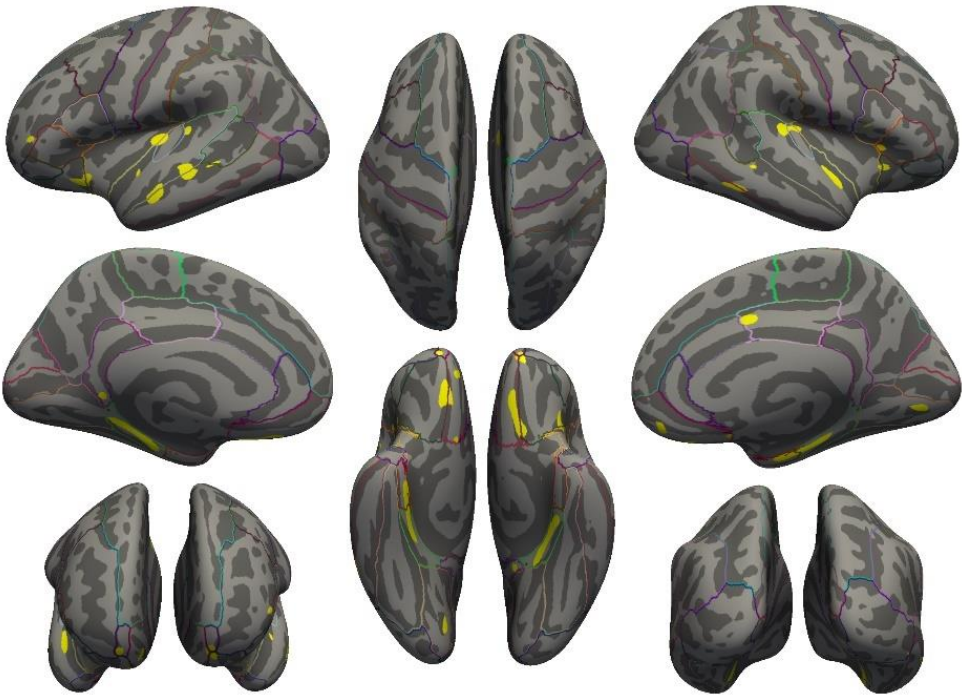
Figure 4. Inflated surface maps with projections of vertices that show positive association between SV2A density and IQ scores (N = 30). For region annotations, cluster sizes and exact *p*-values, see Table S3. The colored lines show the borders of the regions defined by the Desikan-Killiany atlas.

Discussion

Here, we present the first high-resolution *in vivo* human brain atlas of absolute SV2A density as a proxy for synaptic density. We combined *in vivo* and *in vitro* molecular imaging data of SV2A to create a brain map using an optimized surface- and volume-based approach. The atlas provides the spatial distribution and patterns of synaptic density in the human neocortex and subcortical brain structures and is freely available for easy comparison with other maps in *fsaverage* space, while the subcortical structures are available in the commonly used *MNI152* template.

Whereas the regional PET estimates of SV2A binding generally correlated very well with postmortem autoradiography measurements of SV2A density, some regions, and particularly the hippocampus, exhibited notable differences between the autoradiography and PET data. In our data and in previous SV2A PET studies [28–30], the hippocampus consistently ranks as a low-binding region whereas in the Varnäs et al. autoradiography data, the hippocampus is reported to have the highest SV2A density. Although partial volume effects leading to underestimation of PET measurements could potentially contribute to this finding, it seems unlikely that such effects would differentially influence the hippocampus estimates in this young and healthy cohort. An important consideration is that each PET measure represents the average of each region, whereas autoradiography was performed on two discrete brain sections not covering entire regions. Given the diverse cytoarchitecture and neuroreceptor composition of the different hippocampal subfields [31], the autoradiography samples may not fully capture the heterogeneity present in this brain region.

Conversely, most SV2A PET studies find the putamen to have the highest binding [8, 29], but this region only exhibited intermediate density in the autoradiography data. Interestingly, our atlas reveals a clear rostral-caudal gradient in the putamen. Functionally, the rostral part of the putamen, where we observe the highest binding, receives input from associative cortex in the frontal, parietal, and temporal lobes [32, 33] and contains almost twice as many interneurons as the caudal part [34]. The Varnäs autoradiography study sampled the caudal parts of the putamen, which receive projections from the sensorimotor cortex where we observe lower *in vivo* binding.

Such a gradient could indicate that the striatal networks involved in motor function are less complex, or require less modulation compared to the more rostral networks involved in higher-order cognitive functions.

In the neocortex, we observe the highest SV2A density in the posterior cingulate cortex, precuneus cortex, insular cortex, and temporal cortex. In contrast, we observe the lowest density in the lateral occipital cortices and the sensorimotor cortices, which include central parts of the primary visual cortex and the primary motor and sensory cortices. This pattern of higher density in regions related to associative functions and lower density in core sensory and motor areas aligns with patterns of many neurotransmitter receptors [3, 35]. Additionally, we observe a gradient within the sensorimotor cortex reflecting the somatotopic homunculus [36, 37]. We find the lowest SV2A density in areas representing larger body structures, such as the trunk and legs, gradually increasing laterally to regions representing fine motor skills and higher sensory resolution, such as the hands, face, and mouth. Mid-laterally in the central sulcus, between these two bands of lower SV2A density, we see a small island with slightly higher binding, which seems to overlap topographically with the newly discovered *Rolandic motor association area*[38]. In the occipital cortex, we likewise observe a gradient in SV2A density going from lower density in the occipital pole (central vision) to higher density in an anterior direction along the calcarine sulcus (peripheral vision).

These spatial differences could imply that basic sensory and motor functions rely on simpler cortical networks, whereas higher-order integrative, cognitive, and emotional functions require more complex cortical networks with higher synaptic density. This distinction is also present for several neurotransmitter systems in the human and the macaque cortex [31, 39, 40]. This cortical gradient is further mirrored in a study by Wei et al. [41], demonstrating that higher-order cognitive networks (e.g., the default mode network) show higher expression of the so-called *human-accelerated region* (HAR) genes compared to the somato-motor and visual networks, and that HAR genes are associated with, e.g., human intellectual ability. Whether higher synaptic density in these or other regions is associated with better cognitive ability in healthy individuals, as has been demonstrated for patients with neurodegenerative disorders [42],

is unclear. Interestingly, our exploratory vertex-based analysis showed positive associations between IQ scores and SV2A density in areas such as the parahippocampal gyrus, entorhinal cortex, and orbitofrontal and temporal cortices. Although this association warrants replication in a larger sample, characteristics of several of these regions have previously been linked to intelligence, by, e.g., a shared genetic origin with grey matter density in the parahippocampal gyrus [43], positive associations with cortical thickness, dendritic length and complexity, and speed of action potentials in the temporal cortex [44]. In contrast, another study found no associations between IQ and absolute number of neurons, cortical thickness, or cortical surface area in the global neocortex [45]. Together, this underscores the neurobiological complexity underlying cognitive abilities and how SV2A neuroimaging may prove a valuable tool for disentangling these associations.

We found no spatial correlation between *in vivo* SV2A density and SV2A mRNA from the Allen Human Brain atlas. The absence of a correlation between SV2A gene expression (mRNA) and SV2A protein density is in agreement with SV2A being a presynaptic protein, as also seen for, e.g., the serotonin transporter and several neurotransmitter receptors [3, 5]. This discrepancy is explained by several factors, such as the proportion of projection neurons versus interneurons, stability of the mRNA, SV2A protein turnover, and capacity for local protein synthesis in the axon terminal [46]. In addition to being protein-based, the atlas presented here has the advantage that SV2A is expressed as absolute protein density (pmol/mL), thus making it directly comparable to other microanatomical structures such as the density of neurons and neuroreceptors. Further, we used surface-based processing which greatly reduces artefacts due to partial volume effects [18]. This is especially evident when comparing to a volume-based population-average map of [^{11}C]UCB-J non-displaceable binding potential (BP_{ND}) [47]. The BP_{ND} map shows cortical striping patterns and a significant correlation with cortical curvature indicative of partial-volume effects which was not the case for our SV2A density map (Figure S5).

This work is not without limitations. One aspect is the estimated parameters of the linear equation used to transform our PET measurements into absolute protein densities. For example,

if we choose the most extreme values within the 95% confidence interval to provide the slope and intercept, the estimate of SV2A density for a cortical region with [11C]UCB-J V_T value of ~18 mL/cm^3 would change by $\pm$ 9%, whereas a lower binding region like the pallidum with a V_T of ~12 mL/cm^3 would change within the range of -30% to +7%.

Another consideration is that the postmortem brain tissue came from donors who were older than the healthy individuals in our PET cohort. We do not find any age effect on SV2A density but we cannot exclude that this is because of the relatively narrow age range. Other PET studies with broader age ranges have reported no age effects [48, 49], while some preliminary data suggest there may be a reduction with age [50]. Different analysis approaches (e.g., [11C]UCB-J quantification method, application of partial volume correction, and whether correction for multiple comparisons was taken into account), could explain the divergent results [51, 52]. Furthermore, potential age effects may not follow a linear trajectory but could for example reflect the effects of synapse formation and pruning in late adolescence and young adulthood and a reduction after a certain age. As such, effects of age may best be explored with models informed by prior knowledge on brain development.

The participants from the autoradiography and the PET studies were not perfectly balanced in terms of sex, but in line with other SV2A PET studies [48, 49, 53], we do not find any effect of sex on cerebral SV2A densities.

Because the present cohort had relatively high IQ scores and limited variability, the participants in this study are not fully representative of the general population. It is possible that inclusion of participants with a larger range of IQ could have strengthened our finding of a positive association between IQ and SV2A, but this remains to be seen in future studies.

Finally, it is important to consider the limitations of using SV2A as a proxy for synaptic density. SV2A is a highly preserved synaptic protein alike synaptophysin which is one of the most commonly used synaptic density markers [54], and measurements of the two proteins correlate very well [8, 55]. SV2A is located in the synaptic vesicle membrane with most vesicles estimated to contain five molecules per vesicle [56]. Consequently, both PET and autoradiography imaging can theoretically be affected by variability in the number of vesicles

per synapse or the number of proteins in each vesicle. These potential sources of variability are important to keep in mind as their contribution to different pathological conditions could vary.

Conclusion

Here, we present a detailed PET- and MRI-based high-resolution *in vivo* brain atlas of absolute synaptic density in the healthy human brain. By combining two radioligand neuroimaging techniques, we calibrate our *in vivo* PET measurements of SV2A to represent absolute protein densities. The atlas highlights distinctive cortical and subcortical gradients of synapse density that reflect functional topography and mirrors hierarchical patterns seen for cortical thickness and functional networks. Furthermore, our data indicates a potential link between general intelligence and synaptic density in several brain regions that deserved further exploration in future studies. This new resource will help advance our understanding of brain physiology and the pathogenesis of brain disorders, serving as a pivotal tool for future neuroscience research.

Data and availability

The atlas will be freely available and can be accessed from the site: https://xtra.nru.dk/SV2A-atlas. Researchers may apply for access to the original data by submitting an application to the CIMBI Database (https://cimbi.dk) [13]. Code is available upon reasonable request.

Funding

Conflict of Interest

Acknowledgements

References

1. Silbereis JC, Pochareddy S, Zhu Y, Li M, Sestan N. The Cellular and Molecular Landscapes of the Developing Human Central Nervous System. Neuron. 2016;89:248–268.

2. Serrano ME, Kim E, Petrinovic MM, Turkheimer F, Cash D. Imaging Synaptic Density: The Next Holy Grail of Neuroscience? Front Neurosci-Switz. 2022;16:796129.

3. Beliveau V, Ganz M, Feng L, Ozenne B, Højgaard L, Fisher PM, et al. A High-Resolution In Vivo Atlas of the Human Brain's Serotonin System. J Neurosci. 2017;37:120–128.

4. Nørgaard M, Beliveau V, Ganz M, Svarer C, Pinborg LH, Keller SH, et al. A high-resolution in vivo atlas of the human brain's benzodiazepine binding site of GABAA receptors. Neuroimage. 2021;232:117878.

5. Hansen JY, Markello RD, Tuominen L, Nørgaard M, Kuzmin E, Palomero-Gallagher N, et al. Correspondence between gene expression and neurotransmitter receptor and transporter density in the human brain. NeuroImage. 2022;264:119671.

6. Hansen JY, Shafiei G, Markello RD, Smart K, Cox SML, Nørgaard M, et al. Mapping neurotransmitter systems to the structural and functional organization of the human neocortex. Nat Neurosci. 2022;25:1569–1581.

7. Nabulsi NB, Mercier J, Holden D, Carré S, Najafzadeh S, Vandergeten M-C, et al. Synthesis and Preclinical Evaluation of 11C-UCB-J as a PET Tracer for Imaging the Synaptic Vesicle Glycoprotein 2A in the Brain. J Nucl Med. 2016;57:777–784.

8. Finnema SJ, Nabulsi NB, Eid T, Detyniecki K, Lin S, Chen M-K, et al. Imaging synaptic density in the living human brain. Sci Transl Med. 2016;8:348ra96.

9. Bajjalieh S, Frantz G, Weimann J, McConnell S, Scheller R. Differential expression of synaptic vesicle protein 2 (SV2) isoforms. J Neurosci. 1994;14:5223–5235.

10. Mecca AP, Chen M, O'Dell RS, Naganawa M, Toyonaga T, Godek TA, et al. In vivo measurement of widespread synaptic loss in Alzheimer's disease with SV2A PET. Alzheimer's Dementia. 2020;16:974–982.

11. Radhakrishnan R, Skosnik PD, Ranganathan M, Naganawa M, Toyonaga T, Finnema S, et al. In vivo evidence of lower synaptic vesicle density in schizophrenia. Mol Psychiatr. 2021;26:7690–7698.

12. Zhang J, Wang J, Xu X, You Z, Huang Q, Huang Y, et al. In vivo synaptic density loss correlates with impaired functional and related structural connectivity in Alzheimer's disease. J Cereb Blood Flow Metab. 2023;43:977–988.

13. Knudsen GM, Jensen PS, Erritzoe D, Baaré WFC, Ettrup A, Fisher PM, et al. The Center for Integrated Molecular Brain Imaging (Cimbi) database. NeuroImage. 2016;124:1213–1219.

14. Johansen A, Armand S, Plavén-Sigray P, Nasser A, Ozenne B, Petersen I, et al. Escitalopram increases synaptic density in the human brain over weeks: A randomized controlled trial. PREPRINT (Version 1) Available at Research Square. 2023. 2023. https://doi.org/10.21203/rs.3.rs-2989150/v1.

15. Reynolds CR, Kamphaus RW. Introduction to the Reynolds Intellectual Assessment Scales and the Reynolds Intellectual Screening Test. Contemporary Intellectual Assessment: Theories, Tests, and Issues., New York, NY, US: The Guilford Press; 2005. p. 461–483.

16. Keller SH, Svarer C, Sibomana M. Attenuation Correction for the HRRT PET-Scanner Using Transmission Scatter Correction and Total Variation Regularization. IEEE T Med Imaging. 2013;32:1611–1621.

17. Sureau FC, Reader AJ, Comtat C, Leroy C, Ribeiro M-J, Buvat I, et al. Impact of Image-Space Resolution Modeling for Studies with the High-Resolution Research Tomograph. J Nucl Med. 2008;49:1000–1008.

18. Greve DN, Svarer C, Fisher PM, Feng L, Hansen AE, Baare W, et al. Cortical surface-based analysis reduces bias and variance in kinetic modeling of brain PET data. Neuroimage. 2014;92:225–236.

19. Fischl B. FreeSurfer. Neuroimage. 2012;62:774–781.

20. Desikan RS, Ségonne F, Fischl B, Quinn BT, Dickerson BC, Blacker D, et al. An automated labeling system for subdividing the human cerebral cortex on MRI scans into gyral based regions of interest. Neuroimage. 2006;31:968–980.

21. Tjerkaski J, Cervenka S, Farde L, Matheson GJ. Kinfitr — an open-source tool for reproducible PET modelling: validation and evaluation of test-retest reliability. EJNMMI Res. 2020;10:77.

22. DiResta GR, Lee J, Arbit E. Measurement of brain tissue specific gravity using pycnometry. J Neurosci Meth. 1991;39:245–251.

23. Varnäs K, Stepanov V, Halldin C. Autoradiographic mapping of synaptic vesicle glycoprotein 2A in non-human primate and human brain. Synapse. 2020;74:e22157.

24. Markello RD, Arnatkeviciute A, Poline J-B, Fulcher BD, Fornito A, Misic B. Standardizing workflows in imaging transcriptomics with the abagen toolbox. Elife. 2021;10.

25. Hawrylycz MJ, Lein ES, Guillozet-Bongaarts AL, Shen EH, Ng L, Miller JA, et al. An anatomically comprehensive atlas of the adult human brain transcriptome. Nature. 2012;489:391–399.

26. Benjamini Y, Hochberg Y. Controlling the False Discovery Rate: A Practical and Powerful Approach to Multiple Testing. J Royal Statistical Soc Ser B Methodol. 1995;57:289–300.

27. Winkler AM, Ridgway GR, Webster MA, Smith SM, Nichols TE. Permutation inference for the general linear model. NeuroImage. 2014;92:381–397.

28. Finnema SJ, Nabulsi NB, Mercier J, Lin S, Chen M-K, Matuskey D, et al. Kinetic evaluation and test–retest reproducibility of [11C]UCB-J, a novel radioligand for positron emission tomography imaging of synaptic vesicle glycoprotein 2A in humans. J Cereb Blood Flow Metabolism. 2017;38:2041–2052.

29. Naganawa M, Li S, Nabulsi N, Henry S, Zheng M-Q, Pracitto R, et al. First-in-Human Evaluation of 18F-SynVesT-1, a Radioligand for PET Imaging of Synaptic Vesicle Glycoprotein 2A. J Nucl Med. 2021;62:561–567.

30. Lu Y, Toyonaga T, Naganawa M, Gallezot J-D, Chen M-K, Mecca AP, et al. Partial volume correction analysis for 11C-UCB-J PET studies of Alzheimer's disease. Neuroimage. 2021;238:118248.

31. Palomero-Gallagher N, Kedo O, Mohlberg H, Zilles K, Amunts K. Multimodal mapping and analysis of the cyto- and receptorarchitecture of the human hippocampus. Brain Struct Funct. 2020;225:881–907.

32. Parent A, Hazrati L-N. Functional anatomy of the basal ganglia. I. The cortico-basal ganglia-thalamo-cortical loop. Brain Res Rev. 1995;20:91–127.

33. Draganski B, Kherif F, Klöppel S, Cook PA, Alexander DC, Parker GJM, et al. Evidence for Segregated and Integrative Connectivity Patterns in the Human Basal Ganglia. J Neurosci. 2008;28:7143–7152.

34. Lecumberri A, Lopez-Janeiro A, Corral-Domenge C, Bernacer J. Neuronal density and proportion of interneurons in the associative, sensorimotor and limbic human striatum. Brain Struct Funct. 2018;223:1615–1625.

35. Zilles K, Palomero-Gallagher N. Multiple Transmitter Receptors in Regions and Layers of the Human Cerebral Cortex. Front Neuroanat. 2017;11:78.

36. Penfield W, Boldrey E. Somatic motor and sensory representation in the cerebral cortex of man as studied by electrical stimulation. Brain. 1937;60:389–443.

37. Gordon EM, Chauvin RJ, Van AN, Rajesh A, Nielsen A, Newbold DJ, et al. A somato-cognitive action network alternates with effector regions in motor cortex. Nature. 2023;617:351–359.

38. Jensen MA, Huang H, Valencia GO, Klassen BT, Boom MA van den, Kaufmann TJ, et al. A motor association area in the depths of the central sulcus. Nat Neurosci. 2023;26:1165–1169.

39. Froudist-Walsh S, Xu T, Niu M, Rapan L, Zhao L, Margulies DS, et al. Gradients of neurotransmitter receptor expression in the macaque cortex. Nat Neurosci. 2023:1–14.

40. Goulas A, Changeux J-P, Wagstyl K, Amunts K, Palomero-Gallagher N, Hilgetag CC. The natural axis of transmitter receptor distribution in the human cerebral cortex. Proc National Acad Sci. 2021;118:e2020574118.

41. Wei Y, Lange SC de, Scholtens LH, Watanabe K, Ardesch DJ, Jansen PR, et al. Genetic mapping and evolutionary analysis of human-expanded cognitive networks. Nat Commun. 2019;10:4839.

42. Mecca AP, O'Dell RS, Sharp ES, Banks ER, Bartlett HH, Zhao W, et al. Synaptic density and cognitive performance in Alzheimer's disease: A PET imaging study with [11C]UCB-J. Alzheimer's Dementia. 2022;18:2527–2536.

43. Pol HEH, Schnack HG, Posthuma D, Mandl RCW, Baaré WF, Oel C van, et al. Genetic Contributions to Human Brain Morphology and Intelligence. J Neurosci. 2006;26:10235–10242.

44. Goriounova NA, Heyer DB, Wilbers R, Verhoog MB, Giugliano M, Verbist C, et al. Large and fast human pyramidal neurons associate with intelligence. ELife. 2018;7:e41714.

45. Songthawornpong N, Teasdale TW, Olesen MV, Pakkenberg B. Is There a Correlation Between the Number of Brain Cells and IQ? Cereb Cortex. 2020;31:650–657.

46. Hafner A-S, Donlin-Asp PG, Leitch B, Herzog E, Schuman EM. Local protein synthesis is a ubiquitous feature of neuronal pre- and postsynaptic compartments. Science. 2019;364.

47. Markello RD, Hansen JY, Liu Z-Q, Bazinet V, Shafiei G, Suárez LE, et al. neuromaps: structural and functional interpretation of brain maps. Nat Methods. 2022;19:1472–1479.

48. Michiels L, Delva A, Aalst J van, Ceccarini J, Vandenberghe W, Vandenbulcke M, et al. Synaptic density in healthy human aging is not influenced by age or sex: a 11C-UCB-J PET study. Neuroimage. 2021;232:117877.

49. Andersen KB, Hansen AK, Knudsen K, Schacht AC, Damholdt MF, Brooks DJ, et al. Healthy brain aging assessed with [18F]FDG and [11C]UCB-J PET. Nucl Med Biol. 2022;112:52–58.

50. Mansur A, Rabiner EA, Comley RA, Lewis Y, Middleton LT, Huiban M, et al. Characterization of 3 PET Tracers for Quantification of Mitochondrial and Synaptic Function in Healthy Human Brain: 18F-BCPP-EF, 11C-SA-4503, and 11C-UCB-J. J Nucl Med. 2020;61:96–103.

51. Greve DN, Salat DH, Bowen SL, Izquierdo-Garcia D, Schultz AP, Catana C, et al. Different partial volume correction methods lead to different conclusions: An 18F-FDG-PET study of aging. Neuroimage. 2016;132:334–343.

52. Nørgaard M, Ganz M, Svarer C, Frokjaer VG, Greve DN, Strother SC, et al. Different preprocessing strategies lead to different conclusions: A [11C]DASB-PET reproducibility study. J Cereb Blood Flow Metabolism. 2019;40:1902–1911.

53. Fang XT, Toyonaga T, Hillmer AT, Matuskey D, Holmes SE, Radhakrishnan R, et al. Identifying brain networks in synaptic density PET (11C-UCB-J) with independent component analysis. Neuroimage. 2021;237:118167.

54. Rossi R, Arjmand S, Bærentzen SL, Gjedde A, Landau AM. Synaptic Vesicle Glycoprotein 2A: Features and Functions. Front Neurosci-Switz. 2022;16:864514.

55. Mikkelsen JD, Kaad S, Aripaka SS, Finsen B. Synaptic vesicle glycoprotein 2A (SV2A) levels in the cerebral cortex in patients with Alzheimer's disease: a radioligand binding study in postmortem brains. Neurobiol Aging. 2023;129:50–57.

56. Mutch SA, Kensel-Hammes P, Gadd JC, Fujimoto BS, Allen RW, Schiro PG, et al. Protein Quantification at the Single Vesicle Level Reveals That a Subset of Synaptic Vesicle Proteins Are Trafficked with High Precision. J Neurosci. 2011;31:1461–1470.

Supplementary material
An in vivo high-resolution human brain atlas of synaptic density

Contents

Supplementary methods

[³H]UCB-J autoradiography

Post-mortem brains from neurologically healthy individuals (N = 7, average postmortem interval of 44.5 hours (range 24-72 hours) were donated to the Bispebjerg Brain Bank (Bispebjerg-Frederiksberg Hospital, Copenhagen University Hospital, Denmark). All donors provided written informed consent, and clinical data were obtained retrospectively from the patient's medical reports. The project was approved by the ethical committee of the Capital Region of Denmark, journal no: H-20062005.

Frozen brain pieces (stored at −80°C) of the frontal cortex, temporal cortex, parietal cortex, and occipital cortex were dissected to ensure areas with both white and gray matter (details explained below). Coronal cryosections (12 μm) of these pieces were acquired with a cryostat (Leica CM1800, Leica Biosystems, Buffalo Grove, IL, USA) and mounted on Superfrost Plus™ adhesion microscope slides (Thermo Fisher Scientific, Waltham, MA, USA). Sections were stored at −80°C.

On the day of the experiment, the sections were thawed to room temperature for approximately 45 min before prewashing twice for 10 min in pre-incubation buffer (50 mM Tris-HCl [pH 7.4]) containing 0.5% bovine serum albumin (BSA).

First, a saturation assay was performed using sections from the frontal cortex of three subjects. The sections were then incubated for 60 min in assay buffer (50 mM Tris-HCl buffer containing 5 mM $MgCl_2$, 2 mM EGTA, and 0.5% BSA [pH 7.4]) containing varying concentrations (0 to 30 nM) of [³H]UCB-J for total binding (TB) and the same varying concentration of [³H]UCB-J with 10 mM of levetiracetam (Keppra®, UCB Pharma, Brussels, Belgium) for non-specific binding (NSB). Centrum semiovale sections were subjected to the same assay.

Incubation was terminated by three 5-min washes with ice-cold pre-incubation buffer followed by rapid rinsing in 4 °C deionized H_2O. After washing, the slides were air-dried and fixated overnight in a paraformaldehyde vapor chamber stored at 4 °C. The next day, the samples were moved to an exicator for a minimum of 60 min to remove any excess moisture and then placed in a cassette for autoradiography with tritium-sensitive image plates (BAS-IP TR2040 E, Science Imaging Scandinavia AB, Nacka, Sweden) along with radioactive tritium standards (ART0123, American Radiolabeled Chemical, Inc., St. Loui, MO, USA). The image plates were exposed for ~ 36 h. After exposure, the image plates were read using an Amersham™ Typhoon™ IP (Cytiva, Uppsala, Sweden) at 10 μm resolution (default settings). Calibration, quantification, and data evaluation were done using ImageJ software (NIH Image, Bethesda, MD, USA) [1]. The four-parameter general curve fit (David Rodbard, NIH) of decay-corrected tritium standards was used to convert mean pixel density (grayscale) to nCi/mg Tissue Equivalent (TE). The regions of interest were hand-drawn. TB was determined in the grey matter of slides without levetiracetam, while NSB was determined from grey

matter TB in slides containing 10 mM levetiracetam. Finally, the decay-corrected specific activity of [³H]UCB-J was used to convert nCi/mg TE to fmol/mg TE. Specific binding was calculated as the difference between TB and NSB.

[³H]UCB-J binding was plotted against the concentrations of [³H]UCB-J used for the saturation assay (, and a one-site (total and non-specific binding) model was used to fit the data to estimate the B_{max} and the K_D value using Graph-Pad Prism (v. 9.2.0; GraphPad Software, San Diego, CA, USA). The B_{max} of [³H]UCB-J was determined to be 497 fmol/mg TE (95% confidence interval (CI) = 466 to 530 fmol/mg TE) and the K_D to be 3.2 nM (95% CI = 2.6 to 3.8 nM). Since the levetiracetam-blocked sections yielded similar results as the unblocked white matter sections, we used white matter as a measure of NSB in the following experiments.

For regional estimation of SV2A B_{max}, all cortical sections from the different subjects were incubated in 20 nM [³H]UCB-J (6-7 times the K_D) diluted in assay buffer for 60 min. White matter from the same section was used as a proxy for NSB.

Figure S1
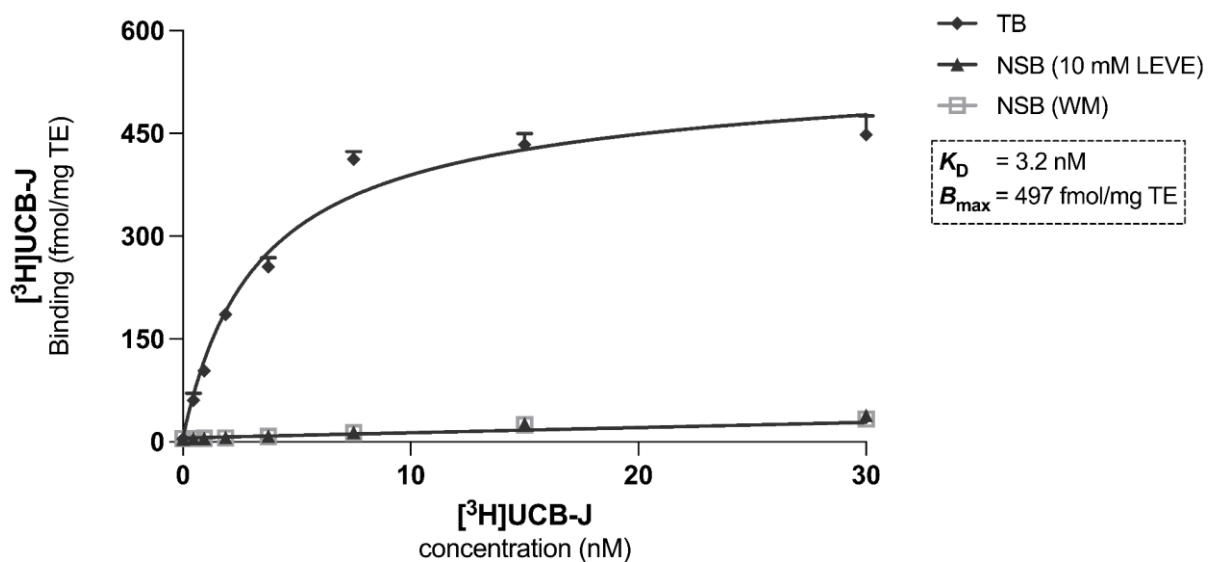
Figure S1. Saturation assay of [³H]UCB-J in frontal cortical human brain tissue from control subjects (average of 3). B_{max} and K_D were calculated using NSB from 10 mM levetiracetam (LEVE) blocked sections.

Figure S2
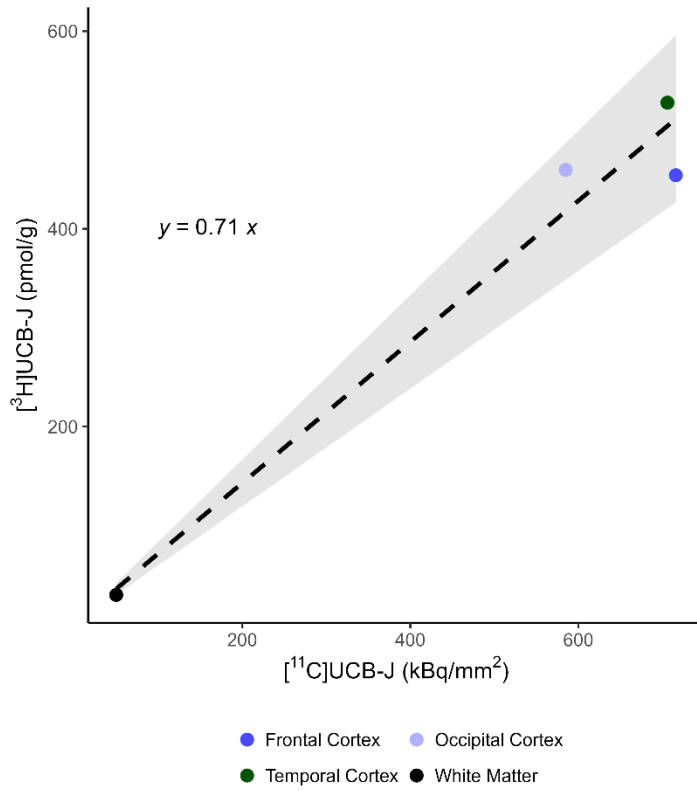
Figure S2. Linear regression between average regional [11C]UCB-J autoradiography from Varnäs et al. [2] and [3H]UCB-J autoradiography data (own).

Table S1

Demographics for the different samples included in the study.

	NRU PET cohort (N = 33)	NRU Auto-radiography (N = 7)	Varnäs 2020 Auto-radiography (N = 3)	Allen Human Brain Atlas mRNA (N = 6)
Sex				
Female	17 (52%)	6 (86%)	1 (33%)	1 (18%)
Male	16 (48%)	1 (14%)	2 (67%)	5 (83%)
Age (years)				
Mean (SD)	27 (6)	84 (11)	43 (NA)	43 (13)
Median [Min, Max]	24 [20, 44]	88 [68, 91]	34 [32, 62]	NA [24, 57]
IQ				
Mean (SD)	109 (7)			
Median [Min, Max]	108 [96, 125]			
Missing	3 (9%)			
Injected dose (MBq)				
Mean (SD)	400 (75)			
Median [Min, Max]	410 [224, 550]			
Weight-adjusted injected dose (MBq/kg)				
Mean (SD)	5.7 (1.4)			
Median [Min, Max]	5.5 [2.7, 9.7]			
Injected mass (ng/kg)				
Mean (SD)	8.9 (13.4)			
Median [Min, Max]	6.5 [1.2, 80.9]			

Quantification of SV2A mRNA levels

The description below was automatically generated by the *abagen* toolbox (v 0.1.3, https://abagen.readthedocs.io) and was copied without modification as was intended by the developers.

Regional microarray expression data were obtained from 6 post-mortem brains (1 female, ages 24.0-57.0, 42.50 ± 13.38) provided by the Allen Human Brain Atlas (AHBA, https://human.brain-map.org; [3]). Data were processed with the abagen toolbox (v 0.1.3-doc+2.g6f55425; https://github.com/rmarkello/abagen; [4]) using an 83-region volumetric atlas in MNI space.

First, microarray probes were reannotated using data provided by [5]; probes not matched to a valid Entrez ID were discarded. Next, probes were filtered based on their expression intensity relative to background noise [6], such that probes with intensity less than the background in ≥50.00% of samples across donors were discarded , yielding 31,569 probes . When multiple probes indexed the expression of the same gene, we selected and used the probe with the most consistent pattern of regional variation across donors (i.e., differential stability; [7]), calculated with:

$$\Delta_S(p) = \frac{1}{\binom{N}{2}} \sum_{i=1}^{N-1} \sum_{j=i+1}^{N} \rho[B_i(p), B_j(p)]$$

where ρ is Spearman's rank correlation of the expression of a single probe, p, across regions in two donors B_i and B_j, and N is the total number of donors. Here, regions correspond to the structural designations provided in the ontology from the AHBA.

The MNI coordinates of tissue samples were updated to those generated via non-linear registration using the Advanced Normalization Tools (ANTs; https://github.com/chrisfilo/alleninf). Samples were assigned to brain regions in the provided atlas if their MNI coordinates were within 2 mm of a given parcel. To reduce the potential for misassignment, sample-to-region matching was constrained by hemisphere and gross structural divisions (i.e., cortex, subcortex/brainstem, and cerebellum, such that e.g., a sample in the left cortex could only be assigned to an atlas parcel in the left cortex; [5]). All tissue samples not assigned to a brain region in the provided atlas were discarded.

Inter-subject variation was addressed by normalizing tissue sample expression values across genes using a robust sigmoid function [8]:

$$x_{norm} = \frac{1}{1 + \exp(-\frac{(x - \langle x \rangle)}{\mathrm{IQR}_x})}$$

where $\langle x \rangle$ is the median and IQR_x is the normalized interquartile range of the expression of a single tissue sample across genes. Normalized expression values were then rescaled to the unit interval:

$$x_{scaled} = \frac{x_{norm} - \min(x_{norm})}{\max(x_{norm}) - \min(x_{norm})}$$

Gene expression values were then normalized across tissue samples using an identical procedure. Samples assigned to the same brain region were averaged separately for each donor and then across donors, yielding a regional expression matrix with 83 rows, corresponding to brain regions.

Supplementary results

Figure S3

Surface (fsaverage)

Volume (MNI152)

65 ──── pmol/mL ──── 125
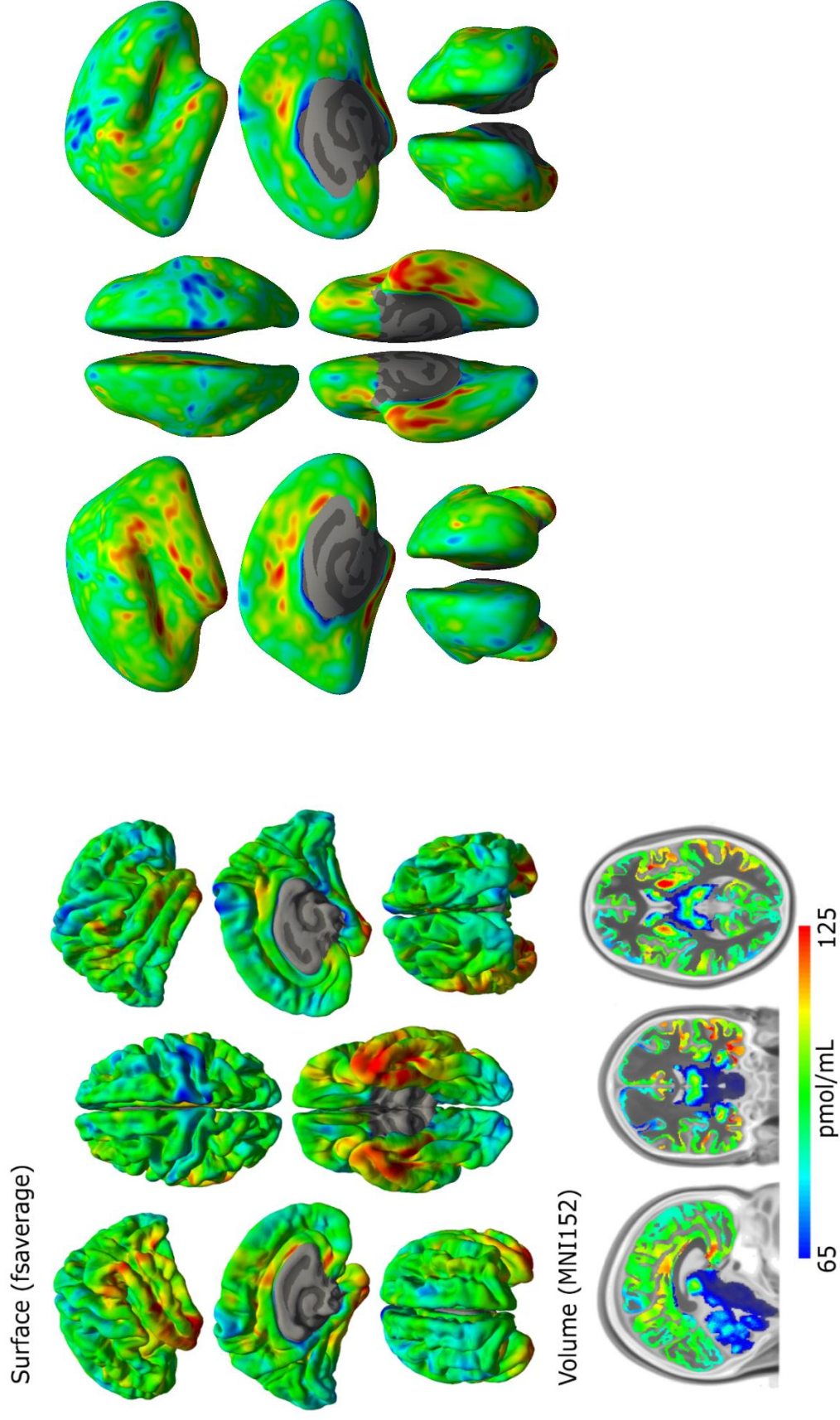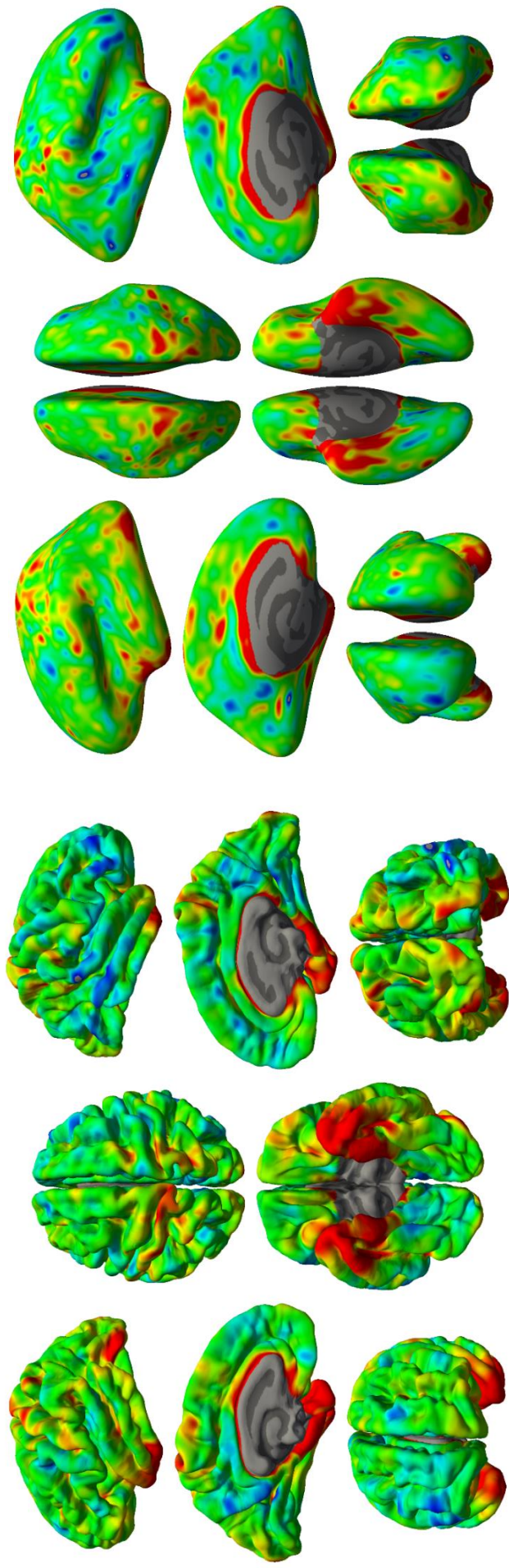
Figure S3. Variability maps. Standard deviation of SV2A density (B_{max}; pmol/mL) on the common FreeSurfer surface (top) and the common MNI152 space (bottom).

8

Figure S4

Surface (fsaverage)

Volume (MNI152)

Figure S4. Variability maps expressed as coefficient of variation (%) of SV2A density on the common FreeSurfer surface (top) and the common MNI152 space (bottom).

9

Table S2

Summary of SV2A B_{max} (pmol/mL) in individual regions in the left and right hemisphere, and for a weighted average (total).

Lobe	Region	Total			Left hemisphere			Right hemisphere			Left / right ratio		
		Mean	SD	COV (%)	Mean	SD	COV (%)	Mean	SD	COV (%)	Mean	SD	COV (%)
Cingulate	Caudal anterior cingulate	526	89	16.92	539	97	18.00	513	85	16.57	1.05	0.09	8.57
	Isthmus cingulate	484	78	16.12	483	76	15.73	485	82	16.91	1.00	0.06	6.00
	Posterior cingulate	577	89	15.42	583	95	16.30	572	85	14.86	1.02	0.06	5.88
	Rostral anterior cingulate	565	86	15.22	572	87	15.21	555	88	15.86	1.03	0.06	5.83
Frontal	Caudal middle frontal	564	84	14.89	574	87	15.16	554	81	14.62	1.04	0.03	2.88
	Frontal (total)	569	83	14.59	573	86	15.01	565	81	14.34	1.01	0.03	2.97
	Frontal pole	570	100	17.54	560	107	19.11	578	98	16.96	0.97	0.06	6.19
	Lateral orbitofrontal	564	87	15.43	574	93	16.20	555	84	15.14	1.03	0.05	4.85
	Medial orbitofrontal	559	86	15.38	558	88	15.77	560	87	15.54	1.00	0.05	5.00
	Paracentral	534	84	15.73	536	86	16.04	533	83	15.57	1.01	0.04	3.96
	Pars opercularis	625	93	14.88	626	99	15.81	624	88	14.10	1.00	0.05	5.00
	Pars orbitalis	578	88	15.22	568	97	17.08	586	86	14.68	0.97	0.08	8.25
	Pars triangularis	594	85	14.31	595	92	15.46	592	83	14.02	1.01	0.06	5.94
	Precentral	547	80	14.63	553	83	15.01	541	78	14.42	1.02	0.04	3.92
	Rostral middle frontal	580	86	14.83	582	92	15.81	579	83	14.34	1.00	0.05	5.00
	Superior frontal	569	84	14.76	574	86	14.98	564	83	14.72	1.02	0.02	1.96
Occipital	Cuneus	572	85	14.86	571	88	15.41	574	84	14.63	0.99	0.04	4.04
	Lateral occipital	520	81	15.58	510	87	17.06	530	79	14.91	0.96	0.07	7.29
	Lingual	560	82	14.64	563	85	15.10	557	80	14.36	1.01	0.03	2.97
	Occipital (total)	546	82	15.02	540	85	15.74	551	80	14.52	0.98	0.04	4.08
	Pericalcarine	574	87	15.16	562	85	15.12	584	91	15.58	0.96	0.03	3.12
Parietal	Inferior parietal	598	84	14.05	587	87	14.82	607	86	14.17	0.97	0.06	6.19
	Parietal (total)	577	85	14.73	576	88	15.28	578	83	14.36	1.00	0.04	4.00
	Postcentral	524	80	15.27	527	86	16.32	521	76	14.59	1.01	0.04	3.96
	Precuneus	616	88	14.29	616	90	14.61	615	87	14.15	1.00	0.02	2.00
	Superior parietal	542	84	15.50	544	85	15.62	541	84	15.53	1.01	0.03	2.97
	Supramarginal	613	92	15.01	618	97	15.70	609	90	14.78	1.02	0.06	5.88
Temporal	Banks of the superior temporal sulcus	631	89	14.10	632	93	14.72	631	91	14.42	1.00	0.07	7.00
	Entorhinal	491	102	20.77	502	110	21.91	479	96	20.04	1.05	0.10	9.52
	Fusiform	577	91	15.77	582	95	16.32	573	88	15.36	1.01	0.04	3.96
	Inferior temporal	594	98	16.50	598	106	17.73	590	92	15.59	1.01	0.05	4.95
	Insula	566	81	14.31	568	83	14.61	565	82	14.51	1.01	0.05	4.95
	Middle temporal	622	90	14.47	618	97	15.70	625	86	13.76	0.99	0.06	6.06
	Parahippocampal	541	98	18.11	538	104	19.33	545	98	17.98	0.99	0.09	9.09
	Superior temporal	606	89	14.69	603	95	15.75	609	84	13.79	0.99	0.05	5.05
	Temporal (total)	595	91	15.29	596	97	16.28	595	87	14.62	1.00	0.04	4.00
	Temporal pole	529	105	19.85	541	111	20.52	517	106	20.50	1.05	0.10	9.52
	Transverse temporal	600	85	14.17	607	91	14.99	591	84	14.21	1.03	0.07	6.80

Subcortical	598	108	18.06	616	121	19.64	585	103	17.61	1.05	0.09	8.57
Accumbens												
Amygdala	472	84	17.80	471	89	18.90	474	82	17.30	0.99	0.05	5.05
Caudate	539	81	15.03	548	81	14.78	531	83	15.63	1.04	0.05	4.81
Cerebellum	341	55	16.13	347	58	16.71	335	54	16.12	1.04	0.04	3.85
Hippocampus	350	64	18.29	351	67	19.09	348	62	17.82	1.01	0.05	4.95
Pallidum	304	52	17.11	315	59	18.73	294	51	17.35	1.08	0.12	11.11
Pons	95	30	31.58									
Putamen	604	88	14.57	618	92	14.89	591	85	14.38	1.05	0.03	2.86
Thalamus	352	55	15.62	353	55	15.58	351	57	16.24	1.01	0.07	6.93
Ventral dc	170	37	21.76	173	39	22.54	167	37	22.16	1.04	0.10	9.62
White matter	12	19	158.33									

Table S3

Table of vertex clusters showing positive associations between SV2A density and IQ. Adjusted *p*-values are Bonferroni-corrected (correction factor of 3; subcortical + 2 hemispheres). Coordinates refer to MNI space.

| Hemisphere	Size (mm²)	MNIX	MNIY	MNIZ	Region annotation	*p*-value	Adjusted p-value
lh	298.86	-20.9	-40.9	-10.1	Parahippocampal	0.009	0.027
lh	151.41	-9.3	27.3	-20	Medial orbitofrontal	0.015	0.046
lh	145.07	-53.1	-24	-4	Superior temporal	0.015	0.046
lh	124.81	-31.9	23.3	-14.5	Lateral orbitofrontal	0.017	0.050
lh	113.82	-53.8	-12.3	-21.1	Middle temporal	0.018	0.055
lh	103.78	-41.2	-25.8	1.7	Transverse temporal	0.020	0.060
lh	100.60	-7.1	59.6	-16	Frontal pole	0.020	0.060
lh	37.79	-39.1	-34.1	7.5	Superior temporal	0.039	0.116
lh	31.31	-39	44	4.5	Rostral middle frontal	0.043	0.130
lh	24.92	-17.2	-48.1	-0.8	Isthmus cingulate	0.047	0.142
rh	241.17	22.8	-20.3	-24.1	Parahippocampal	0.012	0.037
rh	159.79	37.6	-29.3	12.6	Transverse temporal	0.016	0.047
rh	137.15	13.7	32.2	-23.2	Lateral orbitofrontal	0.018	0.053
rh	132.87	49.4	-6.4	-11.9	Superior temporal	0.019	0.056
rh	124.05	9.6	-75.1	-0.2	Lingual	0.020	0.061
rh	87.30	57.1	-46.5	-13.6	Inferior temporal	0.025	0.074
rh	56.66	4.6	3.1	38.1	Posterior cingulate	0.031	0.094
rh	48.44	7.9	45.5	-16	Medial orbitofrontal	0.033	0.100
rh	36.74	12.4	58.7	-15.7	Frontal pole	0.038	0.113
rh	26.58	29.2	25.8	-1.3	Lateral orbitofrontal	0.044	0.133

Figure S5
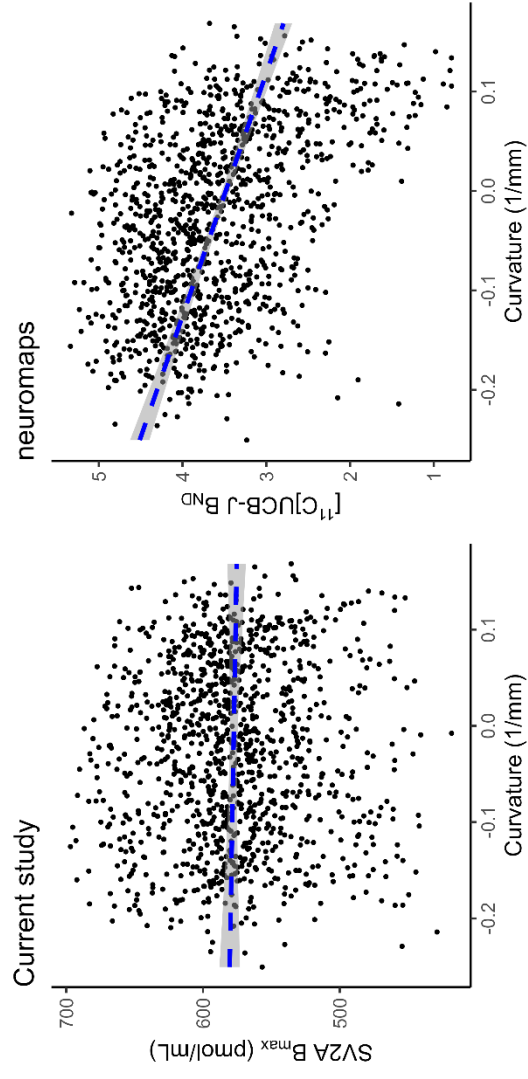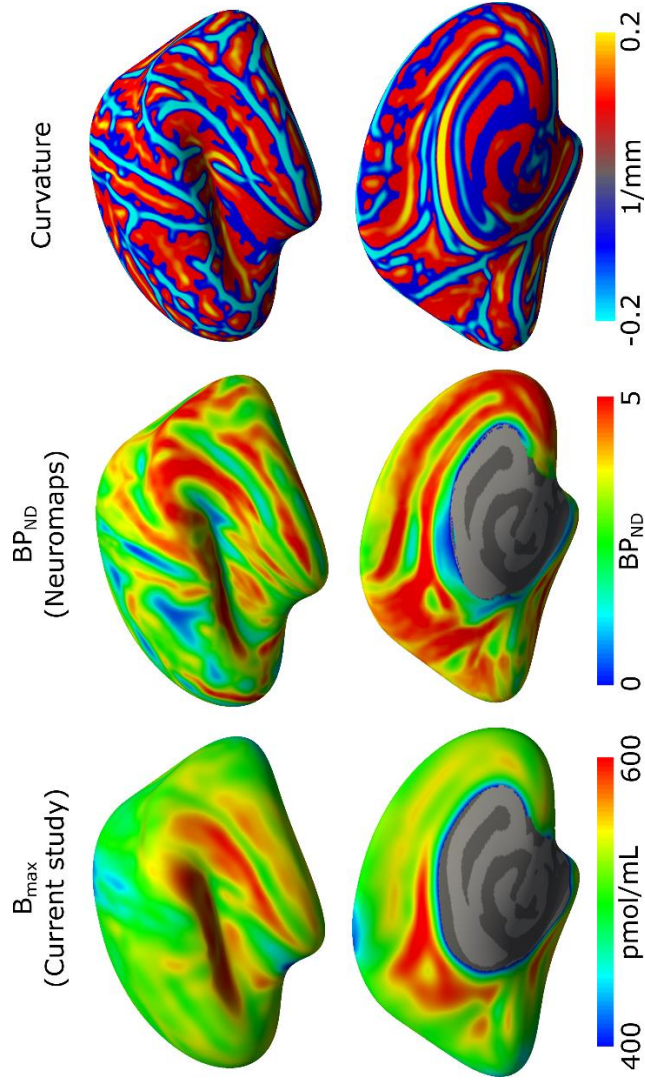
Figure S5. Comparison to a previously published average map of [¹¹C]UCB-J non-displaceable binding potential (BP_{ND}) distributed as part of the *neuromaps* toolbox [9]. Top panel: Average surface-based SV2A density (B_{max}) (left), volume-based [¹¹C]UCB-J BP_{ND} projected to the cortical surface (middle), and curvature of the *fsaverage* surface (right). Bottom: Comparison of the vertex-wise cortical data to curvature of the brain SV2A density (left; r(1145) = -0.02, p = 0.193) and *neuromaps'* [¹¹C]UCB-J BP_{ND} map (right; r(1145) = -0.42, p < 0.0001).

Regional [¹¹C]UCB-J BP_{ND} values were obtained using the map provided in the *neuromaps* toolbox (v 0.0.3) [9]. More details about this [¹¹C]UCB-J BP_{ND} dataset are provided in [10]. Following [10], the Cammoun atlas (MNI152NLin2009aSym, scale033) available from the *netneurotools* toolbox (v 0.2.3, https://netneurotools.readthedocs.io) was used to extract average regional BP_{ND} values directly from the volumetric map in MNI152 space. The Cammoun atlas contains a 1-1 pairing to the cortical and subcortical regions defined in FreeSurfer. Regional SV2A densities and [¹¹C]UCB-J BP_{ND} values were averaged between the left and right hemispheres, where applicable, and compared using Pearson's correlation.

Greve et al.[11] have demonstrated that partial volume effects can be apparent of surface models of the cortex as stripe patterns, which are often aligned with the brain's curvature. The association between PET-derived values and the surface curvature, as a proxy of PVEs, was evaluated using Spearman's correlation. Empirical p-values were obtained using bootstrap with 10,000 resamples. To avoid bias due to the strong spatial autocorrelation of smoothed values on a fine surface model, such as the standard *fsaverage* surface, the B_{max} and BP_{ND} maps were resampled to a lower resolution surface created with an icosahedral tessellation of order 3 (i.e., 1147 vertices for both hemispheres, excluding the medial wall).

Tables S4 and S5: See Excel file

References

1. Schneider, C. A., Rasband, W. S. & Eliceiri, K. W. NIH Image to ImageJ: 25 years of image analysis. *Nat. Methods* **9**, 671–675 (2012).

2. Varnäs, K., Stepanov, V. & Halldin, C. Autoradiographic mapping of synaptic vesicle glycoprotein 2A in non-human primate and human brain. *Synapse* **74**, e22157 (2020).

3. Hawrylycz, M. J. *et al.* An anatomically comprehensive atlas of the adult human brain transcriptome. *Nature* **489**, 391–399 (2012).

4. Markello, R. D. *et al.* Standardizing workflows in imaging transcriptomics with the abagen toolbox. *Elife* **10**, (2021).

5. Arnatkevičiūtė, A., Fulcher, B. D. & Fornito, A. A practical guide to linking brain-wide gene expression and neuroimaging data. *Neuroimage* **189**, 353–367 (2019).

6. Quackenbush, J. Microarray data normalization and transformation. *Nat. Genet.* **32**, 496–501 (2002).

7. Hawrylycz, M. *et al.* Canonical genetic signatures of the adult human brain. *Nat. Neurosci.* **18**, 1832–1844 (2015).

8. Fulcher, B. D., Little, M. A. & Jones, N. S. Highly comparative time-series analysis: the empirical structure of time series and their methods. *J. R. Soc. Interface* **10**, 20130048 (2013).

9. Markello, R. D. *et al.* neuromaps: structural and functional interpretation of brain maps. *Nat Methods* **19**, 1472–1479 (2022).

10. Hansen, J. Y. *et al.* Local molecular and global connectomic contributions to cross-disorder cortical abnormalities. *Nat Commun* **13**, 4682 (2022).

11. Greve, D. N. *et al.* Cortical surface-based analysis reduces bias and variance in kinetic modeling of brain PET data. *Neuroimage* **92**, 225–236 (2014).

II

ARTICLE   OPEN

Effects of escitalopram on synaptic density in the healthy human brain: a randomized controlled trial

Annette Johansen [1,2], Sophia Armand [1,3], Pontus Plavén-Sigray[1], Arafat Nasser[1], Brice Ozenne[1,4], Ida N. Petersen[5], Sune H. Keller[5], Jacob Madsen[5], Vincent Beliveau [1,6], Kirsten Møller [2,7], Alexandra Vassilieva[2,7], Christelle Langley [8], Claus Svarer [1], Dea S. Stenbæk[1,3], Barbara J. Sahakian[8] and Gitte M. Knudsen [1,2 ✉]

Selective serotonin reuptake inhibitors (SSRIs) are widely used for treating neuropsychiatric disorders. However, the exact mechanism of action and why effects can take several weeks to manifest is not clear. The hypothesis of neuroplasticity is supported by preclinical studies, but the evidence in humans is limited. Here, we investigate the effects of the SSRI escitalopram on presynaptic density as a proxy for synaptic plasticity. In a double-blind placebo-controlled study (NCT04239339), 32 healthy participants with no history of psychiatric or cognitive disorders were randomized to receive daily oral dosing of either 20 mg escitalopram ($n = 17$) or a placebo ($n = 15$). After an intervention period of 3–5 weeks, participants underwent a [^{11}C]UCB-J PET scan (29 with full arterial input function) to quantify synaptic vesicle glycoprotein 2A (SV2A) density in the hippocampus and the neocortex. Whereas we find no statistically significant group difference in SV2A binding after an average of 29 (range: 24–38) days of intervention, our secondary analyses show a time-dependent effect of escitalopram on cerebral SV2A binding with positive associations between [^{11}C]UCB-J binding and duration of escitalopram intervention. Our findings suggest that brain synaptic plasticity evolves over 3–5 weeks in healthy humans following daily intake of escitalopram. This is the first in vivo evidence to support the hypothesis of neuroplasticity as a mechanism of action for SSRIs in humans and it offers a plausible biological explanation for the delayed treatment response commonly observed in patients treated with SSRIs. While replication is warranted, these results have important implications for the design of future clinical studies investigating the neurobiological effects of SSRIs.

INTRODUCTION

Drugs targeting the serotonin system, specifically the serotonin transporter, have long been the primary pharmacological treatment for affective and anxiety-related disorders [1]. The most widely used group is the selective serotonin reuptake inhibitors (SSRIs), presumed to work by increasing serotonergic neurotransmission [2]. Serotonin plays an important modulatory role in the brain, including regulation of mood, sleep, cognition, and behaviour, and in the early development of the central nervous system [3, 4]. Further, years of preclinical studies have established a link between the serotonin system and cellular processes such as cytoskeletal rearrangements, long-term potentiation, and neuronal firing – processes that collectively are regarded as forms of neuroplasticity [2, 5]. Functionally, neuroplasticity can be thought of as the ability of the brain to change and adapt to physiological or psychological stimuli to uphold homeostasis [6].

Despite years of research, the question of how inhibition of the serotonin transporter leads to symptom relief in neuropsychiatric conditions, remains unresolved. Major depressive disorder (MDD) is a vastly heterogeneous syndrome [7] and up to 35% of patients

treated with SSRIs do not reach a state of remission [8]. Thus, a deeper understanding of the neurobiological effects of SSRIs, together with better patient stratification [9], is needed to tailor treatment to individual patients and pursue other treatment strategies for patients who are unlikely to benefit from SSRIs.

One hypothesis for the mechanism of action in neuropsychiatric disorders is that strengthened serotonergic neurotransmission induces neuroplasticity and, in turn, improves cognitive and emotion processing [10–12]. Neuroplastic effects have foremost been demonstrated for the visual system; in adult rats, chronic treatment with the SSRI fluoxetine has been shown to reactivate a critical period-like plasticity in the visual cortex [13, 14]. However, whether neuroplasticity is central to the effects of SSRIs in humans has been difficult to investigate, mainly due to the lack of specific biomarkers. A suggested proxy is a change in cortical thickness or brain volume, as measured with MRI, in response to, e.g., learning new skills or tasks, such as juggling [15]. However, by using PET, it is possible to non-invasively quantify molecular biomarkers that more specifically reflect plasticity in vivo. Here, we use the PET radioligand [^{11}C]UCB-J that binds to the Synaptic Vesicle

[1]Neurobiology Research Unit, Copenhagen University Hospital Rigshospitalet, Copenhagen, Denmark. [2]Department of Clinical Medicine, Faculty of Health and Medical Sciences, University of Copenhagen, Copenhagen, Denmark. [3]Department of Psychology, Faculty of Social Sciences, University of Copenhagen, Copenhagen, Denmark. [4]Department of Public Health, Section of Biostatistics, University of Copenhagen, Copenhagen, Denmark. [5]Department of Clinical Physiology and Nuclear Medicine, Copenhagen University Hospital Rigshospitalet, Copenhagen, Denmark. [6]Department of Neurology, Medical University of Innsbruck, Innsbruck, Austria. [7]Department of Neuroanaesthesiology, Copenhagen University Hospital Rigshospitalet, Copenhagen, Denmark. [8]Department of Psychiatry, University of Cambridge, Cambridge, UK. ✉email: gmk@nru.dk

glycoprotein 2A (SV2A), which enables visualization and quantification of pre-synaptic density [16], as a proxy for synaptic plasticity.

PET studies on several neuropsychiatric disorders linked to synaptic dysfunction, including depression, have found lower cerebral SV2A density in patients compared to healthy individuals [17–22]. So far, the only investigation of a pharmacological intervention on SV2A density in humans is a study that examined the acute effect of a single administration of the rapid-acting antidepressant ketamine, and they found no changes for healthy participants and psychiatric patients 24 h after the intervention, but a post-hoc analysis indicated possible effects in a subgroup of patients [23]. Whereas ketamine's psychoactive effects are hyper-acute, with antidepressant effects reaching a maximum one day after administration [24], the clinical effects of SSRIs emerge much slower. Some studies suggest that SSRIs have acute or subacute effects on cognition, e.g., affective processing bias [25–27], but it generally takes several weeks before symptom relief occurs in patients with depression [28–31]. This suggests that clinical effects result from neurobiological changes that emerge gradually, likely over the course of several weeks.

Given the limited knowledge of SSRIs' neurobiological effects in humans, such as their capacity to induce neuroplasticity, we here aim to investigate if SSRI administration over several weeks can alter synaptic density in the healthy human brain, specifically in the hippocampus and the neocortex. The hippocampus is often the target of research on neuroplasticity as it is a key region in learning and memory, and patients with severe depression have been found to have lower SV2A in the hippocampus and several neocortical regions [20]. Although categorized as a *mood* disorder, symptoms of depression indicate global affection of the brain, with deficits related to, e.g., memory and executive function, that can improve independent of change in depression scores following SSRI treatment [32]. For this reason, we chose the global neocortex for our primary investigation rather than specific sub-regions.

Here, we used a double-blind, semi-randomized, placebo-controlled design to test the hypothesis that healthy participants receiving daily SSRI administration would have higher SV2A binding in the hippocampus and the neocortex than those receiving a placebo. We further hypothesized that SV2A binding would be positively associated with the duration of escitalopram intervention.

METHODS
Study design
The study was conducted in conjunction with a cross-sectional (i.e., single-scan), double-blinded, semi-randomized, placebo-controlled study (see Supplementary Fig S2) on the cognitive effects of escitalopram [33] preregistered at ClinicalTrials.gov (NCT04239339). The study was conducted at the Copenhagen University Hospital, Rigshospitalet, between May 2020 and October 2021. Approval was granted by the Danish ethics committee for the capital region of Copenhagen (journal ID: H-18038352, with amendments 71579, 73632, and 78565).

All participants were recruited from a database of individuals who had expressed interest in participating in brain imaging studies. Following information about the study, including potential side effects of escitalopram, participants gave their written consent. Next, participants underwent a screening procedure, including medical history, physical and neurological examination, and screening for current or previous psychiatric disorders according to in- and exclusion criteria (see Supplementary file for complete list). Following the screening procedure and neuropsychological testing of IQ (assessed using the Reynolds Intellectual Screening Test (RIST) [34]) and reaction time, participants were semi-randomized to receive either escitalopram (20 mg daily in capsules of 10 mg) or a placebo in identical capsules that were manufactured and distributed by the Capital Region Pharmacy. The dose of escitalopram was chosen to reflect typical clinical practice (i.e., 10–20 mg) for treating conditions such as MDD, and to minimize the risk of a false-negative result due to low dosing.

Randomization balanced with regards to age, sex, and IQ was done by a research administrator not otherwise involved in data collection or analysis. Participants were instructed to take one capsule daily by mouth for three days and then increase to two capsules daily (i.e., full dose). The aim was an intervention period of a minimum 3 weeks, and for logistical purposes and to allow room for unforeseen events (e.g., illness or technical issues), participants could continue the intervention for up to 5 weeks. After the intervention period, all participants came in for extensive neuropsychological testing and MRI examination. On intervention day 10 and the day of neuropsychological testing and MRI, a blood sample was collected to measure s-escitalopram steady-state levels as confirmation of drug adherence. Participants were instructed only to take their daily dose of medication after the blood sample had been drawn. S-escitalopram was measured with an ultra-performance liquid chromatography-tandem mass spectrometer (UPLC-MS/MS; Filadelfia Epilepsy Hospital, Dianalund, Denmark).

The main study included 66 healthy participants, for which we have reported the neuropsychological outcomes [33]. A subset of 32 participants underwent [11C]UCB-J PET scanning after the main study program was completed and while still double-blinded to the intervention. Participants were asked at the time of inclusion whether they, in addition to the described study program, agreed to undergo a PET scan. The sample size for the PET cohort (16 participants in each group) was calibrated to detect a 10% change (Cohen's d $\cong$ 1) in [11C]UCB-J V_T in the hippocampus, at 80% power and a significance level of 0.05, based on data from Finnema et al. [35]. The data presented here are based on these 32 participants.

MRI acquisition and preprocessing
All participants underwent MRI scans in a Siemens Magnetom Prisma 3 T scanner (Siemens AG, Erlangen, Germany) using a Siemens 32-channel head coil. Structural T1- and T2-weighted images were acquired (T1 protocol: Isotropic $0.9 \times 0.9 \times 0.9$ mm^3 resolution, repetition time = 2000 ms, echo time = 2.58 ms, inversion time = 972 ms, and flip angle = 8°; T2 protocol: Isotropic $0.9 \times 0.9 \times 0.9$ mm^3 resolution, repetition time = 3200 ms, echo time = 408 ms). Grey matter masks for PET processing were extracted from T1- and T2-weighted images using the multispectral segmentation routine in SPM12 (Functional Imaging Laboratory, the Wellcome Trust Centre for Neuroimaging, London, UK). Cortical thickness and hippocampal volume were derived from the T1-weigthed images using the standard anatomical processing stream (recon-all) from Free-Surfer (v. 7.2, https://surfer.nmr.mgh.harvard.edu/) [36], with manual refinement of the pial surface using the T2-weighted images.

PET acquisition
Radiosynthesis of [11C]UCB-J was modified on the basis of Nabulsi et al. [37], as described in detail in the Supplementary file. All participants were scanned with a high-resolution research tomography (HRRT) PET scanner (CTI/Siemens, Knoxville, TN, USA). Following a six-min transmission scan, a 120 min PET scan was started at the time of intravenous [11C]UCB-J bolus injection (over ~20 sec). PET data were acquired in 3D list mode and reconstructed into 40 frames (8×15 s, 8×30 s, 4×60 s, 5×120 s, 10×300 s, 5×300 s) using a 3D OP-OSEM algorithm with modelling of the point-spread-function [38, 39], and attenuation corrected using the HRRT maximum a posteriori transmission reconstruction method (MAP-TR) [40]. Each image frame consisted of 207 planes of 256×256 voxels of $1.22 \times 1.22 \times 1.22$ mm^3.

Arterial blood acquisition and analysis
For determination of the arterial input function, arterial blood samples were collected from a 20 G catheter which had been placed in the radial artery under local anesthesia. For the first 15 min of each scan, whole blood radioactivity was continuously measured (2-s intervals, flow = 8 mL/min) using an Allogg ABSS autosampler (Allogg Technology, Mariefred, Sweden). In addition, manual blood samples were drawn at 2.5, 5, 10, 25, 40, 60, 90, and 120 min for measuring radioactivity in blood and plasma using a gamma counter (Cobra II auto-gamma, Packard, Packard Instrument Company, Meriden, CT, USA) that was cross-calibrated to the PET scanner biweekly. Plasma was extracted after centrifugation of arterial blood at 2246xg for 7 min at 4 °C. To measure intact tracer and radiolabeled metabolites, plasma samples up until 90 min were analyzed using radio-HPLC (see the Supplementary file for full detail).

The plasma free fraction (f_P) of [11C]UCB-J was determined by the equilibrium dialysis method as described in the Supplementary file.

PET image processing

All PET images were motion corrected using the AIR software with the reconcile command (Automated Image Registration, v. 5.2.5, LONI, UCLA, http://air.bmap.ucla.edu/AIR5/). Tissue time-activity curves were extracted from automatically defined ROIs using the PVElab software (https://nru.dk/index.php/allcategories/category/30-software). The neocortex ROI was defined as a weighted average of the individual subregions (frontal, parietal, temporal, occipital and insular cortices). The PVElab pipeline used an unfiltered summation PET image that was automatically co-registered to the participant's T1-weighted MR image using SPM12. Segmented T1- and T2-weighted MR images were then used to extract grey matter values from each ROI defined with a brain atlas, as previously described [41]. Co-registration and ROI placement were visually inspected for each subject; no manual correction was needed. No correction for partial volume effects was applied. The ROI for the centrum semiovale (white matter) was obtained from the PVElab region with the Müeller-Gartner partial volume correction method and was further eroded twice with a 3D erosion operator to minimize partial volume effects. The final volume had a mean (SD) of 7.45 (2.63) mL.

Kinetic modeling

Kinetic modelling of [11C]UCB-J PET data was performed in R (v. 4.2.2, R Foundation, Vienna, Austria) using the kinfitr package (v. 0.6) [42]. Time-activity curves from all ROIs were fitted to the one-tissue compartment model (1TCM) using the subject's metabolite-corrected arterial input function to estimate the total volume of distribution (V_T), an index of SV2A binding. The fraction of blood volume (v_B) was excluded from the model as it did not improve the model fits or change V_T estimates, which is in agreement with previous kinetic evaluations [35].

In addition, as a complementary analysis, time-activity curves from the hippocampus and neocortex were fitted to the simplified reference tissue model 2 (SRTM2) to estimate the non-displaceable binding potential (BP_{ND}) using the white matter region centrum semiovale as a pseudo-reference region [43, 44]. The median k2 from 1TC modelling of centrum semiovale was used as a global k2' (0.035 min^{-1}).

Statistical analyses

The distributions of demographic variables and PET scan parameters were visually compared between the groups and formally tested with a Welch two-sample t-test for continuous variables and Chi-squared tests for group sex ratios. Our primary hypotheses of higher [11C]UCB-J V_T in the hippocampus and the neocortex in the escitalopram group compared to the placebo group were tested using Welch two-sample t-tests. As a sensitivity analysis, we also conducted group comparisons using general linear models with randomization variables (age, sex, and IQ) as covariates. Improvement of model fits was assessed with a likelihood ratio test comparison of nested models.

As a secondary analysis, we investigated if there was an effect on [11C]UCB-J V_T dependent on escitalopram intervention duration: using a likelihood-ratio test, we compared a linear regression model including a group-by-intervention duration interaction term to a nested model where the group term was excluded. The models were also performed with age, sex, and IQ as covariates. Partial correlation coefficients (r_p) were calculated based on the linear models [45]. We further investigated the effect of s-escitalopram concentration (log-transformed) on [11C]UCB-J V_T using linear regression.

Group means for [11C]UCB-J V_T estimates for other regions are listed in the Supplementary file (Table S1). These include neocortical ROIs: Orbital frontal, anterior cingulate, insula, superior temporal gyrus, parietal, medial inferior temporal gyrus, superior frontal, occipital, sensory-motor, dorsolateral prefrontal gyrus, ventrolateral prefrontal gyrus. Subcortical ROIs: Centrum semiovale, thalamus, caudate, putamen, entorhinal cortex, amygdala, raphe nuclei. Neocortex and hippocampus BP_{ND}s from the SRTM2 model were compared with two-sample t-tests.

As exploratory analyses, we investigated the effects of escitalopram versus placebo, intervention duration, and s-escitalopram concentration on hippocampus volume adjusted for age, sex, and intracranial volume (ICV). Lastly, for the neocortical subregions frontal, parietal, temporal, occipital, and insular cortex, we examined if there was a group and intervention duration effect on cortical thickness using linear regressions, as described for [11C]UCB-J V_Ts, with age and sex as covariates.

All tests were performed as two-sided tests. Secondary and exploratory analyses were corrected for multiple comparisons according to the number of regions investigated, using the Bonferroni-Holm method. Statistical analyses were performed in R (v. 4.2.2).

RESULTS

Demographics and scan-related parameters

The escitalopram and placebo groups were similar in age, sex distribution, and PET-related variables, including [11C]UCB-J plasma free fraction (Table 1). This was also the case when leaving out three participants without full arterial input functions, all from the placebo group. Serum-escitalopram measurements confirmed the correct group assignment and that all participants in the escitalopram group had been compliant.

Table 1. Subject demographics and [11C]UCB-J PET scan-related parameters.

	Placebo (N = 15[1])	Escitalopram (N = 17)	p-value
Sex			
Female	8 (53%)	12 (71%)	0.52
Male	7 (47%)	5 (29%)	
Age (years)			
Mean (SD)	22.8 (2.9)	25.2 (5.8)	0.15
Median [Min, Max]	21.7 [19.9, 31.6]	22.7 [19.6, 41.9]	
IQ			
Mean (SD)	108 (5.9)	112 (8.0)	0.11
Median [Min, Max]	108 [94, 118]	113 [99, 129]	
Intervention duration (days)			
Mean (SD)	30.4 (4.7)	28.2 (3.3)	0.14
Median [Min, Max]	32.0 [22.0, 38.0]	27.0 [24.0, 35.0]	
S-escitalopram, day 10 (nmol/L)			
Mean (SD)	0 (0)	86 (75)	-
Median [Min, Max]	0 [0, 0]	68 [28, 338]	
S-escitalopram, follow-up (nmol/L)			
Mean (SD)	0 (0)	84 (56)	-
Median [Min, Max]	0 [0, 0]	69 [28, 263]	
Injected dose (MBq)			
Mean (SD)	401 (101)	410 (63)	0.77
Median [Min, Max]	415 [124, 550]	414 [251, 526]	
Injected mass (ng/kg)			
Mean (SD)	12.2 (19.5)	8.9 (7.2)	0.53
Median [Min, Max]	8.8 [1.2, 80.9]	6.7 [1.4, 29.3]	
f_P			
Mean (SD)	0.36 (0.05)	0.36 (0.05)	0.87
Median [Min, Max]	0.37 [0.29, 0.46]	0.38 [0.26, 0.42]	

P-values refer to two-sample t-tests for continuous variables and Chi-square tests for categorical variables.
[1]Includes three participants in the placebo group who did not have a complete arterial input function. Group characteristics (central tendency measures and spread) did not change noticeably when leaving out these participants.

Primary analyses

There was no statistically significant difference in [^{11}C]UCB-J binding between the escitalopram and placebo group in our primary ROIs, the hippocampus and the neocortex, after an average intervention period of 29 days (Fig. 1). The mean (SD) V_T in the hippocampus was 15.1 (2.2) mL/cm^3 for escitalopram ($n = 17$) vs. 14.3 (1.9) mL/cm^3 for placebo ($n = 12$), corresponding to Cohen's $d = 0.43$ (95% CI [−0.36, 1.20], $p = 0.26$). In the neocortex, the mean (SD) V_T was 18.3 (2.5) mL/cm^3 for escitalopram ($n = 17$) vs. 17.6 (2.0) mL/cm^3 for placebo ($n = 12$) corresponding to Cohen's $d = 0.31$, (95% CI [−0.47, 1.08], $p = 0.41$).

Including age, sex, and IQ as covariates did not reveal any significant group differences in the neocortex or the hippocampus (Supplementary Table S2). Likelihood ratios tests evaluating the improvement of model fits for the neocortex and the hippocampus resulted in the following p-values; $p > 0.76$ for age; $p < 0.071$ for sex; $p < 0.014$ for IQ. None of the covariates improved the model fit for the centrum semiovale (all p-values > 0.32).

Neocortical subregions and subcortical regions were not included in our a priori hypothesis; none of these regions showed significant differences in [^{11}C]UCB-J V_T estimates between escitalopram and placebo groups as compared with Welch two-sample t-tests (Supplementary Table S1). For completeness, we also evaluated the non-displaceable binding potential (BP_{ND})

based on reference tissue modelling using white matter as a reference region (Fig. S2). Mean (SD) BP_{ND} in the hippocampus was 2.65 (0.36) for escitalopram ($n = 17$) vs. 2.70 (0.38) for placebo ($n = 15$)($p = 0.67$), while BP_{ND} in the neocortex was 3.42 (0.38) for escitalopram ($n = 17$) vs. 3.57 (0.42) for placebo ($p = 0.31$).

Secondary analyses

Effect of intervention duration on [^{11}C]UCB-J binding. As the length of the intervention period ranged from 24 to 35 days for the escitalopram group, we investigated if longer exposure to escitalopram was associated with higher [^{11}C]UCB-J V_T. A likelihood-ratio test between a linear regression model including a *group-by-intervention duration* interaction term and a nested model where the *group* term was excluded, indicated a time-dependent group effect of escitalopram: the test resulted in a p-value of 0.020 ($p_{adj.} = 0.039$) for the neocortex and 0.058 ($p_{adj.} = 0.058$) for the hippocampus We then modelled the drug-specific effect of the duration of escitalopram intervention on [^{11}C]UCB-J V_T: in the neocortex (Fig. 2A) we found a positive effect of time for the escitalopram group, estimated to be +0.41 mL/cm^3 per day ($r_\rho = 0.46$, $p = 0.016$), whereas it was −0.12 mL/cm^3 per day ($r_\rho = -0.18$, $p = 0.38$) for the placebo group. Similarly, for the hippocampus (Fig. 2B), the effect of time on [^{11}C]UCB-J V_T was +0.25 mL/cm^3 per day ($r_\rho = 0.31$, $p = 0.11$) for the escitalopram group, whereas for the placebo group, it was −0.14 mL/cm^3 per day ($r_\rho = -0.22$, $p = 0.26$).

When including age, sex, and IQ in the models, the effects of intervention duration in the escitalopram group were further strengthened: in the neocortex, the effect of intervention duration on [^{11}C]UCB-J V_T was +0.47 mL/cm^3 per day ($r_\rho = 0.58$, $p = 0.003$) for the escitalopram group, while there was no effect for the placebo group: −0.01 mL/cm^3 per day ($r_\rho = -0.01$, $p = 0.95$). For the hippocampus, the effect of intervention duration was +0.30 mL/cm^3 per day ($r_\rho = 0.40$, $p = 0.048$) for the escitalopram group, while there was no effect for the placebo group: −0.06 mL/cm^3 per day ($r_\rho = -0.11$, $p = 0.62$). The effect of intervention duration was also observed for the centrum semiovale. All model estimates are listed in Supplementary Table S3.

Effect s-escitalopram concentration on [^{11}C]UCB-J binding. We also investigated the effect of participants' s-escitalopram level on [^{11}C]UCB-J V_T. The estimate of the effect of the log-transformed concentrations was +0.81 mL/cm^3 per log[ng/L] ($r_\rho = 0.18$, $p = 0.48$) in the neocortex, and +0.39 mL/cm^3 per log[ng/L] ($r_\rho = 0.10$, $p = 0.70$) in the hippocampus. The inclusion of age, sex,
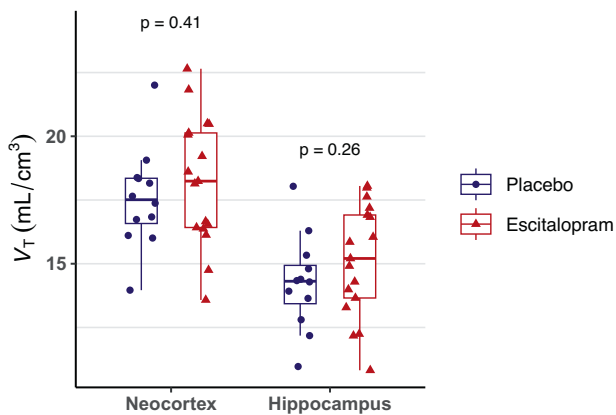
Fig. 1 Effects of escitalopram on SV2A density. Comparison of [^{11}C]UCB-J binding in healthy individuals following 3-5 weeks of intervention with escitalopram ($n = 17$) or placebo ($n = 12$). [^{11}C]UCB-J total volume of distribution (V_T) quantified using the 1TCM ($n = 29$).

Fig. 2 Time-dependent effects of escitalopram on SV2A density. Relationship between [^{11}C]UCB-J binding (V_T) and the duration of the intervention for the placebo group ($n = 12$) and the escitalopram group ($n = 17$) in the neocortex (**A**) and the hippocampus (**B**). The shaded grey area represents the 95% CI.

and IQ as covariates did not reveal any effect of s-escitalopram (Table S4).

Exploratory analyses

Effects of escitalopram on hippocampus volume. The mean (SD) hippocampus volume was 4572 (389) mm^3 in the escitalopram group versus 4767 (329) mm^3 in the placebo group. When compared using a linear regression model controlling for age, sex, and intracranial volume the estimated difference was reduced to -97 mm^3 ($p = 0.33$, Table S5). We further tested if there wa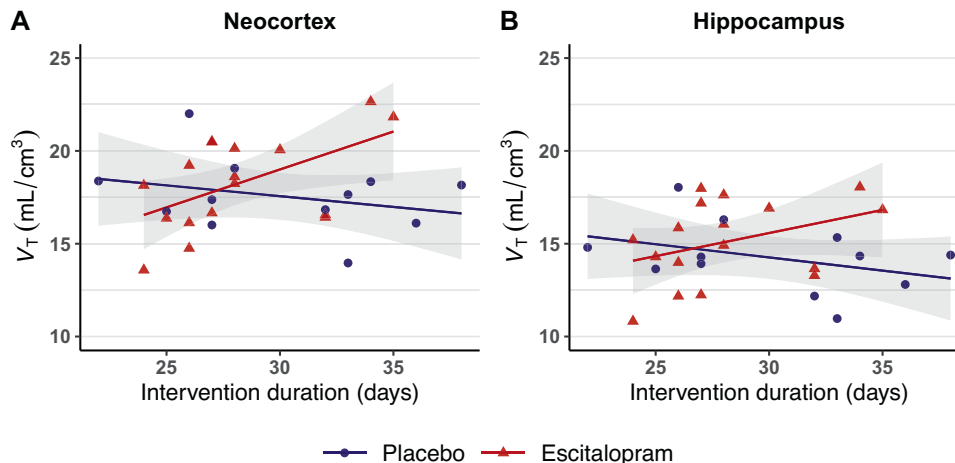s an effect of escitalopram intervention duration, but a model including the *group-by-intervention duration* interaction term did not improve the model fit compared to a nested model, as compared using a likelihood-ratio test ($p = 0.62$). The effect of s-escitalopram concentration on hippocampus volume was estimated to be -22 mm^3 per log[ng/L] of escitalopram ($p = 0.34$). All model estimates are listed in Table S5.

Effects of escitalopram on cortical thickness. Linear regression models with age and sex as covariates showed no difference in cortical thickness between the escitalopram group compared to the placebo group for the neocortical subregions (minimum $p = 0.22$, $p_{adj.} = 1.0$). Estimates for individual regions are listed in Table S6. Likelihood-ratio tests between linear regression models including a *group-by-intervention duration* interaction term and nested models where the group term was excluded, did not support a time-dependent effect of escitalopram on cortical thickness in any of the subregions after correcting for multiple comparisons (minimum $p = 0.033$, $p_{adj.} = 0.16$). Individual estimates are listed in Table S7. Lastly, s-escitalopram concentration also was not associated with cortical thickness (minimum $p = 0.19$, $p_{adj.} = 0.98$) (Table S8).

DISCUSSION

In this study, we examine the effects of the SSRI escitalopram on brain synaptic density in SSRI-naïve healthy volunteers, as indexed by SV2A density measured with [11C]UCB-J PET. Administrating the drug to healthy participants allowed us to study potential effects on synaptic plasticity in the absence of clinical symptoms or brain pathology. The mean [11C]UCB-J V_Ts were not statistically significantly higher in the escitalopram group, and thus the group analysis did not support our primary hypothesis that [11C]UCB-J binding would be higher in the escitalopram group than the placebo group following 3–5 weeks of drug intervention. When adjusting for differences in the length of the intervention period within the escitalopram group, we found a time-dependent effect of escitalopram intervention on [11C]UCB-J V_T, an effect that was more pronounced for the neocortex than the hippocampus. The time-dependent effect of escitalopram was reflected in the linear regression models estimating higher [11C]UCB-J V_T with increasing number of days of escitalopram intervention.

This positive association with escitalopram intervention duration suggests that a reason why we do not find a group difference in the primary analysis could be that an average of 28 days of escitalopram intervention is too short for synaptic effects to fully emerge. Delayed effects of the escitalopram intervention align with the clinical observations that when SSRIs are used for treating, e.g., depression, at least 2–4 weeks of treatment is required before effects on symptoms can be expected [29–31]. As our participants were healthy and relatively young and without cognitive impairments or a history of neuropsychiatric illness, it is also plausible that synaptic wiring, hippocampus volume, and cortical thickness, on which we saw no effect of escitalopram, are less affected by SSRIs. Effects sizes and temporal dynamics might be different in patients, as data from a recent [11C]UCB-J PET study by Holmes et al. [20] suggest that patients with depression have synaptic deficits that correlate with symptom severity. If replicated, it would be interesting to examine whether SSRI

treatment normalizes SV2A levels and if such normalization is associated with clinical improvement.

The reason for the delay in symptom relief following the initiation of SSRI treatment is unclear, although both biological and neuropsychological hypotheses have been proposed, e.g., affective bias and reward sensitivity [11, 12, 27, 46]. Even though inhibition of the serotonin transporter occurs immediately after SSRI dosing [47], the net effect on synaptic serotonin levels is more dynamic. To the best of our knowledge, there is currently no in vivo method available for directly measuring serotonin levels in the human brain after weeks of SSRI intervention. A meta-analysis investigating the temporal effect of SSRIs on brain serotonin levels in rats found an initial dip in the frontal cortex followed by a linear increase over three weeks, in contrast to the hippocampus, where a marked increase was found on day 3 followed by a modest increase from day 6–21 [48]. Our data similarly estimate a larger average effect size for escitalopram in the hippocampus compared to the neocortex, but weaker association with intervention duration. The downstream effects of SSRIs on synaptic structures might be even further delayed and depend on the regional level of serotonergic innervation. One example of this was found in the rat hippocampus in response to the SSRI fluoxetine; in the subregion CA1, synaptic density was equally elevated following 5 and 14 days of intervention, whereas in the subregion CA3, the increase in synaptic density was significantly higher after 14 days than after 5 days of intervention [49] SSRI.

Aside from the intervention duration, the drug dose is also an important aspect to consider. Despite substantial variation in drug concentration, we saw no association between [11C]UCB-J V_T estimates and s-escitalopram concentration. This could be because we used a high daily dose of 20 mg escitalopram, which we expected to lead to a near-maximum occupancy of 70–80% of the serotonin transporter [47]. However, concentrations beyond the point of saturation of the serotonin transporter may be important for the engagement of low-affinity targets. Escitalopram is considered the most selective of the SSRIs [50], but could have important off-target effects according to a recent study: An allosteric binding site at the tropomyosin receptor kinase B (Trk-B) was identified as a low-affinity target of drugs representing several classes of antidepressants, including the SSRIs [51]. The Trk-B receptor activates neurotrophic signalling cascades when activated by brain-derived neurotrophic factor (BDNF). BDNF is known to have antidepressant effects and is increased in response to SSRIs, which forms a strong link between SSRIs and neuroplasticity [14]. It remains to be determined whether all SSRIs, including escitalopram, exert positive allosteric modulation of the Trk-B receptor at clinically relevant doses. This will be important for mapping out the mechanisms of SSRIs and could be a potential target for dual-action drugs promoting neuroplasticity. In this context, evaluating synaptic markers such as SV2A may prove to be a valuable tool.

Few other studies have investigated the effect of drug interventions on SV2A quantified with radioligand techniques. Using [3H]UCB-J in vitro autoradiography, we recently showed that a single administration of the 5-HT$_{2A}$ receptor agonist psilocybin was associated with higher hippocampal SV2A levels in awake pigs 24 h after administration [52]. In contrast, another study found no effect of ketamine on SV2A binding in healthy individuals measured with [11C]UCB-J PET 24 h after the drug intervention [23].

So far, most other SV2A PET imaging studies have been cross-sectional case-control studies of neurodegenerative and psychiatric disorders for which causal relationships cannot be determined. Yet, indications of how modifiable SV2A is in the human brain may potentially be derived indirectly: A study on SV2A binding in cocaine-use disorder by Angarita et al. [53] found a negative correlation between [11C]UCB-J binding and duration of cocaine abstinence, whereas years of lifetime use was unrelated to SV2A binding. In contrast, another study found no association with the frequency of cannabis use in participants with cannabis use disorder [54].

Although exploratory, such analyses can indicate to which extent SV2A is a modifiable state marker or a stable trait marker of synapses.

Some methodological aspects of the current study should be considered. First, the use of SV2A as a proxy for pre-synaptic density. Although SV2A is ubiquitously expressed throughout the brain, it cannot be excluded that SSRI induced changes (or lack thereof) in SV2A binding estimates could have several different causes, such as a number of vesicles per synapse or differential effects on excitatory and inhibitory synapses. Preclinical studies comparing in vivo SV2A PET imaging with in vitro methods will help advance our understanding and interpretations of SV2A imaging studies.

Second, we chose V_T a priori as our primary outcome. The non-displaceable binding potential is often a preferred outcome for radioligands for which a reference region exist. However, the white matter, which has been proposed as a reference region for [11C]UCB-J, is known to contain some amounts of SV2A and overestimate the non-displaceable compartment [43, 44, 55]. Further, given that the centrum semiovale had the second highest estimated effect size (Cohen's d of 0.51) and that we saw an effect of intervention duration for the centrum semiovale, we cannot exclude that the SSRI intervention could have an effect on the specific binding in the white matter, e.g. due to increased axonal transport of newly synthesized synaptic vesicle precursors [56]. The use of V_Ts also make our results more easily comparable to other [11C]UCB-J PET studies on related topics [20–23, 53, 57, 58].

Third, as our study did not include baseline [11C]UCB-J PET scans, we make an assumption of no group differences in cerebral SV2A binding before the intervention was initiated; this assumption is justified on the basis of balanced group randomization that took age and sex into account. The present study design also eliminates issues of long-term test-retest bias which has been reported to occur with [11C]UCB-J PET in some instances [59].

Finally, the sample size was targeted to detect larger effect sizes, which limits us in detecting subtler differences and subgroup differences (e.g., sex). As such, the study should be replicated in an independent sample, ideally with a longer range in the intervention period and in more subjects, to confirm the results and map the temporal dynamics more closely.

In summary, this is the first study to investigate the effect of an SSRI intervention, using clinically relevant doses and duration (i.e., 3–5 weeks), on pre-synaptic density in the human brain. Whereas we find no statistically significant group difference in SV2A, our secondary analyses suggest that escitalopram has a time-dependent effect on cerebral SV2A, i.e., that over 3–5 weeks, escitalopram induces synaptic neuroplasticity in the human brain. This offers a biological explanation for the delayed response commonly observed in patients treated with SSRIs. While replication of the findings is warranted, these results have important implications for future studies investigating the effects of SSRIs, especially concerning the duration of intervention studies. As such, our study adds a novel perspective to the growing literature on synaptic alterations in neuropsychiatric conditions.

DATA AVAILABILITY
Upon completion of the study, all data will be uploaded to the existing CIMBI Database [60]. Researchers may apply for access to the data.

CODE AVAILABILITY
The code generated and used in the production of this manuscript is available from the corresponding authors upon request.

REFERENCES

1. Gabriel FC, Melo DOD, Fráguas R, Leite-Santos NC, Silva RAMda, Ribeiro E. Pharmacological treatment of depression: a systematic review comparing clinical practice guideline recommendations. Plos One. 2020;15:e0231700.
2. Branchi I. The double edged sword of neural plasticity: increasing serotonin levels leads to both greater vulnerability to depression and improved capacity to recover. Psychoneuroendocrino. 2011;36:339–51.
3. Gaspar P, Cases O, Maroteaux L. The developmental role of serotonin: news from mouse molecular genetics. Nat Rev Neurosci. 2003;4:1002–12.
4. Salvan P, Fonseca M, Winkler AM, Beauchamp A, Lerch JP, Johansen-Berg H. Serotonin regulation of behavior via large-scale neuromodulation of serotonin receptor networks. Nat Neurosci. 2023;26:53–63.
5. Kraus C, Castrén E, Kasper S, Lanzenberger R. Serotonin and neuroplasticity – Links between molecular, functional and structural pathophysiology in depression. Neurosci Biobehav Rev. 2017;77:317–26.
6. Duman RS, Aghajanian GK. Synaptic dysfunction in depression: potential therapeutic targets. Science. 2012;338:68–72.
7. Østergaard SD, Jensen SOW, Bech P. The heterogeneity of the depressive syndrome: when numbers get serious. Acta Psychiatr Scand. 2011;124:495–6.
8. Rush AJ, Trivedi MH, Wisniewski SR, Nierenberg AA, Stewart JW, Warden D, et al. Acute and longer-term outcomes in depressed outpatients requiring one or several treatment steps: a STAR*D report. Am J Psychiat. 2006;163:1905–17.
9. Jensen KHR, Dam VH, Ganz M, Fisher PM, Ip C-T, Sankar A, et al. Deep phenotyping towards precision psychiatry of first-episode depression — the Brain Drugs-Depression cohort. BMC Psychiatry. 2023;23:151.
10. Pittenger C, Duman RS. Stress, depression, and neuroplasticity: a convergence of mechanisms. Neuropsychopharmacol. 2008;33:88–109.
11. Clark L, Chamberlain SR, Sahakian BJ. Neurocognitive mechanisms in depression: implications for treatment. Neuroscience. 2009;32:57–74.
12. Roiser JP, Elliott R, Sahakian BJ. Cognitive mechanisms of treatment in depression. Neuropsychopharmacol. 2012;37:117–36.
13. Vetencourt JFM, Sale A, Viegi A, Baroncelli L, Pasquale RD, O'Leary OF, et al. The antidepressant fluoxetine restores plasticity in the adult visual cortex. Science 2008;320:385–8.
14. Castrén E, Antila H. Neuronal plasticity and neurotrophic factors in drug responses. Mol Psychiatr. 2017;22:1085–95.
15. Malik J, Stemplewski R, Maciaszek J. The effect of juggling as dual-task activity on human neuroplasticity: a systematic review. Int J Environ Res Pu. 2022;19:7102.
16. Finnema SJ, Nabulsi NB, Eid T, Detyniecki K, Lin S, Chen M-K, et al. Imaging synaptic density in the living human brain. Sci Transl Med. 2016;8:348ra96.
17. Chen M-K, Mecca AP, Naganawa M, Finnema SJ, Toyonaga T, Lin S, et al. Assessing synaptic density in alzheimer disease with synaptic vesicle glycoprotein 2a positron emission tomographic imaging. Jama Neurol. 2018;75:1215.
18. Mecca AP, O'Dell RS, Chen M, Naganawa M, Toyonaga T, Godek TA, et al. In vivo measurement of widespread synaptic loss and associated tau accumulation in early Alzheimer's disease. Alzheimer's Dement. 2020;16:e037791.
19. Mecca AP, O'Dell RS, Sharp ES, Banks ER, Bartlett HH, Zhao W, et al. Synaptic density and cognitive performance in Alzheimer's disease: A PET imaging study with [11C]UCB-J. Alzheimer's Dement. 2022;18:2527–36.
20. Holmes SE, Scheinost D, Finnema SJ, Naganawa M, Davis MT, DellaGioia N, et al. Lower synaptic density is associated with depression severity and network alterations. Nat Commun. 2019;10:1529.
21. Onwordi EC, Halff EF, Whitehurst T, Mansur A, Cotel M-C, Wells L, et al. Synaptic density marker SV2A is reduced in schizophrenia patients and unaffected by antipsychotics in rats. Nat Commun. 2020;11:246.
22. Radhakrishnan R, Skosnik PD, Ranganathan M, Naganawa M, Toyonaga T, Finnema S, et al. In vivo evidence of lower synaptic vesicle density in schizophrenia. Mol Psychiatr. 2021;26:7690–8.
23. Holmes SE, Finnema SJ, Naganawa M, DellaGioia N, Holden D, Fowles K, et al. Imaging the effect of ketamine on synaptic density (SV2A) in the living brain. Mol Psychiatr. 2022;27:2273–81.
24. Kishimoto T, Chawla JM, Hagi K, Zarate CA, Kane JM, Bauer M, et al. Single-dose infusion ketamine and non-ketamine N-methyl-d-aspartate receptor antagonists for unipolar and bipolar depression: a meta-analysis of efficacy, safety and time trajectories. Psychol Med. 2016;46:1459–72.
25. Harmer CJ, Bhagwagar Z, Perrett DI, Völlm BA, Cowen PJ, Goodwin GM. Acute SSRI administration affects the processing of social cues in healthy volunteers. Neuropsychopharmacol. 2003;28:148–52.
26. Skandali N, Rowe JB, Voon V, Deakin JB, Cardinal RN, Cormack F, et al. Dissociable effects of acute SSRI (escitalopram) on executive, learning and emotional functions in healthy humans. Neuropsychopharmacol. 2018;43:2645–51.
27. Michely J, Eldar E, Martin IM, Dolan RJ. A mechanistic account of serotonin's impact on mood. Nat Commun. 2020;11:2335.
28. Lepola UM, Loft H, Reines EH. Escitalopram (10–20 mg/day) is effective and well tolerated in a placebo-controlled study in depression in primary care. Int Clin Psychopharm. 2003;18:211–7.
29. Kasper S, Spadone C, Verpillat P, Angst J. Onset of action of escitalopram compared with other antidepressants: results of a pooled analysis. Int Clin Psychopharm. 2006;21:105–10.

30. Gelenberg AJ, Freeman MP, Markowitz JC, Rosenbaum JF, Thase ME, Trivedi MH, et al. Practice guideline for the treatment of patients with major depressive disorder. American Psychiatric Association. 2010. 3rd ed. https://psychiatryonline.org/pb/assets/raw/sitewide/practice_guidelines/guidelines/mdd.pdf. Accessed Sep 6, 2022.

31. Taylor MJ, Freemantle N, Geddes JR, Bhagwagar Z. Early onset of selective serotonin reuptake inhibitor antidepressant action: systematic review and meta-analysis. Arch Gen Psychiat. 2006;63:1217–23.

32. Dam VH, Stenbæk DS, Köhler-Forsberg K, Ip C, Ozenne B, Sahakian BJ, et al. Evaluating cognitive disturbances as treatment target and predictor of antidepressant action in major depressive disorder: a NeuroPharm study. Transl Psychiat. 2022;12:468.

33. Langley C, Armand S, Luo Q, Savulich G, Segerberg T, Søndergaard A, et al. Chronic escitalopram in healthy volunteers has specific effects on reinforcement sensitivity: a double-blind, placebo-controlled semi-randomised study. Neuropsychopharmacol. 2023;48:664–70.

34. Reynolds CR, Kamphaus RW. Introduction to the Reynolds Intellectual Assessment Scales and the Reynolds Intellectual Screening Test. Contemporary intellectual assessment: theories, tests, and issues., New York, NY, US: The Guilford Press; 2005. p. 461–83.

35. Finnema SJ, Nabulsi NB, Mercier J, Lin S, Chen M-K, Matuskey D, et al. Kinetic evaluation and test–retest reproducibility of [11C]UCB-J, a novel radioligand for positron emission tomography imaging of synaptic vesicle glycoprotein 2A in humans. J Cereb Blood Flow Metab. 2017;38:2041–52.

36. Fischl B. FreeSurfer. Neuroimage 2012;62:774–81.

37. Nabulsi NB, Mercier J, Holden D, Carré S, Najafzadeh S, Vandergeten M-C, et al. Synthesis and preclinical evaluation of 11C-UCB-J as a PET tracer for imaging the synaptic vesicle glycoprotein 2A in the brain. J Nucl Med. 2016;57:777–84.

38. Hong IK, Chung ST, Kim HK, Kim YB, Son YD, Cho ZH. Ultra fast symmetry and SIMD-based projection-backprojection (SSP) algorithm for 3-D PET image reconstruction. IEEE Trans Med Imaging. 2007;26:789–803.

39. Sureau FC, Reader AJ, Comtat C, Leroy C, Ribeiro M-J, Buvat I, et al. Impact of image-space resolution modeling for studies with the high-resolution research tomograph. J Nucl Med. 2008;49:1000–8.

40. Keller SH, Svarer C, Sibomana M. Attenuation correction for the HRRT PET-scanner using transmission scatter correction and total variation regularization. IEEE Trans Med Imaging. 2013;32:1611–21.

41. Svarer C, Madsen K, Hasselbalch SG, Pinborg LH, Haugbøl S, Frøkjær VG, et al. MR-based automatic delineation of volumes of interest in human brain PET images using probability maps. Neuroimage 2005;24:969–79.

42. Tjerkaski J, Cervenka S, Farde L, Matheson GJ. Kinfitr — an open-source tool for reproducible PET modelling: validation and evaluation of test-retest reliability. EJNMMI Res. 2020;10:77.

43. Rossano S, Toyonaga T, Finnema SJ, Naganawa M, Lu Y, Nabulsi N, et al. Assessment of a white matter reference region for 11C-UCB-J PET quantification. J Cereb Blood Flow Metab.2019;40:1890–901.

44. Finnema SJ, Rossano S, Naganawa M, Henry S, Gao H, Pracitto R, et al. A single-center, open-label positron emission tomography study to evaluate brivaracetam and levetiracetam synaptic vesicle glycoprotein 2A binding in healthy volunteers. Epilepsia. 2019;60:958–67.

45. Lipsitz SR, Leong T, Ibrahim J, Lipshultz S. A partial correlation coefficient and coefficient of determination for multivariate normal repeated measures data. J R Stat Soc: Ser D (Stat). 2001;50:87–95.

46. Harmer CJ, Duman RS, Cowen PJ. How do antidepressants work? New perspectives for refining future treatment approaches. Lancet Psychiatry. 2017;4:409–18.

47. Sørensen A, Ruhé HG, Munkholm K. The relationship between dose and serotonin transporter occupancy of antidepressants—a systematic review. Mol Psychiatr. 2022;27:192–201.

48. Fritze S, Spanagel R, Noori HR. Adaptive dynamics of the 5-HT systems following chronic administration of selective serotonin reuptake inhibitors: a meta-analysis. J Neurochem. 2017;142:747–55.

49. Hajszan T, MacLusky NJ, Leranth C. Short-term treatment with the antidepressant fluoxetine triggers pyramidal dendritic spine synapse formation in rat hippocampus. Eur J Neurosci. 2005;21:1299–303.

50. Zhong H, Haddjeri N. Sánchez C. Escitalopram, an antidepressant with an allosteric effect at the serotonin transporter—a review of current understanding of its mechanism of action. Psychopharmacology. 2012;219:1–13.

51. Casarotto PC, Girych M, Fred SM, Kovaleva V, Moliner R, Enkavi G, et al. Antidepressant drugs act by directly binding to TRKB neurotrophin receptors. Cell 2021;184:1299–1313.e19.

52. Raval NR, Johansen A, Donovan LL, Ros NF, Ozenne B, Hansen HD, et al. A single dose of psilocybin increases synaptic density and decreases 5-HT2A receptor density in the pig brain. Int J Mol Sci. 2021;22:835.

53. Angarita GA, Worhunsky PD, Naganawa M, Toyonaga T, Nabulsi NB, Li CR, et al. Lower prefrontal cortical synaptic vesicle binding in cocaine use disorder: An exploratory 11C-UCB-J positron emission tomography study in humans. Addict Biol. 2022;27:e13123.

54. D'Souza DC, Radhakrishnan R, Naganawa M, Ganesh S, Nabulsi N, Najafzadeh S, et al. Preliminary in vivo evidence of lower hippocampal synaptic density in cannabis use disorder. Mol Psychiatr. 2021;26:3192–3200.

55. Varnäs K, Stepanov V, Halldin C. Autoradiographic mapping of synaptic vesicle glycoprotein 2A in non-human primate and human brain. Synapse. 2020;74:e22157.

56. Guedes-Dias P, Holzbaur ELF. Axonal transport: driving synaptic function. Science. 2019;366:eaaw9997.

57. Fang XT, Toyonaga T, Hillmer AT, Matuskey D, Holmes SE, Radhakrishnan R, et al. Identifying brain networks in synaptic density PET (11C-UCB-J) with independent component analysis. Neuroimage. 2021;237:118167.

58. Fang XT, Volpi T, Holmes SE, Esterlis I, Carson RE, Worhunsky PD. Linking resting-state network fluctuations with systems of coherent synaptic density: a multi-modal fMRI and 11C-UCB-J PET study. Front Hum Neurosci. 2023;17:1124254.

59. Tuncel H, Boellaard R, Coomans EM, Vries EFde, Glaudemans AW, Feltes PK, et al. Kinetics and 28-day test–retest repeatability and reproducibility of [11C]UCB-J PET brain imaging. J Cereb Blood Metab. 2020;41:1338–50.

60. Knudsen GM, Jensen PS, Erritzoe D, Baaré WFC, Ettrup A, Fisher PM, et al. The center for integrated molecular brain imaging (Cimbi) database. NeuroImage. 2016;124:1213–9.

AUTHOR CONTRIBUTIONS
GMK and BJS conceptualized the study and designed the main study together with CL and DSS. BJS and GMK acquired funding for the study. AJ designed the PET experiments and data processing pipeline with input from CS, PPS, GMK, and SHK. SA was responsible for recruitment and MRI acquisition. AJ acquired the PET data with assistance from AN, KM, and AV. INP and JM were responsible for radiochemistry. VB was responsible for the processing of volumetric MRI data. AJ analyzed the data with assistance from PPS, GMK, BO, CS, SHK, and VB. AJ drafted the manuscript in consultation with GMK. All authors critically reviewed the manuscript.

COMPETING INTERESTS
GMK has received honoraria as a speaker for Sage Biogen and H. Lundbeck, and is a consultant for Onsero, Pangea, and Gilgamesh, Abbvie, PureTechHealth. BJS consults for Cambridge Cognition and receives technology transfer fees from PopReach via Cambridge Enterprise. All other authors declare no competing interests. Funding agencies did not impact the study and played no role in manuscript preparation and submission.

ADDITIONAL INFORMATION
Supplementary information The online version contains supplementary material available at https://doi.org/10.1038/s41380-023-02285-8.

Correspondence and requests for materials should be addressed to Gitte M. Knudsen.

Reprints and permission information is available at http://www.nature.com/reprints

Publisher's note Springer Nature remains neutral with regard to jurisdictional claims in published maps and institutional affiliations.

Supplementary material

Effects of escitalopram on synaptic density in the healthy human brain: A randomized controlled trial

Contents

In / exclusion criteria

Inclusion criteria:

1. Healthy females and males aged 18-45 years.

Exclusion criteria:

1. Current or former primary psychiatric disorder (DSM-V or WHO ICD-11 diagnostic classification).
2. Current or previous neurological disease, severe somatic disease, or the consumption of drugs likely to influence the test results.
3. Current psychoactive medication.
4. Abnormal ECG.
5. Postural orthostatic tachycardia syndrome.
6. Hypotension (blood pressure < 100/70 mmHg) or hypertension (blood pressure > 140/90 mmHg).
7. Head injury or concussion resulting in loss of consciousness for more than 2 min.
8. Pregnancy.
9. Lactation.
10. Alcohol or drug abuse.
11. Nicotine addiction.
12. Recreational drug use other than tobacco and alcohol within the last 30 days.
13. Cannabis use > 50 x lifetime.
14. Recreational drug use > 10 x lifetime (for each substance).
15. Non-fluent in Danish or pronounced visual or auditory impairments.
16. Current or past learning disability.
17. Severe physical impairments affecting eyesight or motor performance.
18. Participation in experiments with radioactivity (>10 mSv) within the last year or other significant exposure to radioactivity.
19. Contraindications for magnetic resonance imaging (MRI).
20. Allergy to compounds used for PET scan or intervention.

Figure S1: Study design
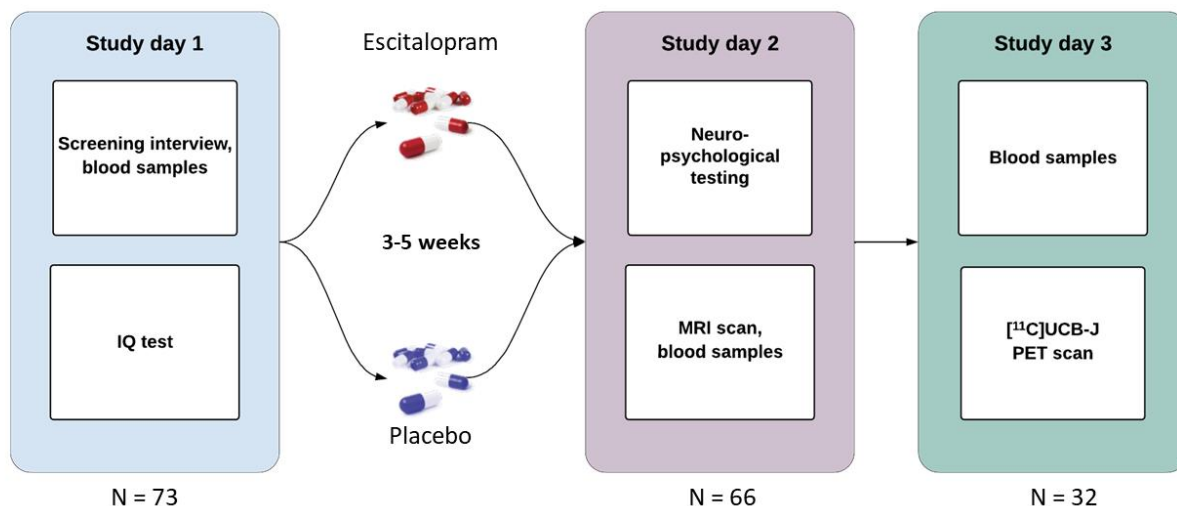
Figure S1: Study design. Participants were screened and randomized on Study day 1. Within 1-5 days, participants started the intervention with either escitalopram or placebo capsules. After 3-5 weeks of full dose intervention, participants came back for MRI scan and neuropsychological testing on Study day 2 and PET scan on Study day 3.

Radiosynthesis of [^{11}C]UCB-J

Proton irradiation of the target material (nitrogen-14 gas) was performed using the cyclotron: Scanditronix MC-32 with aluminium high-pressure gas target. Irradiations for carbon-11 were performed at 16 MeV. The target gas used was 10% hydrogen in nitrogen. Following irradiation, the target gas was transferred to the radiochemistry system (Scansys Aps) through stainless steel capillaries. [^{11}C]methyl iodide was synthesized from [^{11}C]methane by a standard circulation procedure.

Preparation of the precursor: The precursor (1.5 mg) was dissolved in MeOH (70 µL) and 1 M HCl (15 µL) was added. The resulting mixture reacted overnight at room temperature. On the day of synthesis, the liquid was removed by a stream of nitrogen to complete dryness.

Preparation of the labelling mixture: 4-5 mg P(o-tolyl)$_3$ was dissolved in DMF 1.8 mL) and H$_2$O (0.2 mL) in a capped vial and degassed with nitrogen. Pd$_2$dba$_3$ (4-5 mg) was weighed out in a capped vial and flushed with nitrogen. Immediately before labelling, the P-(o-tolyl)$_3$ solution was added to the Pd$_2$dba$_3$. From here, 350 µL was withdrawn and added to a 0.9 mL vial containing 0.5 M K$_2$CO$_3$ (20 µL). The formed [^{11}C]methyl iodide was trapped in the 0.9 mL glass vial containing the K$_2$CO$_3$/ P(o-tolyl)$_3$/Pd$_2$dba$_3$ mixture. After trapping the [^{11}C]methyl iodide, the hydrolyzed DM-BF$_3$-UCB-J precursor was re-dissolved in DMF (150 uL) and reacted with the mixture by heating at 100 °C for 300 seconds to give [^{11}C]UCB-J. The reaction mixture was diluted with 4 mL 0.1% H3PO4 and automatically injected onto a preparative HPLC-column (Onyx™ Monolithic C-18, 100 × 10 mm equipped with a SecurityGuard Cartridge Lux Cellulose-4, 4 x 3.0 mm; flow: 6 mL/min; eluent: 13/87 [ethanol (96%)/0.1 M phosphoric acid]). The radioactive fraction corresponding to the radiolabeled product

(retention time (rt) app. 300 s) was collected by diverting the flow from the column outlet through a 0.22 μm sterile filter and directly into a sterile stoppered and a capped vial containing phosphate buffer (9 mL, pH 7). The identity and molar activity of the product was determined by using a C-18 column (Kinetex 2.6 um, C18, 100Å, 50 x 4.6 mm, Phenomenex) eluted with 67% 25 mM citrate buffer (pH 5.4)/33% acetonitrile ; injection volume 50 μL; flow rate 1.5 mL/min; on-line UV (261 nm) and radioactivity detection. Rt UCB-J 2.1 min.

Radiometabolite analysis

For measurement of intact tracer and radiolabeled metabolites, plasma samples up until 90 min were filtered through a 0.45 μm syringe filter (Whatman GD/X 13 mm, Cytiva, Buckinghamshire, UK) and subsequently diluted 1:1 with 20 mM disodium hydrogen phosphate and 5 mM sodium-1-decanesulfonate pH 7.2 with 2% isopropanol. Samples were analyzed in a fully automated column-switching HPLC system (UltiMate 3000, Thermo Fisher Scientific, Hvidovre, Denmark) connected to a radio-HPLC detector (PosiRam Model 2, LabLogic Systems, Sheffield, UK)(Gillings, 2009). The HPLC system was equipped with a small extraction column (Shimpack MAYI-ODS 30x4.6 mm, Shimadzu, Ballerup, Denmark) combined with an analytical column (Onyx Monolithic C18 50x4.6 mm, Phenomenex, Brønshøj, Denmark). For extraction and elution, the mobile phase consisted of 100% 20 mM disodium hydrogen phosphate and 5 mM sodium-1-decanesulfonate pH 7.2 with 2% isopropanol and 59% 100 mM sodium dihydrogen phosphate and 2 mM sodium-1-decanesulfonate pH 2.6 and 41% methanol, respectively. Samples were injected in a volume of 4 mL, and the analysis was run at a flow of 5 mL/min at 25 °C. The total runtime for each sample was 8.55 min with a 4 min extraction step, 4 min elution step and 0.55 min of equilibration. Four eluate fractions were collected in 2 min intervals, and radioactivity was subsequently measured using a gamma counter (Wizard 2480, Perkin Elmer, Wallac Oy, Turku, Finland). The parent tracer fraction was calculated as follows: % parent fraction = (radioactivity of parent eluate/total amount of collected radioactivity) x 100%.

Free fraction measurement

[^{11}C]UCB-J free fraction was measured in the following way: plasma spiked with 1 μL/mL of tracer was added into one dialysis chamber (500 μL chambers, Harvard Apparatus, Holliston, MA, USA) and dialyzed against an equal volume of phosphate-buffered saline through a cellulose membrane (MWCO 10,000 Dalton, Harvard Apparatus, Holliston, USA). The system was incubated at 37 ºC for 30, 60, 120, 150 and 180 min. After completion of dialysis, samples were extracted and analyzed for radioactivity using the Cobra II gamma counter (Packard Instrument Company, Meriden, USA). The ratio of buffer:plasma radioactivity was plotted over time and fitted according to eq. 1 with a fixed average value of the diffusion coefficient (k_D), using GraphPad Prism (v. 9.0, GraphPad Software, San Diego, CA, USA) to determine f_{Peq}.

$$f_P(t) = \frac{f_{Peq} \times t}{k_D + t} \quad \text{(eq. 1)}$$

[^{11}C]UCB-J plasma free fraction did not differ between intervention groups or sexes, but correlated with age (β_{esc} = 0.01, p = 0.52; β_{male} = -0.003, p = 0.85; β_{age} = -0.005 /year, p = 0.005). The effect of age was slightly reduced and not statistically significant when omitting one age-outlier of 41.9 years (β_{age} = -0.004, p = 0.1). As there was no group difference nor association between [^{11}C]UCB-J V_T estimates and f_P in the neocortex (βf_P = 7.0 mL/cm^3, p = 0.50), it was not used in the analyses.

1TCM V_T estimates for additional ROIs

Table S1

Region	Placebo (N=12)	Escitalopram (N=17)	p	Cohen's *d*
Neocortex	17.55 (1.96)	18.25 (2.51)	0.41	0.31
Hippocampus	14.25 (1.85)	15.12 (2.21)	0.26	0.43
Caudate	20.23 (2.31)	21.83 (3.63)	0.16	0.53
Centrum semiovale	3.85 (0.53)	4.14 (0.61)	0.18	0.51
Insula	18.21 (2.05)	19.38 (2.64)	0.19	0.50
Putamen	20.52 (2.25)	21.77 (3.02)	0.21	0.47
Orbitofrontal ctx	17.78 (2.16)	18.85 (2.94)	0.27	0.41
Entorhinal ctx	14.05 (2.70)	15.19 (2.82)	0.28	0.41
Med inf temp gyrus	17.97 (1.93)	18.90 (2.70)	0.29	0.39
Amygdala	16.66 (2.18)	17.60 (2.75)	0.31	0.38
ACC	18.67 (2.28)	19.65 (2.94)	0.32	0.37
Sup frontal gyrus	16.96 (2.08)	17.81 (2.61)	0.34	0.36
vlPFC	17.95 (2.07)	18.83 (2.75)	0.34	0.36
dlPFC	17.69 (2.14)	18.49 (2.59)	0.37	0.34
Sensory-motor ctx	16.21 (2.02)	16.93 (2.30)	0.38	0.33
Temporal ctx	18.36 (1.97)	19.12 (2.60)	0.38	0.33
Parietal ctx	17.77 (2.09)	18.42 (2.53)	0.45	0.28
Cerebellum (excl. vermis)	13.93 (1.57)	14.41 (1.93)	0.47	0.27
Thalamus	17.35 (2.15)	17.91 (2.41)	0.51	0.25
Sup temp gyrus	18.84 (2.04)	19.42 (2.50)	0.50	0.25
Raphe nuclei	10.98 (1.52)	11.13 (1.25)	0.78	0.11
Occipital ctx	17.50 (1.94)	17.67 (2.39)	0.84	0.08
PCC	18.26 (1.81)	18.40 (2.33)	0.86	0.07

Figure S2: BP_{ND} estimates from the SRTM2 in primary ROIs
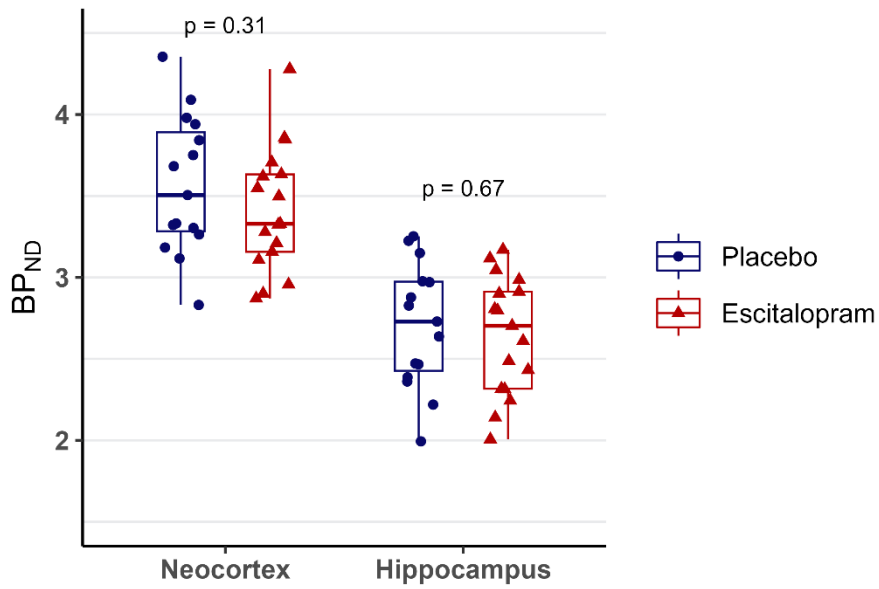
Figure S2. Group comparison of BP_{ND} estimates.

Effects on [^{11}C]UCB-J V_T

Table S2: Effect of intervention group

General linear model with age, sex and IQ as covariates to test group effect on [^{11}C]UCB-J V_T

Predictors	Neocortex			Hippocampus			Centrum semiovale		
	Estimate	SE	p	Estimate	SE	p	Estimate	SE	p
Intercept*	17.01	0.92	**<0.001**	13.75	0.82	**<0.001**	3.83	0.25	**<0.001**
Age (per decade)	0.23	0.84	0.79	0.14	0.76	0.86	0.01	0.23	0.98
Sex (Male)	-1.48	0.85	0.09	-1.29	0.76	0.10	-0.22	0.23	0.35
IQ	0.14	0.06	**0.027**	0.13	0.05	**0.026**	0.02	0.02	0.37
Intervention (escitalopram)	-0.11	0.88	0.90	0.16	0.79	0.84	0.19	0.24	0.43

* Intercept centered at age = 20 years and IQ = 100.

General linear model with age, sex and IQ as covariates to test effect of intervention duration on [¹¹C]UCB-J V_T

Predictors	Neocortex				Hippocampus				Centrum semiovale			
	Estimate	SE	p	r_ρ	Estimate	SE	p	r_ρ	Estimate	SE	p	r_ρ
Intercept*	17.18	0.78	**<0.001**		13.85	0.78	**<0.001**		3.86	0.24	**<0.001**	
Age (per decade)	-0.32	0.74	0.67	-0.09	-0.23	0.74	0.76	-0.07	-0.12	0.22	0.61	-0.11
Sex (Male)	-1.65	0.82	0.056		-1.22	0.82	0.15		-0.21	0.25	0.41	
IQ	0.15	0.05	**0.008**	0.53	0.13	0.05	**0.017**	0.48	0.02	0.02	0.29	0.22
Intervention (escitalopram)	0.32	0.76	0.68		0.42	0.76	0.59		0.28	0.23	0.23	
Duration (placebo)	-0.01	0.13	0.95	-0.01	-0.06	0.13	0.62	-0.1	-0.02	0.04	0.60	-0.11
Duration (escitalopram)	0.47	0.14	**0.003**	0.58	0.30	0.14	**0.048**	0.41	0.10	0.04	**0.029**	0.45

*Intercept centered at age = 20 years, mean intervention duration (29 days), and IQ = 100. R_ρ = partial correlation coefficient.

Table S4: Effects of s-escitalopram

General linear model with age and sex as covariates to test effect of s-escitalopram level on [¹¹C]UCB-J V_T

Predictors	Neocortex			Hippocampus			Centrum semiovale		
	Estimate	SE	p	Estimate	SE	p	Estimate	SE	p
Intercept*	17.03	0.92	**<0.001**	13.80	0.83	**<0.001**	3.85	0.26	**<0.001**
Age (per decade)	0.23	0.83	0.78	0.17	0.75	0.83	0.03	0.23	0.91
Sex (Male)	-1.50	0.86	0.01	-1.31	0.78	0.11	-0.22	0.24	0.36
IQ	0.14	0.06	**0.028**	0.13	0.06	**0.026**	0.02	0.02	0.37
S-escitalopram (log[ng/L])	-0.04	0.20	0.85	0.01	0.18	0.96	0.03	0.06	0.57

* Intercept centered at age = 20 years.

Effects on hippocampus volume

Table S5: Effects of intervention group and s-escitalopram

General linear model with age, sex and intra-cranial volume (ICV) as covariates to test effect of intervention group and s-escitalopram level on hippocampus volume

Predictors	Group			S-escitalopram		
	Estimate	SE	p	Estimate	SE	p
Intercept*	4637	99	**<0.001**	4736	91	**<0.001**
Age (per decade)	68	104	0.52	61	103	0.56
Sex (Male)	-124	117	0.23	-128	117	0.28
ICV (L)	2048	419	**<0.001**	2038	423	**<0.001**
Intervention (Escitalopram)	97	99	0.33			
S-escitalopram (log[ng/L])				-22	23	0.34

Hippocampus volume is in unit of mm^3. * Intercept centered at age = 20 years, and mean ICV.

11

Effects on cortical thickness

Table S6: Effects of intervention group

General linear model with age and sex as covariates to test effect of intervention group cortical thickness

Predictors	Frontal			Parietal			Temporal			Occipital			Insular		
	Estimate	SE	p	Estimate	SE	p	Estimate	SE	p	Estimate	SE	p	Estimate	SE	p
Intercept*	2.77	0.02	**<0.01**	2.52	0.03	**<0.01**	2.90	0.03	**<0.01**	2.02	0.03	**<0.01**	3.16	0.04	**<0.01**
Age (per decade)	-0.07	0.03	**0.02**	-0.05	0.03	0.13	-0.04	0.04	0.32	-0.01	0.03	0.67	-0.05	0.05	0.29
Sex (Male)	0.06	0.03	**0.04**	0.06	0.03	0.07	0.08	0.04	0.06	0.06	0.03	0.07	0.06	0.04	0.17
Intervention (Escitalopram)	0.03	0.03	0.22	0.03	0.03	0.26	0.01	0.04	0.77	0.01	0.03	0.83	-0.00	0.04	0.92

Cortical thickness is in the unit of mm. * Intercept centered at age = 20 years. All escitalopram corrected p-values = 1 (Bonferroni-Holm, 5 tests).

Table S7: Effects of intervention duration

Likelihood-ratio tests of model with *group-by-intervention duration* vs. a nested model without group term. Age and sex included in both models

Frontal			Parietal			Temporal			Occipital			Insular		
χ^2	p	$p_{adj.}$	χ^2	p	$p_{adj.}$	χ^2	p	$p_{adj.}$	χ^2	p	$p_{adj.}$	χ^2	p	$p_{adj.}$
6.72	0.03	0.16	3.1	0.21	0.62	1.60	0.45	0.90	6.84	0.03	0.16	1.00	0.61	0.90

($p_{adj.}$ = Bonferroni-Holm, 5 tests).

Table S8: Effects of s-escitalopram

General linear model with age and sex as covariates to test effect of s-escitalopram on cortical thickness

Predictors	Frontal			Parietal			Temporal			Occipital			Insular		
	Estimate	SE	p	Estimate	SE	p	Estimate	SE	p	Estimate	SE	p	Estimate	SE	p
Intercept*	2.77	0.02	**<0.01**	2.52	0.03	**<0.01**	2.90	0.04	**<0.01**	2.02	0.03	**<0.01**	3.16	0.04	**<0.01**
Age (per decade)	-0.07	0.03	**0.02**	-0.05	0.03	0.15	-0.04	0.04	0.34	-0.01	0.03	0.67	-0.05	0.04	0.28
Sex (Male)	0.06	0.03	**0.03**	0.06	0.03	0.07	0.08	0.04	0.06	0.06	0.03	0.07	0.06	0.04	0.18
S-escitalopram (log[ng/L])	0.01	0.01	0.19	0.01	0.01	0.28	0.00	0.01	0.88	0.00	0.01	0.79	-0.00	0.01	0.97

Cortical thickness is in the unit of mm. * Intercept centered at age = 20 years. All escitalopram corrected p-values = 1 (Bonferroni-Holm, 5 tests).

III

Effects of psilocybin on synaptic plasticity in the human brain

Annette Johansen[1,2], Pontus Plavén-Sigray[1,3], Martin K. Madsen[1,4], Anna Søndergaard[1,2], Catharina Messel[1], Maria Grzywacz, Arafat Nasser[1], Drummond McCulloch[1,2], Vincent Beliveau[1,5], Alexandra Vassilieva[2,6], Anton Lund[2,6], Szabolcs Lehel7, Dea S. Stenbæk[1,8] Patrick M. Fisher[1,9], Claus Svarer[1], Gitte M. Knudsen[1,2]*

1. Neurobiology Research Unit, Rigshospitalet, Copenhagen University Hospital, Copenhagen, Denmark
2. Department of Clinical Medicine, Faculty of Health and Medical Sciences, University of Copenhagen, Copenhagen, Denmark
3. Centre for Psychiatry Research, Department of Clinical Neuroscience, Karolinska Institutet, & Stockholm Health Care Services, Region Stockholm
4. Department of Neurology, Odense University Hospital, Odense, Denmark
5. Department of Neurology, Medical University of Innsbruck, Innsbruck, Austria
6. Department of Neuroanesthesiology, Rigshospitalet, Copenhagen University Hospital, Copenhagen, Denmark
7. PET & Cyclotron Unit, Rigshospitalet, Copenhagen University Hospital, Copenhagen, Denmark
8. Department of Psychology, Faculty of Social Sciences, University of Copenhagen, Copenhagen, Denmark
9. Department of Drug Design and Pharmacology, University of Copenhagen, Copenhagen, Denmark

*Corresponding author:
Gitte Moos Knudsen,
Copenhagen University Hospital, Rigshospitalet, Section 8057,
6-8 Inge Lehmanns Vej,
DK-2100 Copenhagen, Denmark
Ph: +45 3545 6712
E-mail: gmk@nru.dk

Status: In prep.

Abstract

Classical psychedelics like psilocybin are garnering interest as possible treatments for neuropsychiatric disorders. Despite their promise, the underlying mechanism—especially why a single dose can lead to lasting positive effects in both patients and healthy individuals—is yet to be fully understood. While recent preclinical studies suggest that these drugs might enhance neuroplasticity, direct evidence in humans is lacking. This study aimed to investigate the persistent effects of a single psychoactive dose of psilocybin on cerebral SV2A levels, an indicator of synaptic density, in healthy volunteers using $[^{11}C]$UCB-J PET neuroimaging. In a one-arm open-label design, we administered a single dose of 0.3 mg/kg psilocybin to 15 healthy volunteers. $[^{11}C]$UCB-J PET imaging was performed at baseline and one week after the intervention. We examined changes in SV2A density in the hippocampus and frontal cortex and explored links between these changes and the subjective experiences during the intervention session as well as the persisting effects three months later. Our results did not reveal significant changes in cerebral SV2A density one week after psilocybin administration. However, our exploratory analyses hint at potential associations between SV2A changes and subjective experiences. The absence of notable synaptic changes in our healthy cohort highlights the need for investigations in patient populations with neuropsychiatric conditions, where the therapeutic potential of psilocybin may be more evident.

Introduction

The classical psychedelics, e.g., psilocybin or LSD are emerging as potential therapeutics for the treatment of certain neuropsychiatric disorders (Vollenweider and Preller, 2020). Like other psychedelics, psilocybin activates the serotonin 2A receptor (5-HT$_{2A}$R) and when administered in moderate to high doses, this activation acutely induces an altered state of consciousness, perceptual changes, and a diminished sense of self (Vollenweider et al., 1998; Kometer et al., 2012; Quednow et al., 2012; Nichols, 2016; Madsen et al., 2019; Stenbæk et al., 2021; McCulloch et al., 2022). Intake of psychedelics is also associated with long-lasting positive emotional effects in both healthy individuals (MacLean et al., 2011; Smigielski et al., 2019; Madsen et al., 2020; Yaden and Griffiths, 2021; Nautiyal and Yaden, 2023) and patients with MDD, anxiety, and addiction (Carhart-Harris et al., 2016, 2018, 2021; Erritzoe et al., 2018; Roseman et al., 2018; Davis et al., 2021).

Traditional antidepressant drugs acting on the serotonin system such as selective serotonin reuptake inhibitors (SSRI) typically require 2-4 weeks of daily administration before effects can be expected (Kasper et al., 2006; Gelenberg et al., 2010). In contrast, psychedelics are rapid-acting, and current evidence suggests that only 1-2 moderate to high doses leads to substantial relief of depressive symptoms (Carhart-Harris et al., 2016, 2018, 2021; Erritzoe et al., 2018; Roseman et al., 2018; Davis et al., 2021). Positive experiences during the intervention session, such as feelings of bliss and unity with the world, are particularly associated with long-lasting positive effects (Roseman et al., 2018; McCulloch et al., 2022; Søndergaard et al., 2022), but the underlying neurobiological mechanisms have not yet been fully established.

One proposed mechanism of the rapid therapeutic action of psychedelics is that it induces synaptic plasticity (Vos et al., 2021; Olson, 2022; Calder and Hasler, 2023). Structural and functional alterations, such as dendritic sprouting and arborization and upregulation of the presynaptic marker, VGLUT1, occur in cultured neurons as early as 6 hours after 5-HT$_{2A}$R stimulation, with persisting effects detected up to seven days later (Ly et al., 2018, 2021; Shao et al., 2021; Moliner et al., 2023; Vargas et al., 2023). These observations are supported by in vivo studies: Awake pigs that received a single dose of i.v. psilocybin showed higher expression

of the presynaptic marker Synaptic Vesicle glycoprotein 2A (SV2A) density compared to a saline-placebo (Raval et al., 2021). The traditional antidepressive drugs escitalopram has also been associated with synaptic alteration; we recently showed that the longer healthy individuals take the SSRI escitalopram, the higher their cerebral SV2A levels are compared to a placebo group (Johansen et al., 2023a). This observation provides the first *in vivo* link between serotonergic modulation and synaptic plasticity. These findings are particularly interesting, as a recent PET neuroimaging study reported that SV2A density is lower in the hippocampus and frontal cortex in individuals suffering from severe MDD and PTSD (Holmes et al., 2019).

Building on these observations, we aimed to investigate if a single psychoactive dose of psilocybin increases cerebral SV2A levels in healthy individuals, as measured with $[^{11}C]$UCB-J PET neuroimaging. In a one-arm, open-label study, we measured the SV2A density in the hippocampus and frontal cortex in healthy volunteers at baseline and one week after a psilocybin intervention session. We further explored if changes in SV2A density at one week after psilocybin intervention were associated with subjective effects during the intervention or with persisting effects three months after the session.

Methods

i. Participants

Healthy volunteers were recruited from a local database of individuals who had expressed interest in participating in studies involving psilocybin. Upon informed consent, participants underwent extensive screening procedures including somatic and psychiatric medical history, clinical examination, standard blood screening, and ECG.

The study was approved by the Danish Medicines Agency (EudraCT ID: 2016-004000-61, amendments: 2020061833, 2021041519) and by the ethics committee for the Capital region of Denamrk (ID: H-16028698, with amendments). The study was preregistered at ClinicalTrials.gov (NCT03289949).

Baseline neuroimaging data from a subset of participants have been included in a previous study (Johansen et al., 2023b).

ii. Study design and psilocybin intervention

Participants underwent MRI and [^{11}C]UCB-J PET scans at baseline. On a separate day (~7 days later) participants underwent an intervention session with orally administered psilocybin (0.31 mg/kg) guided by trained psychologists in one of two conditions: 1) participants 1-5 completed the intervention while undergoing a series of functional MRI scans in a similar set up as reported by (Madsen et al., 2021); 2) participants 6-15 completed the intervention session in a designated intervention room while listening to music chosen to facilitate the different phases of the psychedelic experience (Messell et al., 2022). In both settings, blood samples were collected from a venous catheter during the intervention to measure plasma psilocin levels (PPL). One week later, participants returned for follow-up [^{11}C]UCB-J PET and MRI scans.

Psychological questionnaires pertaining to the effects of psilocybin were completed at baseline, on the day of the psilocybin session (before and after the intervention), and at 12 weeks follow-up, as previously described (Madsen et al., 2019, 2020). The following questionnaires were included: the Revised Mystical Experience Questionnaire-30 (MEQ30) (Barrett et al., 2015), the Ego-Dissolution Inventory (EDI) (Nour et al., 2016), and the Altered State of Consciousness (ASC) (Studerus et al., 2010). Persisting effects were evaluated three months after the psilocybin session using the Persisting Effects Questionnaire (PEQ) (Griffiths et al., 2006).

iii. Magnetic Resonance Imaging

MRI data were acquired using a 32-channel head coil on a Siemens Magnetom Prisma 3T scanner (Siemens AG, Erlangen, Germany). Structural T1- and T2-weighted images were acquired. T1 protocol: Isotropic 0.8x0.8x0.8 mm^3 resolution, repetition time = 1810 ms, echo

time = 2.41 ms, inversion time = 920 ms, and flip angle = 9°. T2 protocol: Isotropic 0.9x0.9x0.9 mm^3 resolution, repetition time = 3200 ms, echo time = 408 ms). MRI preprocessing and grey matter segmentation were performed as previously described (Johansen et al., 2023a).

iv. PET data acquisition and preprocessing

A full description of the [^{11}C]UCB-J PET acquisition (including radiosynthesis) and preprocessing has been published previously (Johansen et al., 2023a). Briefly, participants were scanned with a high-resolution research tomography (HRRT) PET scanner (CTI/Siemens, Knoxville, TN, USA) for 120 min, starting at the time of the intravenous [^{11}C]UCB-J bolus injection. PET data were acquired in 3D list-mode and reconstructed into 40 frames (8 x 15 s, 8 x 30 s, 4 x 60 s, 5 x 120 s, 10 x 300 s, 5 x 300 s) using 3D OP-OSEM algorithm with all standard corrections (Sureau et al., 2008). Images consisted of 207 planes of 256 x 256 voxels of 1.22x1.22x1.22 mm^3.

Arterial blood samples were collected and analyzed; for the first 15 min radioactivity was continuously measured using an Allogg ABSS autosampler (Allogg Technology, Mariefred, Sweden). Manual blood samples were drawn at 2.5, 5, 10, 25, 40, 60, 90 and 120 min to measure whole blood and plasma radioactivity using a gamma counter (Cobra II auto-gamma, Packard). Intact radioligand and radiolabeled metabolites were measured in plasma samples using radio-HPLC (UltiMate 3000, Thermo Fisher Scientific).

Scan related variables (injected dose, injected mass, and [^{11}C]UCB-J free fraction) are listed in Supplementary table S1.

v. PET image processing

Following motion correction with the AIR software using the reconcile function (Automated Image Registration, v. 5.2.5, LONI, UCLA, http://air.bmap.ucla.edu/AIR5/), we extracted time-activity curves from automatically defined regions of interest (ROIs) using a processing pipeline in the PVElab software (https://nru.dk/index.php/allcategories/category/30-software), similar to previously described (Svarer et al., 2005). Briefly, unfiltered PET images

6

were co-registered to participants' individual T1-weighted MR images using SPM12. Radioactivity counts were extracted from each ROI based on T1-weighted MRI segmentation of grey matter.

vi. Kinetic modeling of PET and blood data

Kinetic modeling of [^{11}C]UCB-J PET data was performed in R (v. 4.2.2, R Foundation, Vienna, Austria) using the *kinfirtr* package v. 0.6 (Tjerkaski et al., 2020). Regional time-activity curves and the corresponding metabolite-corrected arterial input function were fitted to the one-tissue compartment model (1TCM) to estimate the total volume of distribution (V_T). In addition, time-activity curves from the hippocampus and frontal cortex were fitted to the simplified reference tissue model 2 (SRTM2) using the white matter region centrum semiovale as the reference region, and the median k2 from 1TC modeling of centrum semiovale as a global k2' as determined within the sample.

vii. Statistical analyses

Changes in [^{11}C]UCB-J V_T and BP_{ND} estimates between baseline and 1-week follow-up for the hippocampus and the frontal cortex were compared using one-tailed paired t-tests, in accordance with the pre-registration protocol (aspredicted.org ID: 93092).

As exploratory analyses, we used correlation analyses to investigate whether change in [^{11}C]UCB-J V_T was associated with subjective ratings of the psychedelic experience rated immediately after the psilocybin session (MEQ30, EDI, ASC) and subjective persisting effects (PEQ) at 3-months follow-up. Because of high intercorrelation between the items in the PEQ, a total sum-score was calculated for the positive and the negative items, respectively.

Results

i. Acute effects of psilocybin

Participant demographics along with summary statistics of the subjective effects questionnaires and $[^{11}C]$UCB-J PET scan related parameters are listed in Table 1. There we no differences between baseline and follow-up scan acquisitions with regards to injected dose ($p = 0.23$), injected mass ($p = 0.46$), or free fraction of $[^{11}C]$UCB-J ($p = 0.8$).

The intervention with psilocybin was generally well-tolerated. One participant experienced anxiety as drug effects set in but responded well to the support from the psychologists. Participants undergoing interventions in the MRI scanner as well as in traditional environment experienced altered states of consciousness (Table 1). Six out of ten participants in the intervention room setting had a 'complete mystical experience' (defined as a score of ≥ 3 out of 5 on all four MEQ30 sub facets), while this was only the case for one out of five in the MRI setting. Participants in the intervention room setting scored significantly higher on the MEQ30 ($p = 0.04$), and positive PEQ items ($p = 0.001$), while there were no differences for the EDI ($p = 0.27$) and ASC (0.93).

Table 1	
Age (years)	32.5 [26.6, 60.3]
Female/male	5/10
Mystical Type Experience (MEQ; 0-5)	2.97 [1.7, 5.0]
Ego-Dissolution Inventory (EDI; 0-100)	71.5 [2.4, 100]
Altered State of Consciousness (ASC; 0-100)	34.4 [10.0, 66.8]
Positive Persisting Effects (PEQ; 0-100)	28.6 [1.8, 77.8]
Negative Persisting Effects (PEQ; 0-100)	2.73 [0, 17.6]
Injected radioactivity dose (MBq)	
Baseline	413 [266, 481]
1-week follow-up	388 [89, 466]
Injected mass (ng/kg)	
Baseline	5.7 [1.5, 10.8]
1-week follow-up	3.1 [2.2, 10.6]
f_p	
Baseline	0.33 [0.22, 0.45]
1-week follow-up	0.33 [0.21, 0.44]

Values are presented as median [range].

ii. *Effects of psilocybin on cerebral SV2A levels*

For the group of 12 participants with complete AIF, we saw no statistically significant increase in [^{11}C]UCB-J V_T following the psilocybin intervention. [^{11}C]UCB-J V_T estimates for the baseline and follow-up scans along with changes are shown in Figure 1 and summarized in Table 2.

For completeness, we also evaluated the non-displaceable binding potential (BP_{ND}) for the total sample of 15 subjects based on reference tissue modelling using the white matter region centrum semiovale as reference region. For the hippocampus, the mean BP_{ND} (SD) at baseline was 2.74 (0.3) versus 2.75 (0.27) one week after psilocybin intervention ($p = 0.44$). For the frontal cortex, the mean BP_{ND} (SD) at baseline was 3.67 (0.38) versus 3.66 (0.43) one week after psilocybin intervention ($p = 0.53$).
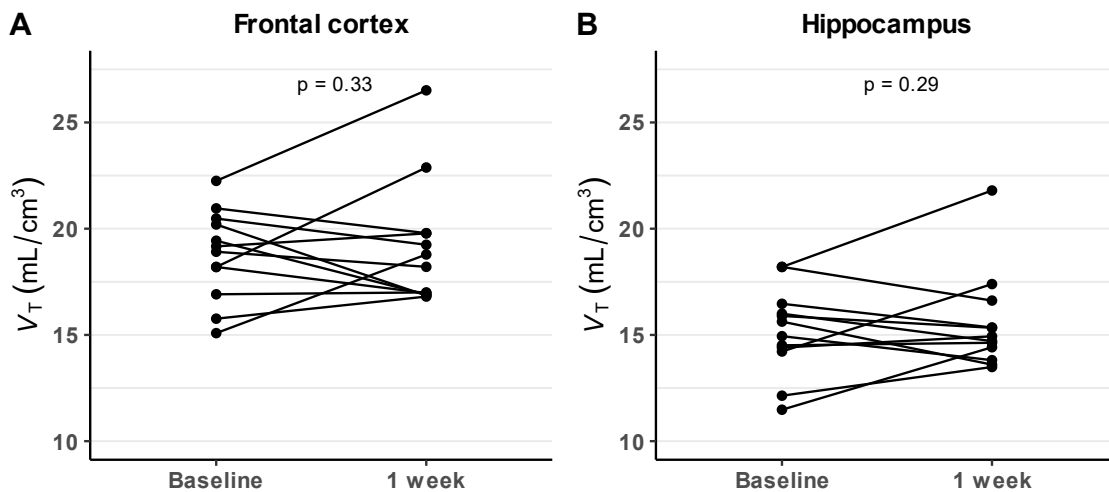

Figure 1. [^{11}C]UCB-J binding (V_T) estimates for the frontal cortex (**A**) and the hippocampus (**B**) at baseline and 1-week after psilocybin intervention compared with one-tailed *t*-tests.

Table 2.

	Baseline V_T (mL/cm³)	Follow-up V_T (mL/cm³)	Mean difference (mL/cm³)	Relative difference (%)	p-value
Hippocampus	15.2 (2.1)	15.5 (2.3)	0.3 (2.0)	+3.0 (13.5)	0.29
Frontal cortex	18.8 (2.1)	19.1 (2.9)	0.3 (2.6)	+2.6 (14.1)	0.32

Summary of [^{11}C]UCB-J V_T estimates for the baseline and 1-week follow-up scans. Changes in V_T were compared using one-tailed, paired *t*-tests.

iii. Exploratory analyses

We further investigated the potential association between change in frontal cortex and hippocampus [11C]UCB-J V_T, respectively, and subjective ratings after the psilocybin session. For the questionnaires filled out immediately after the psilocybin session, we saw no association for the MEQ30 total score (r < 0.38, *p* > 0.21), the EDI score (r < 0.35, p > 0.24), or the ASC mean score (rho < 0.09, p > 0.77).

We also investigated persisting effects at 3 months post-psilocybin. Here, the PEQ positive and negative effects' sub scales were summed, respectively. For the negative sum score, there was a negative association with change in [11C]UCB-J V_T for the hippocampus (rho = -0.62, p = 0.023) and the neocortex (rho = -0.69, p = 0.009). There was no association between change in [11C]UCB-J V_T and the positive sum score (r < 0.27, p > 0.37).

All correlation coefficients for the total scores and sub scales are listed in Supplementary Tables.

Discussion

This study represents the first investigation into the persistent effects of psilocybin on synaptic density in the human brain. We did not find evidence for consistent changes in cerebral SV2A density one week after administering a single dose of psilocybin to healthy individuals, as measured by [11C]UCB-J PET. Our exploratory analyses hinted at positive associations between SV2A changes and subjective effects related to positive psychological experiences during the session, while negative SV2A changes were associated with more negative persisting effects at three months follow-up.

Affective and anxiety-related neuropsychiatric disorders are believed to involve a diminished capacity for neuroplasticity, which psilocybin has been hypothesized to reinstate. By conducting this study in healthy individuals without neuropsychiatric symptoms or associated pathological changes, we were able to assess the synaptic effects of psilocybin from a purely neurobiological perspective. As such, the results cannot be directly generalized to patient populations. A previous [11C]UCB-J PET imaging study indicates that patients with

severe depression have lower SV2A binding compared to healthy individuals (Holmes et al., 2019), and thus it is possible that psilocybin may induce neuroplasticity and restore lost synapses in individuals with MDD. Ongoing research on psilocybin's ability to stimulate synaptic plasticity in patient with depression will provide further insights into this question.

In our exploratory analyses relating subjective effects of psilocybin to change in [^{11}C]UCB-J binding, we saw that participants who scored higher on the mystical experience questionnaire sub scores 'positive mood' and 'mystical' had a tendency towards increasing their [^{11}C]UCB-J V_T more, although the estimates of the association came with considerable uncertainty (p-values > 0.09). In contrast, we observed a negative association between change in [^{11}C]UCB-J V_T and negative persisting effects at 3 months follow-up.

One key consideration is the timing of the follow-up [^{11}C]UCB-J PET scan. Many preclinical studies have evaluated effects after 24 hours. Notably, our research group recently demonstrated higher SV2A levels in the hippocampus one day after intravenous administration of a psychedelic-equivalent dose of psilocybin in pigs (Raval et al., 2021). Thus, it is possible that psilocybin induces a transient increase in SV2A that is normalized at 1-week follow-up.

Another rapid-acting antidepressant, ketamine, has also been investigated for its ability to induce changes in healthy individuals and patients with mixed psychiatric conditions. A similar [^{11}C]UCB-J PET study examining the effects of ketamine found no change in SV2A 24 hours after a ketamine infusion (Holmes et al., 2022). Considering the distinct pharmacological profiles of ketamine and psychedelics, we would, however, not necessarily expect their downstream effects and time courses to be identical.

Psilocybin acts on a range of different receptors, but its psychedelic effects primarily depend on the activation of postsynaptic 5-HT2AR (Madsen et al., 2019) which is heavily expressed in the neocortex (Beliveau et al., 2017). Consequently, effects on SV2A density would likely manifest downstream in the projection areas of 5-HT2AR-activated neurons. Yet, postsynaptic feedback through, e.g., cell-adhesion molecules, could potentially strengthen presynaptic density upstream from the 5-HT2ARs as well.

Our study was powered to detect 5% increase in [^{11}C]UCB-J V_T in the hippocampus. However, it is important to note that V_T represents total tissue binding of the radioligand, including the non-displaceable compartment. Furthermore, synaptic alterations may be specific to certain neuron populations in specific layers (e.g., interneurons vs. projection neurons) or show differential effects on excitatory and inhibitory neurons. Additionally, changes in synaptic density might vary between different networks, with some showing increased density while others may decrease (Madsen et al., 2021).

Few studies have investigated the effects of pharmacological interventions on in vivo SV2A in the human brain. In a recent study, we assessed the effects of a different serotonergic modulator in healthy individuals, namely the selective serotonin reuptake inhibitor escitalopram, and found an association between the duration of the intervention and [^{11}C]UCB-J binding, pointing to a gradually emerging effect. Similarly, another study found a positive association between SV2A density and recent cocaine use (Angarita et al., 2022). As such, the dynamics of synaptic density measured with SV2A likely could be affected differently for different interventions.

The present study has some important limitations that should be acknowledged. First, five of our subjects underwent the psilocybin intervention in an MRI scanner setting. This subgroup had less intense psychedelic experiences than the participants undergoing the intervention in a designated intervention room with music being played. As positive experiences during the intervention have been shown to predict persistent positive psychological effects in patients, it is possible that there is a threshold for intensity that must be exceeded for persisting neurobiological effects to occur.

Second, our study was carried out in a small sample with an open-label design that did not include a placebo condition. This potentially limits us in detecting increases in SV2A binding, as previous studies have reported a negative bias for [^{11}C]UCB-J estimates. One study reported decreases in regional V_T in the range of -1% to -8% and for BP_{ND} in the range of -5% to -14% (Tuncel et al., 2020) between baseline and rescan four weeks apart. Another test-retest

study with test-retest performed on the same day also showed a negative bias in BP_{ND} (Li et al., 2021).

Conclusion

In conclusion, our study represents a crucial step in understanding the persisting effects of psilocybin on synaptic density in the human brain. While we did not observe changes in synaptic density one week after psilocybin administration in healthy individuals, the potential for neuroplasticity may be more pronounced in patient populations with neuropsychiatric disorders. Investigating the timing and duration of synaptic changes induced by psilocybin, as well as differential effects on various neuron populations and networks, will contribute to a more comprehensive understanding of the therapeutic mechanisms.

Disclosure

GMK has within the last three years received honoraria as speaker for Angelini, H Lundbeck and Sage Therapeutics and as a consultant for Sanos, Onsero, Pangea, Gilgamesh, Pure Technologies and Abbvie. All other authors declare that there are no conflicts of interest.

References

Angarita, G. A., Worhunsky, P. D., Naganawa, M., Toyonaga, T., Nabulsi, N. B., Li, C. R., et al. (2022). Lower prefrontal cortical synaptic vesicle binding in cocaine use disorder: An exploratory 11C-UCB-J positron emission tomography study in humans. *Addict Biol* 27, e13123. doi: 10.1111/adb.13123.

Barrett, F. S., Johnson, M. W., and Griffiths, R. R. (2015). Validation of the revised Mystical Experience Questionnaire in experimental sessions with psilocybin. *J. Psychopharmacol.* 29, 1182–1190. doi: 10.1177/0269881115609019.

Beliveau, V., Ganz, M., Feng, L., Ozenne, B., Højgaard, L., Fisher, P. M., et al. (2017). A High-Resolution In Vivo Atlas of the Human Brain's Serotonin System. *J Neurosci* 37, 120–128. doi: 10.1523/jneurosci.2830-16.2016.

Calder, A. E., and Hasler, G. (2023). Towards an understanding of psychedelic-induced neuroplasticity. *Neuropsychopharmacol* 48, 104–112. doi: 10.1038/s41386-022-01389-z.

Carhart-Harris, R., Giribaldi, B., Watts, R., Baker-Jones, M., Murphy-Beiner, A., Murphy, R., et al. (2021). Trial of Psilocybin versus Escitalopram for Depression. *New Engl J Med* 384, 1402–1411. doi: 10.1056/nejmoa2032994.

Carhart-Harris, R. L., Bolstridge, M., Day, C. M. J., Rucker, J., Watts, R., Erritzoe, D. E., et al. (2018). Psilocybin with psychological support for treatment-resistant depression: six-month follow-up. *Psychopharmacology* 235, 399–408. doi: 10.1007/s00213-017-4771-x.

Carhart-Harris, R. L., Bolstridge, M., Rucker, J., Day, C. M. J. J., Erritzoe, D., Kaelen, M., et al. (2016). Psilocybin with psychological support for treatment-resistant depression: An open-label feasibility study. *Lancet Psychiatry* 3, 619--627. doi: 10.1016/s2215-0366(16)30065-7.

Davis, A. K., Barrett, F. S., May, D. G., Cosimano, M. P., Sepeda, N. D., Johnson, M. W., et al. (2021). Effects of Psilocybin-Assisted Therapy on Major Depressive Disorder. *Jama Psychiat* 78, 481–489. doi: 10.1001/jamapsychiatry.2020.3285.

Erritzoe, D., Roseman, L., Nour, M. M., MacLean, K., Kaelen, M., Nutt, D. J., et al. (2018). Effects of psilocybin therapy on personality structure. *Acta Psychiat Scand* 138, 368–378. doi: 10.1111/acps.12904.

Gelenberg, A. J., Freeman, M. P., Markowitz, J. C., Rosenbaum, J. F., Thase, M. E., Trivedi, M. H., et al. (2010). Treatment of Patients With Major Depressive Disorder. Available at: https://psychiatryonline.org/pb/assets/raw/sitewide/practice_guidelines/guidelines/mdd.pdf [Accessed September 6, 2022].

Griffiths, R. R., Richards, W. A., McCann, U., and Jesse, R. (2006). Psilocybin can occasion mystical-type experiences having substantial and sustained personal meaning and spiritual significance. *Psychopharmacology* 187, 268–283. doi: 10.1007/s00213-006-0457-5.

Holmes, S. E., Finnema, S. J., Naganawa, M., DellaGioia, N., Holden, D., Fowles, K., et al. (2022). Imaging the effect of ketamine on synaptic density (SV2A) in the living brain. *Mol Psychiatr* 27, 2273–2281. doi: 10.1038/s41380-022-01465-2.

Holmes, S. E., Scheinost, D., Finnema, S. J., Naganawa, M., Davis, M. T., DellaGioia, N., et al. (2019). Lower synaptic density is associated with depression severity and network alterations. *Nat Commun* 10, 1529. doi: 10.1038/s41467-019-09562-7.

Johansen, A., Armand, S., Plaven-Sigray, P., Nasser, A., Ozenne, B., Sahakian, B. J., et al. (2023a). Effects of escitalopram on synaptic density in the human brain: a randomized controlled trial. *Molecular Psychiatry* In press.

Johansen, A., Beliveau, V., Colliander, E., Raval, N. R., Dam, V. H., Gillings, N., et al. (2023b). An in vivo high-resolution human brain atlas of synaptic density.

Kasper, S., Spadone, C., Verpillat, P., and Angst, J. (2006). Onset of action of escitalopram compared with other antidepressants: results of a pooled analysis. *Int Clin Psychopharm* 21, 105–110. doi: 10.1097/01.yic.0000194375.42589.c3.

Kometer, M., Schmidt, A., Bachmann, R., Studerus, E., Seifritz, E., and Vollenweider, F. X. (2012). Psilocybin Biases Facial Recognition, Goal-Directed Behavior, and Mood State Toward Positive Relative to Negative Emotions Through Different Serotonergic Subreceptors. *Biol Psychiat* 72, 898–906. doi: 10.1016/j.biopsych.2012.04.005.

Li, S., Naganawa, M., Pracitto, R., Najafzadeh, S., Holden, D., Henry, S., et al. (2021). Assessment of test-retest reproducibility of [18F]SynVesT-1, a novel radiotracer for PET imaging of synaptic vesicle glycoprotein 2A. *Eur J Nucl Med Mol I* 48, 1327–1338. doi: 10.1007/s00259-020-05149-3.

Ly, C., Greb, A. C., Cameron, L. P., Wong, J. M., Barragan, E. V., Wilson, P. C., et al. (2018). Psychedelics Promote Structural and Functional Neural Plasticity. *Cell Reports* 23, 3170–3182. doi: 10.1016/j.celrep.2018.05.022.

Ly, C., Greb, A. C., Vargas, M. V., Duim, W. C., Grodzki, A. C. G., Lein, P. J., et al. (2021). Transient Stimulation with Psychoplastogens Is Sufficient to Initiate Neuronal Growth. *ACS Pharmacol. Transl. Sci.* 4, 452–460. doi: 10.1021/acsptsci.0c00065.

MacLean, K. A., Johnson, M. W., and Griffiths, R. R. (2011). Mystical experiences occasioned by the hallucinogen psilocybin lead to increases in the personality domain of openness. *J Psychopharmacol* 25, 1453–1461. doi: 10.1177/0269881111420188.

Madsen, M. K., Fisher, P. M., Burmester, D., Dyssegaard, A., Stenbæk, D. S., Kristiansen, S., et al. (2019). Psychedelic effects of psilocybin correlate with serotonin 2A receptor occupancy and plasma psilocin levels. *Neuropsychopharmacol* 44, 1328–1334. doi: 10.1038/s41386-019-0324-9.

Madsen, M. K., Fisher, P. M., Stenbæk, D. S., Kristiansen, S., Burmester, D., Lehel, S., et al. (2020). A single psilocybin dose is associated with long-term increased mindfulness, preceded by a proportional change in neocortical 5-HT2A receptor binding. *Eur Neuropsychopharm* 33, 71–80. doi: 10.1016/j.euroneuro.2020.02.001.

Madsen, M. K., Stenbæk, D. S., Arvidsson, A., Armand, S., Marstrand-Joergensen, M. R., Johansen, S. S., et al. (2021). Psilocybin-induced changes in brain network integrity and segregation correlate with plasma psilocin level and psychedelic experience. *Eur Neuropsychopharm* 50, 121–132. doi: 10.1016/j.euroneuro.2021.06.001.

McCulloch, D. E.-W., Grzywacz, M. Z., Madsen, M. K., Jensen, P. S., Ozenne, B., Armand, S., et al. (2022). Psilocybin-Induced Mystical-Type Experiences are Related to Persisting Positive Effects: A Quantitative and Qualitative Report. *Front Pharmacol* 13, 841648. doi: 10.3389/fphar.2022.841648.

Messell, C., Summer, L., Bonde, L. O., Beck, B. D., and Stenbæk, D. S. (2022). Music programming for psilocybin-assisted therapy: Guided Imagery and Music-informed perspectives. *Front Psychol* 13, 873455. doi: 10.3389/fpsyg.2022.873455.

Moliner, R., Girych, M., Brunello, C. A., Kovaleva, V., Biojone, C., Enkavi, G., et al. (2023). Psychedelics promote plasticity by directly binding to BDNF receptor TrkB. *Nat. Neurosci.*, 1–10. doi: 10.1038/s41593-023-01316-5.

Nautiyal, K. M., and Yaden, D. B. (2023). Does the trip matter? Investigating the role of the subjective effects of psychedelics in persisting therapeutic effects. *Neuropsychopharmacol* 48, 215–216. doi: 10.1038/s41386-022-01424-z.

Nichols, D. E. (2016). Psychedelics. *Pharmacol Rev* 68, 264–355. doi: 10.1124/pr.115.011478.

Nour, M. M., Evans, L., Nutt, D., and Carhart-Harris, R. L. (2016). Ego-Dissolution and Psychedelics: Validation of the Ego-Dissolution Inventory (EDI). *Front. Hum. Neurosci.* 10, 269. doi: 10.3389/fnhum.2016.00269.

Olson, D. E. (2022). Biochemical Mechanisms Underlying Psychedelic-Induced Neuroplasticity. *Biochemistry-us* 61, 127–136. doi: 10.1021/acs.biochem.1c00812.

Quednow, B. B., Kometer, M., Geyer, M. A., and Vollenweider, F. X. (2012). Psilocybin-Induced Deficits in Automatic and Controlled Inhibition are Attenuated by Ketanserin in Healthy Human Volunteers. *Neuropsychopharmacol* 37, 630–640. doi: 10.1038/npp.2011.228.

Raval, N. R., Johansen, A., Donovan, L. L., Ros, N. F., Ozenne, B., Hansen, H. D., et al. (2021). A Single Dose of Psilocybin Increases Synaptic Density and Decreases 5-HT2A Receptor Density in the Pig Brain. *Int J Mol Sci* 22, 835. doi: 10.3390/ijms22020835.

Roseman, L., Nutt, D. J., and Carhart-Harris, R. L. (2018). Quality of Acute Psychedelic Experience Predicts Therapeutic Efficacy of Psilocybin for Treatment-Resistant Depression. *Front Pharmacol* 8, 974. doi: 10.3389/fphar.2017.00974.

Shao, L.-X., Liao, C., Gregg, I., Davoudian, P. A., Savalia, N. K., Delagarza, K., et al. (2021). Psilocybin induces rapid and persistent growth of dendritic spines in frontal cortex in vivo. *Neuron* 109, 2535-2544.e4. doi: 10.1016/j.neuron.2021.06.008.

Smigielski, L., Scheidegger, M., Kometer, M., and Vollenweider, F. X. (2019). Psilocybin-assisted mindfulness training modulates self-consciousness and brain default mode network connectivity with lasting effects. *Neuroimage* 196, 207–215. doi: 10.1016/j.neuroimage.2019.04.009.

Søndergaard, A., Madsen, M. K., Ozenne, B., Armand, S., Knudsen, G. M., Fisher, P. M., et al. (2022). Lasting increases in trait mindfulness after psilocybin correlate positively with the mystical-type experience in healthy individuals. *Front Psychol* 13, 948729. doi: 10.3389/fpsyg.2022.948729.

Stenbæk, D. S., Madsen, M. K., Ozenne, B., Kristiansen, S., Burmester, D., Erritzoe, D., et al. (2021). Brain serotonin 2A receptor binding predicts subjective temporal and mystical effects of psilocybin in healthy humans. *J Psychopharmacol* 35, 459–468. doi: 10.1177/0269881120959609.

Studerus, E., Gamma, A., and Vollenweider, F. X. (2010). Psychometric Evaluation of the Altered States of Consciousness Rating Scale (OAV). *PLoS ONE* 5, e12412. doi: 10.1371/journal.pone.0012412.

Sureau, F. C., Reader, A. J., Comtat, C., Leroy, C., Ribeiro, M.-J., Buvat, I., et al. (2008). Impact of Image-Space Resolution Modeling for Studies with the High-Resolution Research Tomograph. *J Nucl Med* 49, 1000–1008. doi: 10.2967/jnumed.107.045351.

Svarer, C., Madsen, K., Hasselbalch, S. G., Pinborg, L. H., Haugbøl, S., Frøkjær, V. G., et al. (2005). MR-based automatic delineation of volumes of interest in human brain PET images using probability maps. *Neuroimage* 24, 969–979. doi: 10.1016/j.neuroimage.2004.10.017.

Tjerkaski, J., Cervenka, S., Farde, L., and Matheson, G. J. (2020). Kinfitr — an open-source tool for reproducible PET modelling: validation and evaluation of test-retest reliability. *EJNMMI Res* 10, 77. doi: 10.1186/s13550-020-00664-8.

Tuncel, H., Boellaard, R., Coomans, E. M., Vries, E. F. de, Glaudemans, A. W., Feltes, P. K., et al. (2020). Kinetics and 28-day test–retest repeatability and reproducibility of [11C]UCB-J PET brain imaging. *J Cereb Blood Flow Metabolism* 41, 1338–1350. doi: 10.1177/0271678x20964248.

Vargas, M. V., Dunlap, L. E., Dong, C., Carter, S. J., Tombari, R. J., Jami, S. A., et al. (2023). Psychedelics promote neuroplasticity through the activation of intracellular 5-HT2A receptors. *Science* 379, 700–706. doi: 10.1126/science.adf0435.

Vollenweider, F. X., and Preller, K. H. (2020). Psychedelic drugs: neurobiology and potential for treatment of psychiatric disorders. *Nat Rev Neurosci* 21, 611–624. doi: 10.1038/s41583-020-0367-2.

Vollenweider, F. X., Vollenweider-Scherpenhuyzen, M. F. I., Bäbler, A., Vogel, H., and Hell, D. (1998). Psilocybin induces schizophrenia-like psychosis in humans via a serotonin-2 agonist action. *Neuroreport* 9, 3897–3902. doi: 10.1097/00001756-199812010-00024.

Vos, C. M. H. de, Mason, N. L., and Kuypers, K. P. C. (2021). Psychedelics and Neuroplasticity: A Systematic Review Unraveling the Biological Underpinnings of Psychedelics. *Frontiers Psychiatry* 12, 724606. doi: 10.3389/fpsyt.2021.724606.

Yaden, D. B., and Griffiths, R. R. (2021). The Subjective Effects of Psychedelics Are Necessary for Their Enduring Therapeutic Effects. *ACS Pharmacol. Transl. Sci.* 4, 568–572. doi: 10.1021/acsptsci.0c00194.

Supplementary file

Effects of psilocybin on synaptic plasticity in the human brain

Questionnaire item	Frontal cortex				Hippocampus			
	Pearson r	p_value	Spearman rho	p_value	Pearson r	p_value	Spearman r	p_value
MEQ_total	0.375	0.206	0.396	0.182	0.284	0.346	0.192	0.529
Mystical	0.412	0.161	0.349	0.242	0.327	0.275	0.154	0.615
Positive.mood	0.487	0.091	0.434	0.138	0.373	0.209	0.257	0.396
Transcendence.of.time.and.space	0.072	0.816	0.033	0.914	-0.012	0.97	-0.218	0.474
Ineffability	0.147	0.632	0.112	0.715	0.137	0.655	-0.073	0.813
EDI_mean	0.351	0.24	0.325	0.279	0.327	0.276	0.08	0.796
ASC_total_mean	0.049	0.874	0.093	0.765	0.03	0.922	-0.099	0.751
Experience.of.unity	0.408	0.167	0.534	0.06	0.38	0.2	0.344	0.25
Spiritual.experience	0.225	0.461	0.291	0.334	0.157	0.608	0.143	0.643
Blissfull.state	0.573	0.041	0.549	0.055	0.462	0.112	0.335	0.263
Insightfulness	0.185	0.546	0.181	0.554	0.141	0.647	0.049	0.878
Disembodiment	-0.117	0.704	-0.165	0.59	-0.093	0.763	-0.253	0.404
Impaired.control.and.cognition	-0.287	0.342	-0.099	0.751	-0.277	0.359	-0.203	0.505
Anxiety	-0.034	0.912	-0.033	0.915	-0.078	0.8	-0.176	0.564
Complex.imagery	-0.213	0.485	-0.148	0.63	-0.176	0.566	-0.242	0.426
Elementary.imagery	0.131	0.67	0.188	0.539	0.282	0.351	0.271	0.371
Audio-visual.synesthesia	-0.067	0.827	-0.16	0.603	-0.069	0.823	-0.187	0.541
Changed.meanings.of.percepts	-0.277	0.359	-0.259	0.394	-0.24	0.429	-0.36	0.226
PEQ SumPos	0.286	0.343	0.148	0.63	0.244	0.423	0.148	0.63
PEQ SumNeg	-0.519	0.069	-0.719	0.006	-0.496	0.085	-0.638	0.019